THE UNIVERSITY OF CHICAGO

FIRST PRINCIPLES CALCULATIONS OF NANOMATERIALS FOR RENEWABLE
ENERGY

A DISSERTATION SUBMITTED TO
THE FACULTY OF THE PRITZKER SCHOOL OF MOLECULAR ENGINEERING
IN CANDIDACY FOR THE DEGREE OF
DOCTOR OF PHILOSOPHY

BY
ARIN RAE GREENWOOD

CHICAGO, ILLINOIS
AUGUST 2020

ProQuest Number: 28025130

ProQuest.

ProQuest 28025130

ProQuest LLC
789 East Eisenhower Parkway
P.O. Box 1346
Ann Arbor, MI 48106 - 1346

For my mother, who has waited patiently while I pursue my dreams halfway across the country.

TABLE OF CONTENTS

LIST OF FIGURES

LIST OF TABLES

ACKNOWLEDGMENTS

I owe this journey to the incredible friends and mentors I've met over the past six years, as well as my family who has supported me every step of the way. It would be impossible to thank each and every one of you, but I'll try my best:

Thanks to my advisor, Professor Giulia Galli, who has taught me to think critically, to push myself beyond what I felt I was capable of, and to be a confident and strong female scientist.

Thanks to all the professors and teachers who have supported and guided me, in particular Professor Juan de Pablo, whose faith in me has been unwavering, Professor François Gygi at UC Davis, who always had answers when I needed them, Professor Jay Schieber at IIT, who taught the best (and hardest) math class imaginable, and Professor Jim Pfaendtner at the University of Washington, who encouraged me to be a Molecular Engineer.

Thanks to Dr. Márton Vörös and Dr. Federico Giberti, the best mentors and friends anyone could have asked for.

Thanks to my colleague, collaborator, and close friend Sergio Mazzotti - I could not have done this without you.

Thanks to Viktor Rozsa, my Galli Group partner in crime.

Thanks to all of my friends, in Chicago and around the world, who supported me in countless ways, including: Dr. Ashley Guo, Dr. Moshe Dolejsi, Dr. Emre Sevgen, Dr. Zack Jarin, Dr. Josh Moller, Dr. Alex Gaiduk, Dr. Nicholas Brawand, Dr. Mariami Rusishvili, Ryan McAvoy, Elyse Watkins, Elizabeth Ashley, Viviana Palacio Betancur, Jeff Gustafson, Tami McTaggart, Tiffany Du Bennett, Wilson Chan, Josh Fuller, Austin Brown, Erin Harris, Zoe Drew-King, Maile Hollinger, and Nicholas Msall.

Thanks to my late grandfather, James G. Lilley, who always told me that physics was easier than dancing.

Finally, thanks to my best friend, role model, and mother, Diana Greenwood. I am who I am because of you.

ABSTRACT

Nanostructured materials, including nanoparticles, nanoplatelets and Metal Organic Frameworks are promising platforms for numerous applications in the field of renewable energy. Inorganic, semiconducting nanoparticles and nanoplatelets, for example, are ideal materials for the design of novel photovoltaic devices due to optoelectronic properties that are tunable through modification of their shape, size and composition. Much attention has been drawn to improving efficiency and device performance through altering the character of the nanomaterials, but the discovery of design rules for optimal device performance is still an open question. Due to challenges in controlling experimental techniques on an atomic scale, as well as numerous combinations of size, shape, composition and surface termination, experimental material design in this field is best complemented by accurate atomistic calculations. The latter can help interpret experiments, predict new materials and offer physical understanding.

In this dissertation, we take a tour of three classes of nanomaterials that span different dimensionalities and offer different opportunities for renewable energy material design. First, we seek to understand the collective properties of a thin film of cubic lead sulfide nanoparticles that display quantum confinement in all three directions and are used in solar cell devices. We look at the combined effects of temperature and interactions between nanoparticles, and show that at finite temperature, interacting nanoparticles are dynamical dipolar systems with average values of dipole moments and polarizabilities substantially increased with respect to those of the isolated building blocks. We also present a critical discussion of various results reported in the literature for the dipole moments of nanoparticles. This work has important implications for understanding the nature of charge transport through nanoparticle thin films within a solar cell, as it is the interactions and spacing between nanoparticles that govern the charge transfer behavior.

Next, we transition from the collective properties of a nanoparticle film to the optoelectronic properties of individual quasi-two dimensional cadmium selenide nanoplatelets. We use this quasi-2D material, quantum confined in only one direction, to develop a general,

predictive computational protocol for calculations of 2D materials. Through building up this framework, we provide an understanding of the optical gap of CdSe nanoplatelets, a main experimental observable essential for photovoltaic devices. Our investigation of the optical gap is completed through disentangling the interplay between three main effects: biaxial strain, quantum confinement, and dielectric contrast between the material and its environment. We present the first calculations for these materials based on many-body perturbation theory, of both the fundamental gap and exciton binding energies, validating models that enable further investigation of larger and more complex systems. We discuss a series of models of quasiparticle energies that allow for comparison with previous theoretical predictions and provide the ability to directly probe the three key effects. These models provide a simple method to estimate the gap of complex nanoplatelets, with potential implications for the search of optimal nanomaterials for photovoltaic devices.

Finally, we end with a short investigation of a recently synthesized 3D Metal Organic Framework that, while macroscopic in nature, exhibits a nanoporous structure ideal for gas storage, separation and catalysis. In conjunction with experiment, we show that these MOFs exist in an energetically favorable anti-ferromagnetic state, with the ferromagnetic and non-magnetic spin configurations inaccessible due to structural rigidity. Together, our first principles predictions of the optoelectronic properties of nanoparticles, nanoplatelets and Metal Organic Frameworks, along with experimental characterization and synthesis of similar materials, is expected to help guide the search for optimal nanomaterials for renewable energy devices.

CHAPTER 1

INTRODUCTION

The success of the field of nanoscience has been established through collaboration between experiment, theory and simulation. While experimental chemists and physicists are consistently improving synthesis and characterization techniques that allow for atomically precise materials that can be visualized on an atomic scale, computational research is an essential guiding force for understanding the underlying physics and making predictions that push the field forward faster than would otherwise be possible. Particularly when viewing nanoscience through the lens of engineering renewable energy devices to combat climate change and meet increasing energy demands, the entanglement of experiment and computation is indispensable. Thus, a computational framework that can be used to both interpret experiments and make predictions is essential.

Density Functional Theory (DFT) is a common, versatile first-principles computational method that allows for the prediction of the structural and optoelectronic properties of materials from a microscopic scale. DFT, as well as other methods based upon it, is the tool of choice for this dissertation to understand the electronic structure of three classes of nanomaterials spanning dimensionalities from "0D" nanoparticles to quasi-2D nanoplatelets to 3D crystalline bulk Metal-Organic Frameworks. In this dissertation, we seek to progress the current understanding for the design of ideal nanomaterial-based photovoltaic devices by demonstrating the importance of key features for both the collective properties of nanomaterial films and individual properties of the nanomaterial "building blocks," for example highlighting the importance of temperature effects, interactions between nano-objects, and the structure-function relationships in strongly anisotropic 2D nanomaterials.

We start in Chapter 2 by briefly introducing the topic of nanomaterials for renewable energy applications by surveying the current landscape of the field. In particular, we devote Section 2.2 and Section 2.3 to a discussion of the use of nanoparticles and nanoplatelets, respectively, as thin films in solar cells that have the potential to be smaller, cheaper and

more flexible than the prevalent silicon devices. Then, we transition to a short overview of a very different class of nanomaterials, namely Metal Organic Frameworks (MOFs), which are nanoporous, rigid 3D structures ideal for gas storage, gas separation and catalysis.

In Chapter 3, we present a summary of all of the first-principles computational methods and theory that have been used in this dissertation. In Section 3.2 we provide an overview and brief history of Density Functional Theory (DFT), the foundation of our electronic structure calculations. We include a discussion of different approximations that can be made and the trade-offs that are essential to consider, including approximations to the exchange-correlation potential, the use of a plane-wave basis set, and selection of pseudopotentials to represent the core electrons and nuclei. We end the section with an example of a study that we performed to investigate the accuracy of two different pseudopotentials. In Section 3.3, we show how the concepts of ground state DFT can be coupled to molecular dynamics to probe the finite temperature, dynamical properties of materials through the use of First Principles Molecular Dynamics (FPMD). Then, in Section 3.4, we describe two first principles methods for calculating dielectric properties of materials through applied electric fields. In Section 3.5, we move from DFT-based methods to introduce Many Body Perturbation Theory, which provides us with a way to calculate the electronic structure of materials with quantitative comparison to experimental measurements such as the Ionization Potential and Electron Affinity that probe the highest occupied and lowest unoccupied energy states, respectively. Finally, in Section 3.6, we introduce another state-of-the-art method, namely the Bethe-Salpeter Equation, which can be used to compare directly with experiments, absorption spectra and related optical properties.

In Chapter 4, we present our first application of first-principles methods to nanomaterials, in particular using DFT and FPMD to probe the changes in electronic structure as nanoparticles interact with one another in a thin film. After a brief introduction and discussion of the computational details, in Section 4.3 we begin by showing how the electronic structure of isolated NPs change as a function of temperature, looking in particular at the

fundamental band gaps, radiative lifetimes, and dipole moments of these nanocrystallites. We also present a critical discussion of various results reported in the literature for the values of dipole moments of nanoparticles. In Section 4.4 we take what we learned from the isolated NPs at finite temperature and show how interactions between these NPs can drastically change their properties. Of particular note, we show that at finite temperature, interacting NPs act as dynamical dipolar systems, with average values of dipole moments and polarizabilities substantially increased with respect to those of the isolated building blocks.

In Chapter 5, we turn our attention from the "zero"-dimensional nanoparticles, which are quite established from computational, synthetic, and device-integration standpoints, to quasi-two dimensional semiconducting nanoplatelets (NPLs) which are a class of nanomaterials that is newer and less understood but can be synthesized with remarkable precision. Because of this atomistic-level control of the NPL thickness and thus enhanced tunability of optoelectronic properties, these materials have the potential to out-perform nanoparticles for use in solar cells as well as other applications such as lasing and LEDs. However, as these materials are newer, many computational questions remain regarding how to accurately calculate their properties, especially because physical models and assumptions have not previously been probed and validated for this quasi-two dimensional regime. Thus, after a brief introduction, in Section 5.3, we begin by discussing the structural properties of the NPLs used in this study, looking in particular at the effect of biaxial strain. In Section 5.4, we present calculations of the fundamental band gap and band structure calculated at different levels of theory, comparing to available models in the literature and suggest a new model that can estimate quasiparticle band gaps with near G_0W_0 accuracy using only calculations of the bulk material. We include a brief discussion of the challenges related to calculating or defining a dielectric constant for these materials, and we present a method for calculating an effective dielectric constant of a quasi-2D material based upon the electrostatic potential; we validate our method through hybrid functional calculations of the band gap, using a functional whose definition contains the dielectric constant. In the final section, we move

3

to a more direct comparison with experiments by probing the exciton binding energy and calculating the absorption spectra of the NPLs using the Bethe-Salpeter Equation (BSE). We compare our results to existing models, shedding light on the validity of a number of assumptions from the models that have not been assessed for quasi-two dimensional materials. Our work offers the first calculations of both the G_0W_0 fundamental gap and BSE exciton binding energies, enabling further investigation of and improvement upon models that can reduce the computational cost relative to first principles calculations.

Finally, in Chapter 6 we complete our computational investigation of nanomaterials for renewable energy by presenting a short study on the stability of a class of 3D Metal Organic Frameworks (MOFs). In conjunction with experiment, we show that these MOFs exist in an energetically favorable anti-ferromagnetic state, with the ferromagnetic and non-magnetic spin configurations largely inaccessible due to structural rigidity.

We conclude the dissertation in Chapter 7 with a summary and brief discussion of the future directions to which our research could lead.

CHAPTER 2

NANOMATERIALS FOR ENERGY APPLICATIONS

2.1 Introduction

The growing field of renewable energy is essential for reducing greenhouse gas emissions and reducing the use of fossil fuels, which are currently the largest source of carbon dioxide emissions in the United States [5]. Concerns over climate change and global warming, as well as decreasing costs of renewable energy devices, have led to an increase in renewable energy consumption in the past ten years, but currently non-renewable resources still make up nearly 90% of the energy consumption in the United States [5]. In order to expand our use of renewable energy and eliminate the reliance on fossil fuels, it is vital to continue research into cheaper and more versatile materials that can be used in renewable energy devices with suitable efficiency. Particularly in the area of solar energy, nanomaterials have shown remarkable promise as alternative materials to produce cost effective photovoltaic cells with competitive energy conversion efficiency that can be synthesized without the need for large manufacturing facilities, offering a route to attainable solar energy in developing countries. In addition to solar energy, nanomaterials have been prevalent in a wide variety of renewable energy devices; for example, carbon nanotubes have been used to strengthen the blades of windmills, and nanoparticles have been used to improve energy generation in geothermal systems [50].

A road map for cheaper and more versatile materials for solar energy devices has been in progress since the first silicon solar cell was sold commercially in 1955 with an efficiency of only 4% [136]. Since then, the advancement in solar cell technology has been included a variety of designs including amorphous and polycrystalline silicon thin films, polymer films with inorganic nanostructure components, and more recently nanoparticle and perovskite films [166]. Traditional silicon-based solar cells are the earliest commercial solar cells, though these are still the most efficient solar cells available commercially and make up the majority
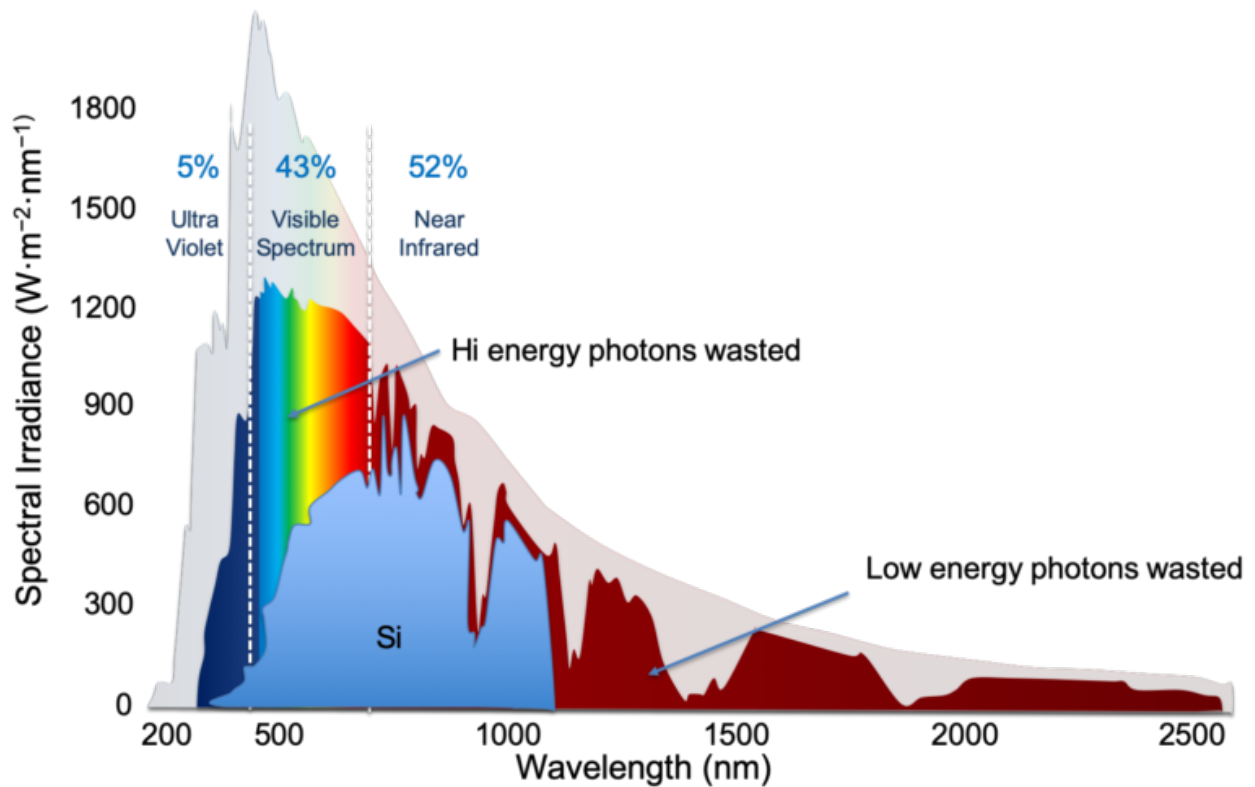
Figure 2.1: The solar energy spectrum compared to the theoretical maximum amount of energy that could be converted to electrical energy in a silicon solar cell. The gray area shows the total sunlight that reaches the earth, while the colored spectrum is the radiation that reaches sea level. Figure from Ref. [4]

of all of the devices that have been sold. The success of silicon solar cells can be attributed to its abundance as well as an ideal band gap of 1.12 eV which means that this material absorbs light at the maximum of the solar spectrum, as shown in Fig. 2.1. The energy range in which a material can absorb is tied closely with its conversion efficiency in a photovoltaic (PV) cell: PV cells work by absorbing some portion of solar radiation (sunlight) in the form of photons, which generate electron-hole pairs in the semiconductor materials that can then generate electrical currents and usable energy [50]. The greater percentage of the solar spectrum that the material (or materials) can absorb, the higher the device efficiency since less sunlight is wasted. However, there is a theoretical limit, called the Shockley-Queisser Limit [157], of approximately 33% for a PV cell made from a single (pristine) material. In the later generations of solar cell evolution, overcoming this theoretical limit has been a

primary goal through combining materials into multi-junction solar cells, doping materials with specific impurities, and using combinations of nanoparticles, nanoplatelets and other nanomaterials that can be uniquely tuned to have band gaps that cover the full range of the solar spectrum depending on their size and composition.

2.2 Nanoparticles for Solar Energy Applications

Solution-processed semiconductor nanoparticles (NPs) are a promising material class for PV cells to overcome the Shockley-Queisser limit, due to their tunable electronic and optical properties. Particularly combined with perovskites (which efficiently absorb high energy photons) or other unique materials, NPs have the potential to capture the full solar spectrum [4]. However, finding materials that absorb in the optimum energy range is not the only factor to consider for efficient devices.

When designing PV devices, in addition to an optimum band gap, a high carrier mobility is desired to maximize the apparatus efficiency. With the most NP devices, however, electron mobility is not competitive with bulk silicon since in the former, electron transfer occurs between different nano-objects with barriers between them due to ligands, packing density, etc [124, 86]. Thus, experimental and computational scientists are designing creative alternatives that maximize electron transport in NP arrays. One such option includes self-assembled superstructures, called nanoparticle solids or nanoparticle films, which have been realized experimentally using many different techniques and could be made from not only nanoparticles but other nano-objects as well. These NP solids are the "artificial atom" equivalent of a crystalline solid in which NPs are arranged in a grid-like fashion and therefore maintain their quantum properties while also improving long-range order and enhancing the migration of charge carriers. Although it is difficult to avoid disorder in NP size, position, orientation, and ligand arrangement, many groups have made breakthroughs in approaching the synthesis of a perfect NP solid as shown in Fig. 2.2 [124, 86].

As with an ordinary crystal lattice, the periodicity of the NPs in a perfect NP solid

7
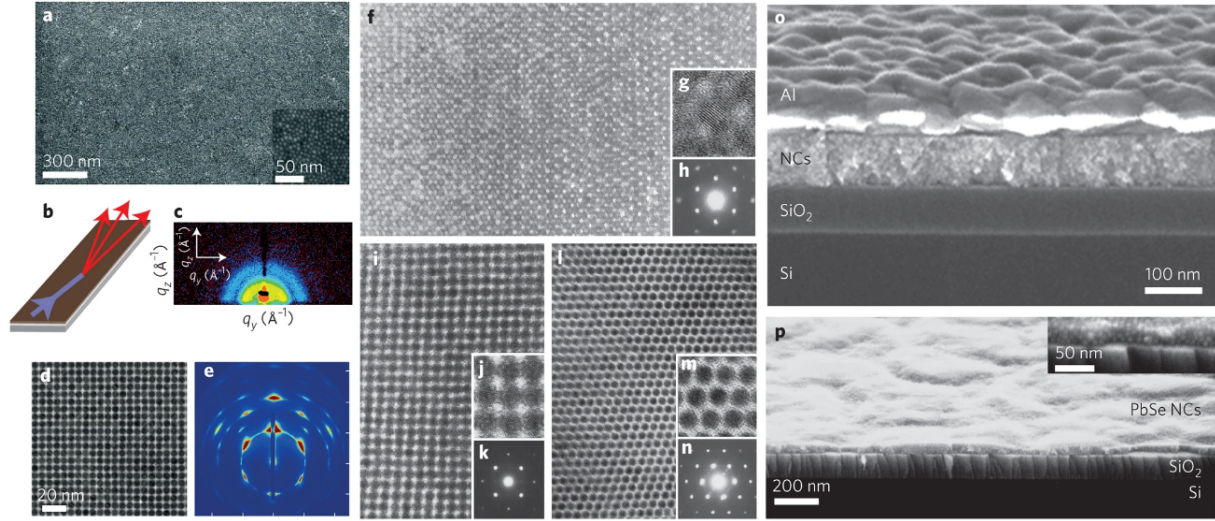
Figure 2.2: Figure and caption from Ref. [86]. **a-c**, Low-resolution (inset, high-resolution) SEM micrographs (**a**), and large-area GISAXS probing (**b,c**) of glassy, PbTe QD thin films. d,e, TEM (**d**) and GISAXS (**e**) images of PbS QD assemblies. **f-n**, CdSe QD superlattices for $< 111 >$ SL projection (**f-h**), $< 100 >$ SL projection (**i-k**) and $< 101 >$ SL projection (**l-n**),shown as low-resolution TEM images (**f,i,l**), high-resolution TEM images (**g,j,m**) and small-angle electron diffraction images (**h,k,n**). In **f,g,i,j,l,m**, each QD is 4.8 nm. **o**, Cross-sectional SEM image of CdSe QD solids. NCs, nanocrystals. **p**, Cross-sectional SEM image of PbSe QD solids. Figure reproduced with permission from: **a-c**, ref. [172], American Chemical Society; **d,e**, ref. [180], American Chemical Society; **f-n**, ref. [124], Annual Reviews; **o**, ref. [105], Nature Publishing Group; **p**, ref. [167], AAAS

may lead to the formation of energy bands due to interactions between atoms, with electronic wavefunctions delocalized over the whole solid and thus high electron mobilities on the order of 10-20 cm$^2 V^1 s^1$ may be obtained [124]. While some recent experimental studies [38, 86, 100] have demonstrated the existence of energy bands, in most cases the inherent disorder in particle size and alignment in a NP solid can cause localization of the wavefunctions on one or a few NPs, thus changing the way electrons are able to move throughout the solid [185] and decreasing the electron mobility. To summarize, moving from a perfectly ordered to a disordered structure affects the carrier mobility and these two extremes represent two completely different transport regimes: that of "band" transport, where electrons travel through the delocalized states (bands) of a crystal, and "hopping" transport, in which electrons tunnel between neighboring sites (NPs). Understanding the electronic structure and

optoelectronic properties of pristine and disordered interacting NPs, both from experimental and computational perspectives, is thus of vital importance for the design of efficient PV devices.

2.3 Nanoplatelets for Solar Energy Applications

While NP or QD films have been successfully integrated into solar cells with efficiencies in excess of 12% [101, 2], a vast collection of other nanomaterials are being considered to further improve these devices. One such class of nanomaterials includes strongly anisotropic, quasi-two dimensional nanoplatelets (NPLs), which have gained interest recently due to synthetic advancement [84, 77] that has greatly enhanced their ability to tune the optoelectronic properties. One such synthetic technique is colloidal Atomic Layer Deposition (c-ALD) [84, 77], which is similar to the gas-phase ALD technique used to deposit thin films of dielectric oxides, semiconductors and metals onto silicon wafers and other substrates. This method has been revolutionary in improving synthetic control, eliminating polydispersity, and creating nanoplatelets with atomic precision. c-ALD has even been used to create a library of complex semiconductor NPL heterostructures, in which individual layers of a NPL are made from different materials such as CdSe, CdS, and ZnS, as seen in Fig. 2.3c-d. These endless combinations of core/shell materials illustrate the unique role NPLs could play in the design of solar cell devices with precisely tunable absorption properties.

In addition to their tunable properties, NPLs also differ from NPs due to their strong anisotropy that leads to biaxial strain profiles (illustrated in Fig. 2.3b) which can change the relationship between structure and function compared to what one would expect in a spherically symmetric NP. In biaxial strain profiles, present in both single-material and heterostructured NPLs, a compressive strain (lattice contraction) in either the in-plane or axial direction is partially offset by a tensile strain (lattice expansion) in the other direction. This illustrates one reason that NPLs stand out among other nanomaterials: the biaxial strian in NPLs has a unique effect on the optical properties such as the band gap. Specifically,

it leads to an interplay between strain and quantum confinement that is not necessarily straightforward: the biaxial strain in CdSe NPLs, for example, leads to a reduction in the band gap compared to an ideal "unstrained" NPL regardless of whether the axial lattice constant is compressed or expanded. A competing effect is quantum confinement (QC), arising by expanding or compressing in the axial direction which either reduces or increases the band gap, respectively. For NPL heterostructures, the strain profiles can become more complex due to the presence of interfaces. Thus, the generation of NPL heterostructures with layers of different materials can be synthesized to precisely engineer the strain profiles and thus their interplay with quantum confinement.
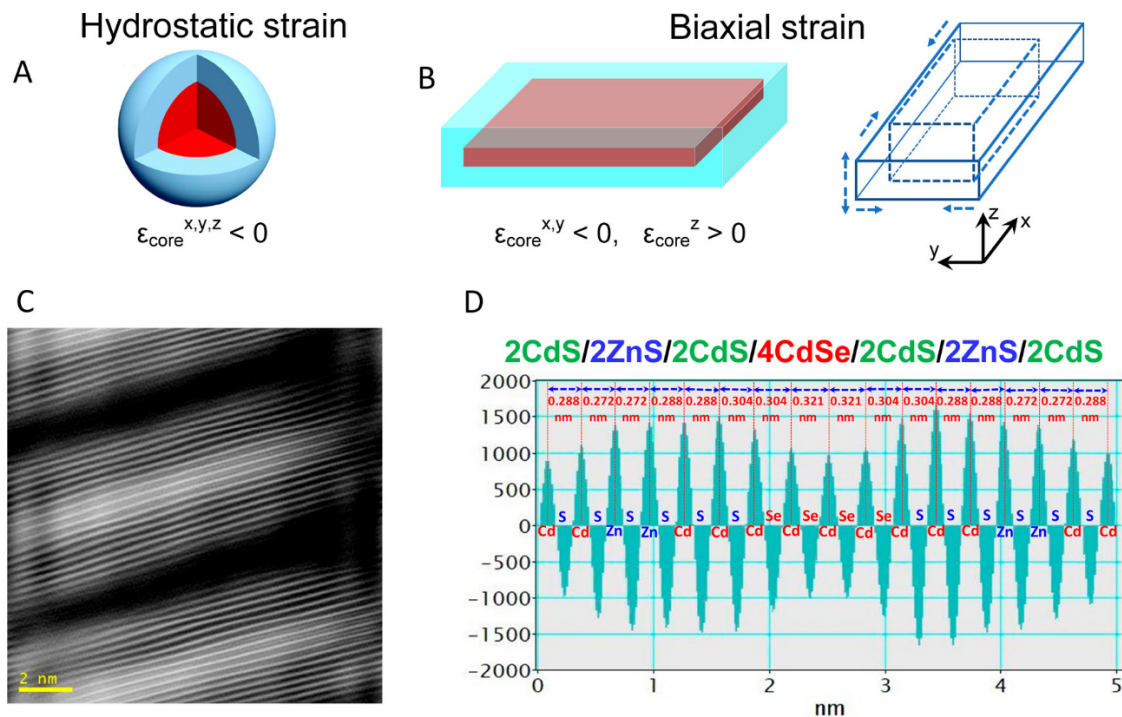
Figure 2.3: Figure and captain from Ref. [77]. Strain and tetragonal unit cell distortion in NPL heterostructures. (A, B) Comparison of strain caused by the lattice mismatch in coreshell nanostructures with spherical and NPL morphology. In a spherical QD, the core is hydrostatically strained while the NPL core is under biaxial strain: the lattice is compressed along the x and y coordinates and expanded along the z-axis, which is also the direction of strong quantum confinement. (C) HAADF-STEM image of 2CdS/2ZnS/2CdS/4CdSe/2CdS/2ZnS/2CdS and (D) the interplanar distances for this structure

In general, due to the synthetic control of these CdSe-based quasi-2D materials, their

optical absorption and photoluminescence (PL) spectra can be tuned with even greater precision than other nano-objects, with impressively narrow PL linewidths of less than 40 meV [77], almost half of what is typically observed in QDs [34]. This highly controlled tunability through the NPL thickness and layer-by-layer composition promises successful integration as photoabsorbers in PV devices. In fact, films of CdSe NPLs have already been demonstrated in PV devices [110], but these materials are much less established than their NP counterparts. Similarly to NP solids, NPLs are expected to be most successful in PV devices as assembled films where electrons can rapidly and efficiently move throughout the layer [144, 59]. NPLs have the additional benefits over NPs of straightforward 2D packing into a grid-like thin film and a unique relationship between quantum confinement and biaxial strain that introduces an additional level of control over their optoelectronic properties.

2.4   Metal-Organic Frameworks for Hydrogen Storage

Away from solar energy and nano-objects, we draw attention to a class of nanoporous materials called Metal Organic Frameworks (MOFs). Metal-Organic Frameworks are porous compounds that consist of an array of metal ions or clusters linked together by organic ligands, forming a unique cage-like structure. These vast two- or three- dimensional networks can be created in numerous shapes and patterns, with a wide variety of metal centers and organic materials, tuned depending on the desired optoelectric or magnetic properties and applications.

Due to the porous nature of these materials as well as their high surface area, they are a natural choice for applications such as gas storage [126, 121, 54], separation [29, 23], and heterogeneous catalysis [113, 187] because "guest" particles such as gas molecules can be absorbed into the pores. Depending on the composition of the metal centers and ligands, the MOF can be tuned to absorb different types of molecules, making it a particularly versatile class of materials. In addition to the common applications of hydrogen storage or catalysis, MOFs have been successfully used for the capture of carbon dioxide and other greenhouse

11

gases, potentially paving the way for the design of more efficient materials to capture carbon from the atmosphere or even from fossil fuel power plants to fight the greenhouse effect [122, 47].

CHAPTER 3

FIRST PRINCIPLES CALCULATIONS

3.1 Introduction

In this chapter, we present the theoretical background for the first principles methods that have been used in this dissertation to calculate the electronic structure of nanomaterials. First, we will provide an overview of Density Functional Theory (DFT), the framework for which the majority of our calculations are based upon. Then, we will discuss First Principles Molecular Dynamics (FPMD), which allows one to extend DFT to finite temperature simulations. Next, we will introduce Many Body Perturbation Theory (MBPT), and in particular the G_0W_0 approximation, which is a first principles technique that is more accurate yet more computationally demanding than DFT. Finally, we will discuss the application of first principles techniques to optical properties such as absorption spectra, through the use of the Bethe-Salpeter Equation.

3.2 Calculations of Ground State Properties using Density Functional Theory

3.2.1 Kohn-Sham Formulation

In non-relativistic Quantum Mechanics, the Schrödinger equation mathematically defines the wavefunctions of a system and thus fully describes the state of that system at each point in space and time. However, for all but the simplest systems (such as a single Hydrogen atom) it is impossible to analytically solve the Schrödinger equation exactly. Thus, a number of computational techniques and approximations have arisen over the past 50 years in an attempt to overcome this limitation and be able to accurately describe the electronic structure of complex many-body systems (i.e. systems containing more than one electron). Among the most popular and versatile of these methods is Density Functional Theory (DFT), which

is based upon the assertion that the ground state properties of a quantum-mechanical system can be fully described by their electron density rather than their wavefunctions. The popularity and success of DFT can be traced back to 1965, when the theorems of Pierre Hohenberg and Walter Kohn [80] gave DFT the theoretical and computational grounding necessary to potentially compete with other electronic structure methods. The Hohenberg-Kohn Theorems state the following:

1. The ground state of any interacting many particle system with a given fixed inter-particle interaction is a unique functional of the electron density n(r).

2. The electron density that minimizes the energy of the overall functional is the true electron density corresponding to the full solutions of the Schrödinger equation.

Essentially, the ground state wavefunction, and thus its energy, can be written as a unique functional of the ground state electron density (where a functional is defined as a function of a function). If this functional is known, then one can find the ground state energy by varying the electron density and finding where the energy is a minimum. However, the seminal paper by Hohenberg and Kohn provided no form for the universal functional.

One year after the Hohenberg-Kohn Theorems were published, Walter Kohn and Lu Jeu Sham [94] provided the final piece necessary to make DFT feasible and kick-started the modern era of electronic structure calculations. The Kohn-Sham Ansatz [94] stated that the ground state electron density of the many-body system can be written as a fictitious system of noninteracting particles with the same ground state electron density. Thus, it became possible to use a set of single particle equations that look like the Schrödinger equation and can be solved numerically. The Kohn-Sham Equations are:

$$\left(-\frac{1}{2}\nabla^2 + v_h(\mathbf{r}) + v_{xc}(\mathbf{r})\right)\phi_i(\mathbf{r}) = \epsilon_i\phi_i(\mathbf{r}) \tag{3.1}$$

where $n(\mathbf{r})$ is the electron density, $v_h(\mathbf{r})$ is the Hartree potential (the classic electrostatic potential), ϵ_i is the single particle energy, $\phi_i(\mathbf{r})$ is the single particle wavefunction, and $v_{xc}(\mathbf{r})$ is the so-called exchange-correlation potential (the functional derivative of the related exchange-correlation energy). While the Hartree potential is easy to calculate, the exact form of the exchange-correlation potential is unknown. Many different methods of approximating this exchange-correlation potential exist, and an overview of these choices will make up the next section of this chapter.

3.2.2 Approximations for the Exchange-Correlation Functional

On a basic level, the Exchange-Correlation potential is the term in the Kohn-Sham Equations that attempts to approximate the interactions between electrons that are not otherwise incorporated into the single particle equations. The Exchange interaction and Correlation interaction, which together make up this term, can be understood by the Pauli Exclusion Principle that is well known in chemistry: the exchange part comes from the repulsion energy between two electrons with parallel spins, and the correlation part includes the additional lowering of energy due to the electrons avoiding each other.

The simplest approximation to the Exchange-Correlation potential, which was introduced initially by J.P. Perdew and A. Zunger in 1981 [135], is the Local Density Approximation (LDA) which assumes that the electron density can be treated locally as a uniform electron gas. This approximation can be accurate for very uniform systems, but fails in cases where the density changes rapidly in different parts of the material. An improvement on the LDA, and what is used throughout most of this dissertation, is the Generalized Gradient Approximation (GGA) [102, 16], which instead of only using the local density also includes the gradient of the electron density at a given point in space:

$$E_{xc}^{GGA} = \int d\mathbf{r}\rho(\mathbf{r})\epsilon_{xc}^{GGA}(\rho(\mathbf{r}), \nabla\rho(\mathbf{r})) \tag{3.2}$$

where $\rho(\mathbf{r})$ is the electron density and ϵ_{xc}^{GGA} is the exchange-correlation energy per electron. In particular, in this work we use the parametrization of GGA by Perdew, Burke, and Enzerhof (PBE) [134], although others such as BLYP [16, 104] are common as well.

GGA is widely used throughout the computational physics, chemistry and even biology communities, and it is well known that this fairly inexpensive approximation can accurately describe structural properties such as bond lengths and satisfactorily predict trends in electronic structure properties such as band gaps. However, for quantitative comparisons to experiment, GGA is often not sufficient and more computationally expensive alternatives must be used.

One method for improving the quantitative accuracy of electronic structure calculations is the use of hybrid functionals, which combine GGA with a fraction of the Hartree Fock (HF) exchange, also known as the exact exchange self-energy (EXX). The HF method has been widely used in the chemistry community for longer than DFT. The general hybrid potential used in the KS equations of DFT is defined as:

$$v_{xc}^{hybrid}(\mathbf{r}, \mathbf{r}') = \alpha \Sigma_x(\mathbf{r}, \mathbf{r}') + (1 - \alpha)v_x(\mathbf{r}) + v_c(\mathbf{r}) \tag{3.3}$$

where Σ_x is the HF exact exchange, v_x is the GGA exchange potential, v_c is the GGA correlation potential, and α is the fraction of exact exchange used in the given hybrid functional. In practice, numerous suggestions for the best choice of α have been proposed. The commonly-used PBE0 functional [8] uses a constant $\alpha = 0.25$, while other more complex hybrid functionals select α based on material parameters such as the dielectric constant (see Section 3.2.3 below).

Further approximations to the exchange-correlation functional to improve the accuracy of DFT include range-separated hybrids and meta-GGAs, the latter of which depend on the kinetic energy density in addition to the electron density and density gradient [114]. In general,the trade-off between computational complexity and accuracy is something that drives many of the decisions made in the field of electronic structure calculations.

3.2.3 Dielectric-Dependent Hybrid Functionals

While numerous flavors of hybrid functionals exist, one particularly successful and physically motivated option is the dielectric-dependent hybrid functional, which was first introduced for solids in 2014 [158]. In this case, rather than using a constant fraction of exact exchange, for example $\alpha = 0.25$, the fraction is chosen as the inverse of the macroscopic dielectric constant of the material. The dielectric constant can be calculated self-consistently by calculating the dielectric screening using, for example, the method of Density Functional Perturbation Theory or the application of finite fields, as described in Section 3.4. Self-consistent dielectric-dependent hybrid calculations have been shown to be more accurate than PBE0 for many materials [26] and in excellent quantitative agreement with experiment.

The dielectric-dependent hybrid functional has been generalized to finite systems [28] such as molecules or nanoparticles, where the dielectric constant of the system is ill-defined. To overcome this limitation, the authors instead proposed that the fraction of exact exchange is defined as the ratio of the screened and unscreened exchange energies. It can be shown mathematically that, for bulk materials, this ratio reduces to the inverse of the dielectric constant. While this definition works for both finite and three-dimensional systems, its validity for the intermediate regime of two-dimensional materials, as well as a unifying functional spanning dimensionalities, has not been previously explored and is the subject of future work.

3.2.4 The Planewave Pseudopotential Method

So far in this chapter, we have discussed the foundations upon which the field of Density Functional Theory is built, but we have yet to address the computationally efficient, numerical techniques that make such calculations possible on real systems. In general, such techniques revolve around representing the Kohn-Sham orbitals with a basis set. While there exist a number of options of basis sets to use, the work in this dissertation has been performed using a planewave basis set with periodic boundary conditions, which is the ideal

option for condensed matter systems and can be used for isolated systems as well. The planewave basis set is a Fourier expansion of the wavefunction:

$$\psi_{i,\mathbf{k(r)}} = \sum_G c_{i,\mathbf{k},\mathbf{G}} e^{i(\mathbf{k}+\mathbf{G})\cdot r} \tag{3.4}$$

where the sum is over G, the reciprocal lattice vectors, $c_{i,\mathbf{k},\mathbf{G}}$ are the Fourier coefficients, and $\mathbf{k}$ is the k-point vector in the first Brillouin zone. The number of k-points included in the summation depends upon the system of interest; for isolated systems such as nanoparticles, there is no k-dependence and a single k-point ($\mathbf{k}$={0,0,0}, known as the Γ point) is used, but for 3D or 2D periodic systems such as bulk solids or 2D nanoplatelets, convergence of the electronic structure as a function of the size of the k-point grid is essential. Convergence with respect to the number of G vectors is required as well, with this number typically represented as an energy cutoff, E_{cut}.

One downside to the use of planewave basis sets in DFT is that the sharp features of the wavefunctions of the core electrons are prohibitively expensive to represent in this manner since doing so would require a massive number of planewaves. To overcome this limitation, planewave basis set calculations are coupled with pseudopotentials, in which the nuclei and the core electrons, which do not participate in chemical bonding, are not treated explicitly and are instead replaced by an effective potential. Doing so allows the valence electrons to be described by pseudowavefunctions that have fewer nodes than their all-electron counterparts. Each type of atomic species has its own pseudopotential, and there exist numerous forms of pseudopotentials such as Norm-Conserving [75], where the norm of the pseudowavefunction is required to be equal to the norm of the all-electron wavefunction within a cutoff radius, or Ultrasoft [174], where the norm-conserving requirement is relaxed in order to reduce the number of plane waves needed by splitting the valence electron density into "soft" (few nodes) and "hard" (many nodes) contributions. However, the choice of which electrons to include in the valence for a pseudopotential is not always straightforward, and this has led to the development of numerous different pseudopotentials that have been used throughout the

literature with varying levels of success for different systems and different levels of theory. Throughout this dissertation, the pseudopotentials used in each study are explicitly stated, and are chosen based on the level of theory and elements involved in each case.

3.3 First Principles Calculations at Finite Temperature

Density Functional Theory is an optimal electronic structure method to calculate static, ground state properties of a vast range of materials at T=0. However, when comparing calculations directly to experimental measurements, the inclusion of temperature effects is crucial because measurements are often performed at room temperature or above. Furthermore, probing structural dynamics, phase transitions or vibrational spectra of a system is only possible through the use of a dynamic calculation. Molecular dynamics offers a tool to simulate such dynamical properties of materials.

3.3.1 First Principles Molecular Dynamics

In Molecular Dynamics (MD) simulations, the positions and velocities of atoms in a system are calculated by numerically solving Newton's equation of motion:

$$m_i \ddot{\mathbf{R}}_{\mathbf{i}} = \mathbf{F}_{\mathbf{i}} \tag{3.5}$$

where m_i is the mass of the ith nuclei, $\ddot{\mathbf{R}}_{\mathbf{i}}$ is the acceleration of the ith nuclei, and $\mathbf{F}_{\mathbf{i}}$ are the forces (a derivative of the total energy). The forces acting upon each atom at each point in time are generally calculated in one of two ways: using an empirical interatomic potential, or using first principles techniques. Interatomic potentials or force fields are often computationally inexpensive to evaluate, but they are not easily transferable between systems (since force fields are designed for individual systems), may not adequately simulate changes in chemical bonding, and usually they are not as accurate as when the forces are calculated from first principles.

An alternative to classical force fields is First Principles Molecular Dynamics (FPMD), which offers a non-empirical method to calculate the forces and propagate the atomic trajectories with greater accuracy. While FPMD comes in two flavors, Born-Oppenheimer MD [118] and Carr-Parrinello MD [33], in this dissertation we will focus only on Born-Oppenheimer MD. At each time step in FPMD under the Born-Oppenheimer approximation, the energy, and thus the forces, are calculated using DFT and the KS equations. The derivative of the total energy, which allows one to calculate the forces, is evaluated by using the Hellmann-Feynman theorem [117], which relates the derivative of the total energy to the expectation value of the Hamiltonian. While FPMD is a much more accurate and flexible method than MD with interatomic potentials, due to its high computational cost it is only feasible for smaller systems and much shorter simulation times (up to a few hundred picoseconds, while nanoseconds of data can easily be collected using MD with empirical force fields).

3.4 Calculations of Dielectric Properties

In the previous two sections, we have presented a framework for calculating the electronic structure of materials at zero temperature and finite temperature using DFT and FPMD, respectively. In general, these methods allow us to calculate properties such as the most stable configuration of atom positions as well as the distribution of charge density and the positions of the energy levels (including band gaps and other energy differences, ionization potentials, etc). Of additional interest is an understanding of the way a system responds to perturbations from the environment - for example, the response to an external electric field, which opens up the possibility to calculate numerous dielectric properties such as the dielectric constant, polarizability, polarization, and dipole moment. These dielectric properties can be calculated in two different ways, both of which will be presented below.

3.4.1 Density Functional Perturbation Theory

The first commonly used method for calculating dielectric properties of materials from first principles is Density Functional Perturbation Theory (DFPT), which is used to study the linear response to an external perturbation and is implemented, for example, in the Quantum Espresso DFT code [61]. In addition to dielectric properties such as the polarizability or dipole moments, DFPT can be used to calculate the phonons in the system or its Raman spectra. In the DFPT formalism of Baroni [13, 12], the response to the external perturbation is calculated using the so-called Sternheimer equation:

$$\left(H^{(0)} - \varepsilon_i^{(0)}\right)|\psi_i^{(1)}\rangle = -\left(H^{(1)} - \varepsilon_i^{(1)}\right)|\psi_i^{(0)}\rangle \tag{3.6}$$

where $H^{(0)}$, $\varepsilon_i^{(0)}$, and $\psi_i^{(0)}$ are the unperturbed Kohn-Sham Hamiltonian, eigenvalues and Kohn-Sham orbitals, and $H^{(1)}$, $\varepsilon_i^{(1)}$, and $\psi_i^{(1)}$ are the first-order perturbations of the same quantities. In its simplest formulation, DFPT is valid for insulating and semiconducting materials with perturbations in the linear regime, although extensions of the method have been proposed to account for metallic systems [44] or to go beyond the linear response by including higher order perturbations [65]. Furthermore, the response to external perturbation includes the calculation of a local field correction term that is nontrivial and computationally demanding to compute for orbital-dependent hybrid functionals due to their explicit dependence on ψ_i, and thus for hybrid functionals the method of Finite Fields is often preferred (see Section 3.4.2) over DFPT.

3.4.2 Finite Field Method

The second common method for calculating dielectric properties of materials is through the use of explicitly applied external electric fields. Due to its explicit nature, the so-called Finite Field Method is more versatile than DFPT as it can be used to study the response to external electric fields in both the linear and nonlinear regimes through varying the strength of the

applied field. Furthermore, as mentioned in Section 3.4.1, the implementation of DFPT coupled with orbital-dependent functionals such as hybrid functionals is not straightforward, and thus the Finite Field method provides a simpler option to calculate highly accurate dielectric properties using hybrid functionals. Although both DFPT and Finite Field are used throughout this dissertation for benchmarking and comparisons, the latter technique has been chosen for most computations due to its flexibility. The Finite Field method is implemented, for example, in the Qbox code [3].

The dipole moments, polarization, and polarizability of a material are obtained through the use of maximally localized Wannier functions (MLWF) [119, 120] which allow one to calculate the position operator even in 2D- or 3D-periodic systems where it cannot be calculated directly as it is for isolated systems. MLWFs are localized linear combinations of Bloch orbitals; in contrast to the delocalized Bloch orbitals, however, the localized nature of MLWFs allow them to frequently be used as visualization tools for chemical bonding. As the simplest depiction, the center of charge for a MLWF gives one an indication of the "location" of an electron or electron pair. The position of the Wannier centers is defined as:

$$r_{n,i}^0 = \frac{L_i}{2\pi} \text{Im} \ln \langle w_n | e^{i\frac{2\pi}{L_i}r_i} | w_n \rangle \qquad (3.7)$$

where L_i is the ith cell dimension, and the Wannier functions w_n are obtained by applying a unitary transformation to the occupied Kohn-Sham eigenstates in order to minimize their spread [72].

For an isolated system such as a nanoparticle, the total dipole is defined as:

$$\mu = -2\sum_n (\mathbf{r}_n^0 + \Delta\mathbf{r}_n) + \sum_n Z_n \mathbf{r}_{n,ion} \qquad (3.8)$$

where Z_n is the ionic charge, $\mathbf{r}_{n,ion}$ are the positions of the ions, $\mathbf{r}_n^0$ is the position of the nth Wannier center and $\Delta\mathbf{r}_n$ is a correction to the position of the nth Wannier center due to the refinement procedure of M. Stengel and N. Spaldin [162, 179]. The factor of 2 accounts

for spin multiplicity.

For 3D- or 2D-periodic systems such as bulk materials or nanoplatelets, the dipole moment is ill-defined. Instead, The Modern Theory of Polarization [140, 175, 89] offers a method for the calculation of differences in polarization with respect to an origin. The polarization is calculated as:

$$\mathbf{P} = -\frac{2}{\Omega} \sum_n (\mathbf{r}_n^0 + \Delta\mathbf{r}_n) + \frac{1}{\Omega} \sum_n Z_n \mathbf{r}_{n,ion} \tag{3.9}$$

where Ω is the unit cell volume, and $\mathbf{r}_n^0$ are again the positions of the Wannier centers.

By analyzing the change in position of the MLWFs upon application of an electric field, the polarizability and dielectric constant of the material can easily be calculated. The polarizability tensor is defined as:

$$\alpha_{ij} = \Omega \frac{P_i(+\Delta E_j) - P_i(-\Delta E_j)}{2\Delta E_j} \tag{3.10}$$

where $P_i(\Delta E_j)$ denotes the polarization in the ith direction in response to an applied field ΔE_j in the jth direction. ΔE should be chosen to be small enough so as to ensure calculations are carried out in the linear response regime.

Finally, the dielectric tensors for solids can be obtained using finite differences with the same applied electric field:

$$\epsilon_{\infty,ij} = \delta_{ij} + \frac{4\pi\alpha_{ij}}{\Omega} \tag{3.11}$$

where δ_{ij} is the Kronecker delta, Ω is the unit cell volume, and α_{ij} is from Eq. 3.10. The high-frequency dielectric constant is then typically calculated as the trace of the dielectric tensor.

3.5 Many Body Perturbation Theory

Although Density Functional Theory has been widely successful at predicting structural and electronic properties of materials, especially when combined with the use of hybrid functionals, in several cases this level of theory is not sufficient to accurately describe excited state properties that compare well with experimental measurements. Many Body Perturbation Theory (MBPT) offers a method to calculate the excited state properties of materials with high accuracy. In particular, the GW method developed by Lars Hedin in 1965 [78] has become the premier electronic structure method for quantitative comparison to experiments such as direct and indirect photoemission, which measure the energy of the highest occupied and lowest unoccupied energy states through addition or removal of an electron [64].

MBPT starting from DFT single particle states has been shown to give energy levels, band gaps and other properties in close agreement with experiment for numerous classes of complex systems [81, 82, 55]. Particularly in the field of photovoltaics, which include solar energy conversion processes, GW has become a crucial technique to study the excited state properties of nanomaterials. However, until recently the high computational cost of this method has been prohibitive for all but the smallest systems or the most powerful computational resources. [66]

In the GW approximation, one can obtain quasiparticle (QP) states, Ψ_i^{QP}, and QP energies, E_i^{QP}, using an equation similar to the Kohn-Sham equation (Eq. 3.2.1):

$$\hat{H}^{QP} |\Psi_i^{QP}\rangle = E_i^{QP} |\Psi_i^{QP}\rangle \tag{3.12}$$

Here, the QP Hamiltonian, $\hat{H}^{\text{QP}}$ includes the self-energy operator Σ, rather than the exchange-correlation potential, v_{xc}, from Eq. 3.2.1:

$$\Sigma = iGW\Gamma \tag{3.13}$$

where G is the interacting one-particle Green's function and W is the screened Coulomb
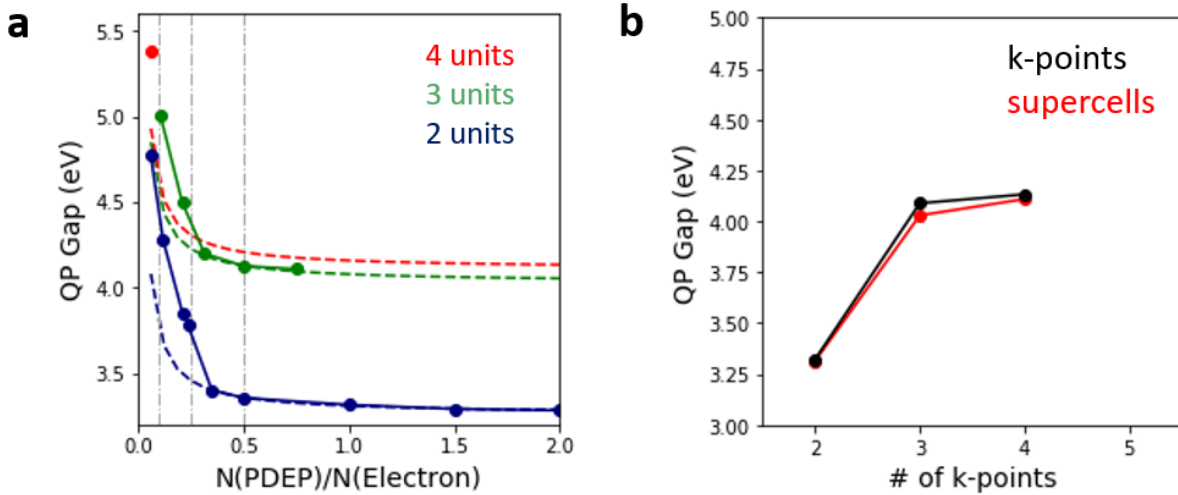
Figure 3.1: a) Convergence of the QP band gap of a 2ML CdSe nanoplatelet as a function of the number of PDEPs used in West, for 2x2, 3x3, and 4x4 unit supercells b) Comparison of the QP band gap using extrapolated values of infinite PDEP from supercells and direct calculations using k-points, where the number of electrons was reduced due to using a primitive unit cell.

interaction. Γ is the vertex operator [82], which in many approximations is taken to be the identity.

The work in this dissertation in particular uses the G_0W_0 approximation, in which the Green's function, G, and the screened Coulomb interaction, W, are calculated non-self-consistently from DFT wavefunctions. G_0W_0 calculations have been performed with the WEST code [66], which is optimized for large-scale calculations. We have also used Yambo [145, 115] in the cases where large k-point meshes were required.

G_0W_0 calculations in West are efficient in that there is no need to compute virtual electronic states and hence no need to converge QP gaps and energies as a function of the number of empty states that enter the calculation; in addition, one can go beyond the common plasmon pole approximation [63, 53, 161]. West uses the method of spectral decomposition of the static dielectric matrix (ϵ) through an algorithm called "Projective Dielectric Eigenpotential" (PDEP), in which the Sternheimer equation is solved iteratively using Density Functional Perturbation Theory (see Section 3.4.1) [148], in order to find the

eigenvectors of the dielectric matrix. While convergence with empty states is not necessary, it is essential to converge QP energies with respect to the number of PDEPs included in the spectral decomposition of the dielectric matrix, as shown in Fig. 3.1 for a 2ML CdSe nanoplatelet. In particular, the number of PDEPs required is proportional to the number of electrons in the system, and typically a $n_{PDEP}/n_{electron}$ ratio of at least 1 or 2 is necessary before extrapolations can be obtained (see Fig. 3.1a) [183].

3.5.1   Pseudopotential Considerations Using GW

As discussed in Section 3.2.4, the choice of pseudopotentials may strongly depend on the level of theory used in a calculation. In particular, Scherpelz *et al.* [148] found that the accuracy of G_0W_0 calculations depend on which electrons are included in the valence partition of the pseudopotential. For a number of compounds with d electrons, G_0W_0 calculations only gave band gaps in agreement with experiment when the valence partition included the corresponding s and p electrons of the same shell as the d electrons, despite the s and p electrons not participating in the chemical bonding. For example, for the element Cadmium with electron configuration $[Kr]4d^{10}5s^2$, it is essential to include the $4p^6$ and $4s^2$ electrons in the valence as well as $4d^{10}$ and $5s^2$.

The selection (and development) of pseudopotentials can be further complicated, however, as we have found that even in cases where the valence configuration adheres to the suggestions of Scherpelz *et al.* [148] the G_0W_0 quasiparticle band gaps can differ by over 0.5 eV using different pseudopotential parametrizations. For example, Scherpelz *et al.* showed that the gaps of CdS, GaAs and zinc compounds varied depending on the choice of two different Optimized Norm-Conserving Vanderbilt (ONCV) pseudopotentials: SG15 [74] and PseudoDojo [173], derived with the same valence partition. In this dissertation, we have found that CdSe additionally shows a similar discrepancy between ONCV SG15 and PseudoDojo. The G_0W_0 quasiparticle gaps and experimental gaps for CdSe and CdS are summarized in Table 3.1.

26

Table 3.1: Summary of quasiparticle band gaps for CdSe and CdS computed using SG15 and PseudoDojo pseudopotentials

system	SG15	PseudoDojo	exp.
CdSe	0.48 eV	1.57 eV	1.70 eV
CdS	1.77 eV	2.23 eV	2.42 eV

To understand the source of this discrepancy, in Fig. 3.2 we plot the pseudowavefunctions compared to their all-electron counterparts for the SG15 and PseudoDojo pseudopotentials of Cd, S, and Se, the elements of interest for the nanoplatelets studied in Chapter 5. We note that, for Cd and S, the valence partitions are identical for SG15 and PseudoDojo: $4s^24p^64d^{10}5s^2$ and $3s^23p^4$ for Cd and S, respectively. For Se, however, the SG15 parametrization uses a valence partition of the full n=4 shell ($4s^24p^4$), while the PseudoDojo parametrization additionally includes the lower-lying 3d electrons in the valence ($3d^{10}4s^24p^4$). By comparing the quasiparticle gaps of CdSe in Table 3.1, we find that the inclusion of the 3d shell in the valence is essential to reproduce a band gap within 0.1 eV of experiment, whereas failing to do so underestimates the gap by 0.6 eV.

For the case of S, however, the distinction is not so clear as the valence configurations are indistinguishable. By comparing the pseudowavefunctions of S for both SG15 and PseudoDojo (Fig. 3.2, right column), we find that despite identical valence configurations, the PseudoDojo S pseudopotential is configured with a 3d projector function which is not present for SG15. Furthermore, for the Se pseudopotential, the SG15 parametrization is generated with a 4d projector (though the 4d electrons are not included in the valence), while PseudoDojo uses both the 3d projector and 3d valence electrons. The subtle differences in pseudopotential generation are found to significantly affect the band gaps of these materials at the G_0W_0 level of theory; however, we note that the electronic and structural properties at the PBE level of theory are not affected.
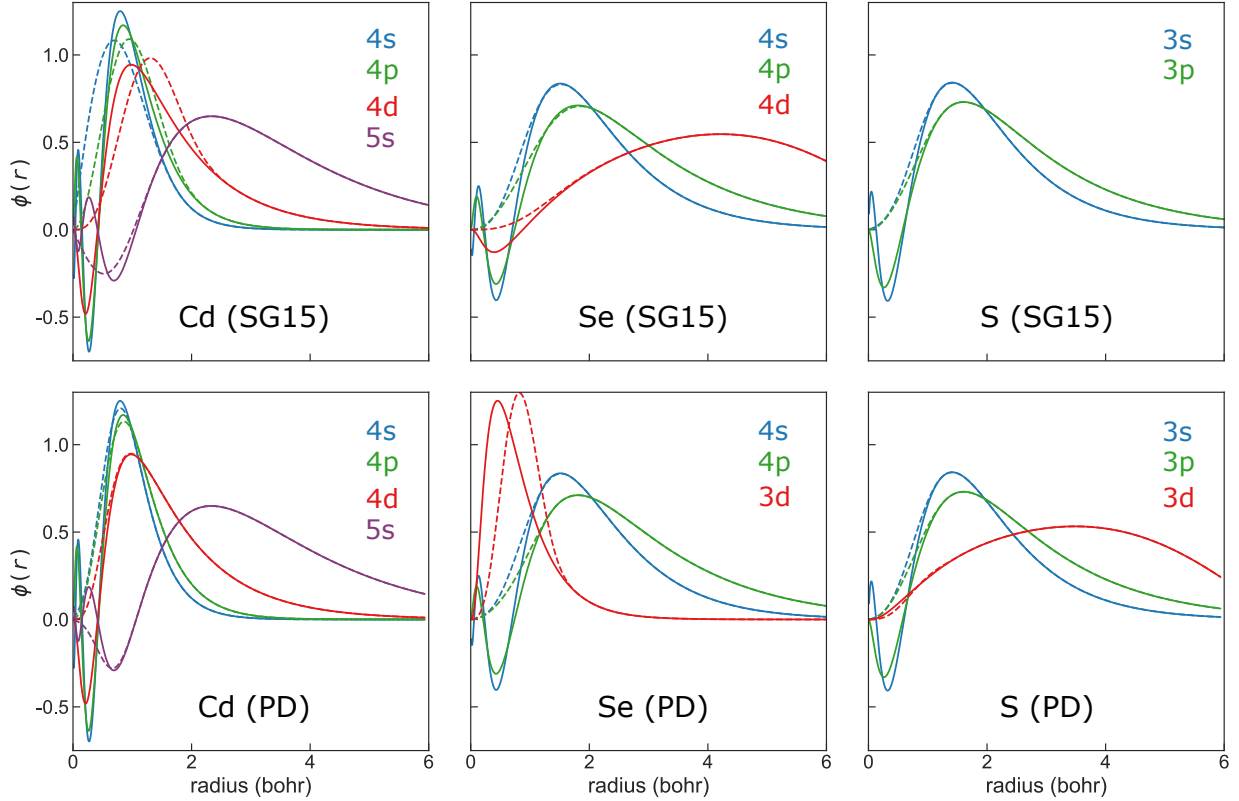
Figure 3.2: Pseudo- (dotted lines) and all-electron (solid lines) wavefunctions of Cd, Se, and S for SG15 (top) and PseudoDojo (bottom) pseudopotentials.

3.6 Calculations of Optical Properties and Absorption Spectra

In addition to quasiparticle energies, in the field of photovoltaics an understanding of the absorption spectrum of a material is crucial since the materials are targeted to absorb in a certain energy range. For example the optical band gap, which is determined experimentally by the onset of the absorption spectrum measured by i.e. UV-Vis spectroscopy, is different from the so-called fundamental band gap calculated with DFT or GW (the difference between the highest occupied and lowest unoccupied energy levels) because the latter does not include the interactions between the electron and hole formed through the excitation that results from the incident light in spectroscopy measurements. The difference between the fundamental band gap, $E_{g,fund}$, and the optical band gap, $E_{g,opt}$, is the exciton binding energy, E_b, which measures the energy it takes to form a bound electron-hole pair (an exciton)

in a semiconductor or insulator:

$$E_{g,opt} = E_{g,fund} - E_b \tag{3.14}$$

Especially for materials with strong excitonic effects, including the nanomaterials studied in this dissertation, direct comparison with experiment cannot be done without an understanding of the optical as well as fundamental band gaps.

We thus conclude this chapter with a brief discussion on the calculation of absorption spectra from first-principles, which enables one to determine the optical band gap and exciton binding energy to compare calculations to experimental optical absorption measurements. In optical absorption spectroscopy, the incident light excites electrons from occupied to empty energy levels. For a periodic solid system, the absorption coefficient $I(\omega)$ is given by the imaginary part of the macroscopic dielectric function, called $\varepsilon_2(\omega)$, while for a finite system the absorption spectrum is proportional to the trace of the dynamical polarizability tensor $\alpha(\omega)$ [141]. In the sections below, we will focus on methods used to calculate the absorption spectrum for periodic systems, and thus present equations for calculating $\varepsilon_2(\omega)$.

3.6.1   Independent Particle Approximation

Before considering excitonic effects, one can obtain a very basic approximation of the imaginary part of the dielectric function of a material through the Independent Particle Approximation (IPA) which gives the transition rate between occupied and unoccupied energy states using Fermi's Golden Rule [186]:

$$\epsilon_{ij} = \frac{1}{\omega^2} \sum_k \sum_{i \in V} \sum_{j \in C} \langle u_{j,k} | \hat{e} \cdot p_{ij} | u_{i,k} \rangle^2 \, \delta \left(E_j(k) - E_i(k) - \omega \right) \tag{3.15}$$

where p_{ij} is the transition matrix element between two single particle Bloch functions $u_{i,k}$ and $u_{j,k}$ with energies $E_i(k)$ and $E_j(k)$, considering interband transitions between states i in the valence band, V, and states j in the conduction band, C, with transition energy ω.
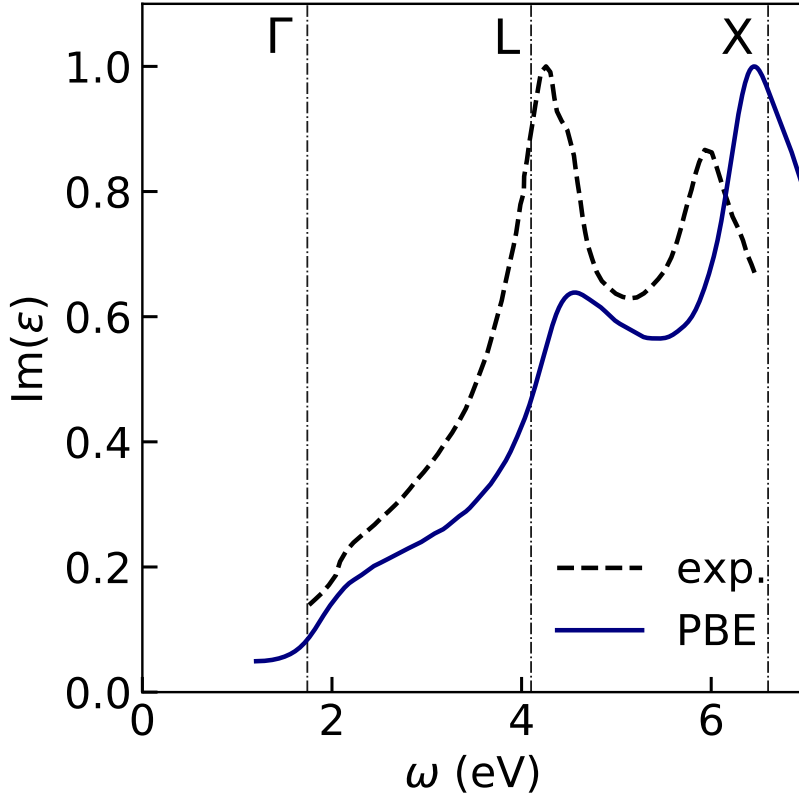
Figure 3.3: IPA spectrum of bulk CdSe calculated at the PBE level of theory, shifted by the difference between experimental and PBE band gaps, compared to the experimental spectrum [88]. Vertical dotted lines represent the calculated HOMO-LUMO transitions at high-symmetry points.

Only transitions in which the electron momentum, **k**, is conserved are considered. The IPA spectrum is closely connected to the Joint Density of States, which is simply the density of the transition energies between occupied and unoccupied states, or in other words the number of states per unit volume available for photons of a given energy to be absorbed or emitted. For systems with negligible excitonic effects, i.e. small exciton binding energies, the IPA spectrum can be in decent agreement with experimental measurements of the imaginary dielectric constant, as shown in Fig. 3.3 for bulk CdSe which has an exciton binding energy of approximately 20 meV [88].

3.6.2   The Bethe-Salpeter Equation

The final method that we will discuss in this chapter is the solution of the Bethe-Salpeter Equation (BSE) for the calculation of neutral excitations such as those involved in optical absorption spectra or energy loss spectra. Much like GW, BSE is based upon MBPT and the Green's function formalism [137]. While GW techniques incorporate a single-particle Green's function to compute electronic excitations involving the addition or removal of an electron, approximate solutions of the BSE are obtained with two-particle Green's functions, where the interaction between two quasiparticles – the electron and the hole – is described. Because BSE includes interactions between the electron and hole (together forming an exciton), this method has been widely successful in calculating optical band gaps and absorption spectra in good agreement with experiment [107]. Of the methods discussed in this dissertation, the complexity of BSE is the most computationally demanding. However, recent advances have provided ways to reduce the computational cost, for example by eliminating the need to sum over all empty states for both molecules [141] and solids [142].

In the two-particle Green's function formulation, the correlation between the electron and hole can be written as a product of single-particle Green's functions [137]:

$$iL(1, 2; 1', 2') = -G^{(2)}(1, 2; 1', 2') + G^{(1)}(1, 1')G^{(1)}(2, 2') \tag{3.16}$$

where $G^{(2)}(1, 2; 1', 2')$ is the two-particle Green's function and the second term is the product of two single-particle Green's functions and gives the independent evolution of the electron and hole. The correlation function L can then be used for the Bethe-Salpeter equation:

$$L(1, 2; 1', 2') = L_0(1, 2; 1', 2') + \int d3456 L_0(1, 4; 1', 3)\Xi(3, 5; 4, 6)L(6, 2; 5, 2') \tag{3.17}$$

where $iL(1, 2; 1', 2') = G^{(1)}(1, 2')G^{(1)}(2, 1')$ and Ξ is a kernel that gives the effective two-particle interaction that is the sum of the derivative of the Hartree potential and the self-

31

energy, Σ, from Eq. 3.13. Thus, the Bethe-Salpeter equation relates the correlation function L to the variation of the self-energy with respect to G [137]. Practically, different approximations can be made to the single-particle Green's functions and kernel Ξ to be used in modelling absorption experiments.

For the calculation of absorption spectra using BSE (as well as for GW calculations), the dielectric matrix (a microscopic quantity) can be calculated using a plane-wave representation as:

$$\epsilon^{-1}(\mathbf{r},\mathbf{r'}) = \frac{1}{\Omega} \sum_{q,G,G'} e^{i(q+G)\cdot r} \epsilon^{-1}_{G,G'}(\mathbf{q}) e^{-i(q+G')\cdot r'} \qquad (3.18)$$

where Ω is the volume, $\mathbf{q}$ is the transferred momentum, and G,G' are the reciprocal lattice vectors. The macroscopic dielectric function, the imaginary part of which gives the absorption coefficient, is then:

$$\epsilon^M = \lim_{q \to 0} \frac{1}{\epsilon^{-1}_{G=0,G'=0}(\mathbf{q},\omega)} \qquad (3.19)$$

While Eq. 3.19 technically requires calculating and inverting the full matrix, in practice the dielectric function can be calculated through an effective two-particle operator, where its eigenvalues correspond to the excitation energies of the system [137].

As this method requires solving a large eigenvalue problem, there are often a number of numerical techniques and choices to make this step feasible, for example the use of an iterative Lanczos-Haydock algorithm [19]. In this dissertation, all BSE calculations have been performed using the Yambo code [115] using the Lanczos-Haydock solver, as this code has been optimized for extended systems such as bulk materials and 2D NPLs which are the systems of interest in Chapter 5. Finally, we note that an additional method, Time-Dependent Density Functional Theory (TD-DFT) has been shown to give absorption spectra in decent agreement with experiment particularly when combined with the use of hybrid functionals (Section 3.2.2) [103]. However, this method will not be discussed in detail here,

as it has not been used in this dissertation. In Fig. 3.4, an example of a comparison of ε_2 is presented for BSE, TD-DFT using LDA wavefunctions, and experiment.
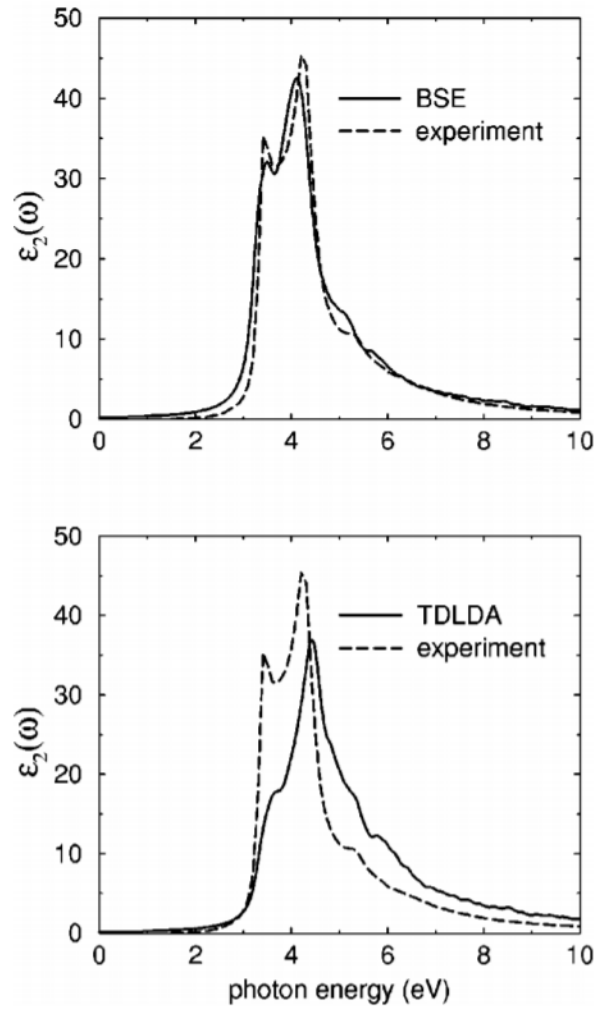
Figure 3.4: Imaginary part of the macroscopic dielectric function of bulk Silicon, illustrating the agreement between BSE and experiment and showing comparison to TD-DFT calculations. Figure taken from [18].

CHAPTER 4

SIMULATIONS OF INTERACTING NANOPARTICLES AT FINITE TEMPERATURE

4.1 Introduction

In this chapter, we use the methods presented in Chapter 3 to calculate the finite temperature electronic structure of isolated and interacting nanoparticles. We begin by introducing the application of semiconducting nanoparticles for next generation photovoltaic devices, and remark upon the current state of experimental and computational research in this area. In Section 4.2, we lay out our computational strategy to investigate these nanomaterials, including the electronic structure methods employed as well as the structural models we chose to use. Next, in Section 4.3 we present our results of the optoelectronic properties of isolated nanoparticles. We illustrate how these properties change as a function of temperature, and analyze our calculated dipole moments of isolated nanoparticles in comparison to various literature reports, showing that the vast discrepancies in the literature stem from sensitivity to temperature fluctuations, ligands, and interactions between nearby nanoparticles even in dilute systems. Finally, in Section 4.4, we compare the electronic structure and optoelectronic properties of isolated nanoparticles to interacting nanoparticle solids, showing the emergence of electronic and dielectric properties that are very different from their isolated counterparts.

4.1.1 State of the Art of Calculations and Experiments for Semiconducting Nanoparticles

Semiconducting colloidal nanoparticles (NPs) are promising candidates for next generation photovoltaic devices due to their tunable electronic and optical properties [125, 143, 111, 156, 95]. In particular, lead chalcogenide quantum dots have a large exciton Bohr radius (18 nm for PbS), leading to strong quantum confinement and hence a band gap that can be tuned over the solar spectrum by changing the NP size. Recently, halide-capped PbS NPs [169, 190, 42, 101] have been successfully integrated into certified solar cell devices with efficiency in excess of 12% [101, 2], which could be further improved and potentially even pushed beyond the Shockley-Queisser limit by exploiting the efficient multiple exciton generation observed in PbS NPs. [157, 76, 68, 152, 151, 90, 133, 127] In addition to tunable band gaps, the frontier orbital energies (or band edges) of these NPs may be tuned by choosing appropriate ligands; [30, 98] for example they could be tuned with respect to the redox potentials of water, CO_2 or H_2S, thus allowing for the design of novel and efficient photoabsorbers for photoelectrochemical cells. [184]

In NP based solar cells, quantum dots are assembled into films [39, 25, 124] where charge transport usually occurs via hopping, possibly leading to low mobilities [191, 9, 38, 185]. It is often assumed that mobilities can be enhanced by precisely arranging the dots into ordered solids, or by decreasing the distance between NPs [96, 35]. For example, epitaxially-connected NP superlattices [147, 182] and ultrathin 2D sheets of PbS NPs [149] have been synthesized, and the formation mechanisms of 2D and 3D NP superstructures have been studied using X-ray scattering experiments, electron microscopy, and Monte Carlo simulations [181, 60]. Treml *et al.* used successive ionic layer adsorption and reaction (SILAR) to enhance interdot coupling [171] in similar epitaxially-connected NP assemblies, while Dolzhnikov *et al.* [46, 85] used composition-matched molecular "solders" to increase carrier mobilities between NPs.

Despite the importance of NP interactions to understand and predict the properties of energy conversion devices composed of quantum dots, most theoretical and computational studies to date have addressed isolated NPs at zero temperature (T). Only a few finite temperature simulations of isolated Ge and Si NPs [56, 57] and of PbSe and CdSe [87,

62] NPs have appeared in the literature. Recent studies on the interactions of 2D PbSe nanoplatelets [93] and hydrogenated Si NP dimers [58, 67] and CdSe NP solids [178] have neglected temperature effects altogether. To our knowledge, no atomistic studies have been conducted previously on nanostructured lead chalcogenide solids that include at the same time the effects of temperature, NP interactions and that consider realistic capping ligands.

4.2   Computational Framework

We present a first principles study of the finite temperature properties of PbS NPs assembled into solids. We used First Principles Molecular Dynamics (FPMD) to investigate the modification of the electronic and dielectric properties of 1.6 nm iodine-capped lead sulfide NPs ($Pb_{32}S_{28}I_8$) upon formation of thin films. In order to assess the effect of interaction strength on the optoelectronic properties of NPs, we compared the properties of isolated NPs to those of interacting ones in two regimes: the first regime represents an assembly in which the NPs are kept apart by the ligands (similar to what is observed in spin-cast or drop-cast experimental films [111, 167]), and where the NPs are interacting but not covalently bonded; the second regime is representative of chemically bonded NP solids, or "connected NP solids." [147, 15, 46, 182] The models built in this work, labelled "necked" and "fused" solids, are illustrated in the two right-most panels of Fig. 4.1. The left-most panel represents the isolated NP, while the second panel shows the weakly interacting regime. The subunits for the necked solid remain largely intact, with the bonds between NPs occurring at the edges (or "neck") of the unit, whereas the NPs in the fused solid are strongly bound and they arrange into a periodic sheet of units fused together. Although these models represent only two possible bonding geometries, they are expected to be representative of epitaxially-connected structures synthesized by several groups using techniques designed to enhance electronic coupling [189, 108, 171, 147].

For each of our NP models, we chose to cover the surfaces with iodide ligands, as these are employed in experiments to prevent oxidative attacks and thus improve air-stability [128].

36
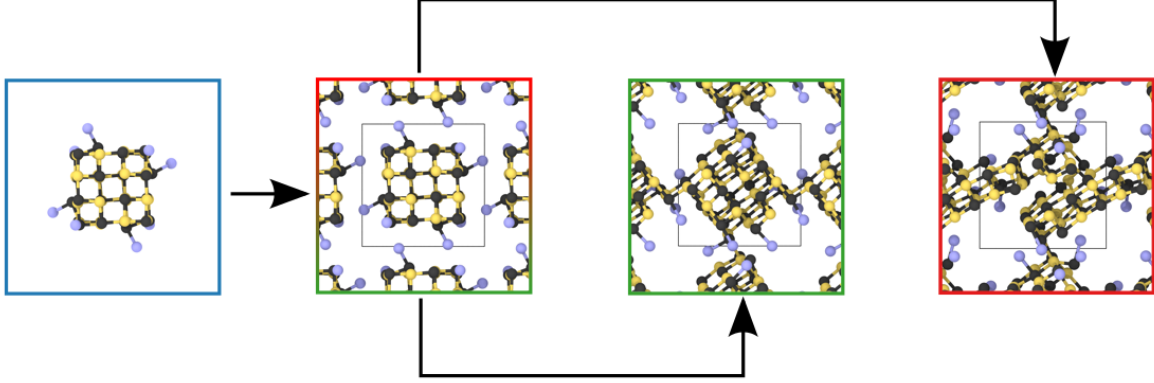
Figure 4.1: Ball and stick representation of the nanoparticles (NPs) considered in this work; from left to right: isolated $Pb_{32}S_{28}I_8$ NP; solid of weakly interacting NPs; necked and fused solids of NPs forming bonds (simulation cell shown as inner black box). Black, yellow and purple spheres indicate lead, sulfur, and iodine atoms, respectively.

Although smaller than those usually considered experimentally (often 3-10 nm in diameter), the NPs studied here are representative models of experimental quantum dots, inclusive of a core and a surface with cation excess, whose charge is compensated for by an appropriate number of anionic ligands.

Finite temperature NP structures from FPMD were generated using the Qbox code [3, 71], and electronic structure calculations were conducted with both Qbox [3, 71] and Quantum Espresso, [61] using plane wave basis sets (with cutoff of 60 Ry) and ONCV pseudopotentials [74]. In all cases, we used Density Functional Theory (DFT) under the Generalized Gradient Approximation with Perdew-Burke-Ernzerhof (PBE) parametrization [134]. FPMD simulations of the isolated NPs were performed in a unit cell with a lattice constant of 23 Å (corresponding to a vacuum of at least 8 Å between periodic images). For the calculations of the dipoles and polarizabilities, the lattice constant was increased to 30 Å (15 Å vacuum) as the convergence of these properties as a function of cell size is slower than that of the total energy [97]. FPMD simulations were performed using the Bussi-Donadio-Parrinello thermostat [31] with a time step of 2 fs.

A summary of computational parameters for the simulations in the text are presented in Table 4.1. The difference in structures between the fused and necked solid stems from using

Table 4.1: Summary of simulation details for the higher temperature simulations (target T=600 K), showing the only difference in initial parameters for the fused and necked solids.

System	Equilibration T (K)	Thermostat time constant (τ, fs)
isolated NP	511±39	200
fused solid	508± 43	200
necked solid	510± 42	20 for equilibration, 200 after 10 ps

two different coupling strengths of the thermostat during the initial phase of the simulations. The fused solid was generated using a weak thermostat coupling (large thermostat time constant), while the necked solid was generated with a stronger thermostat coupling, which was then set to be equal to the one adopted for the fused solid during the equilibration portion of the MD simulations.

After short simulation times of about 3 ps, we observed the NP building blocks merge into connected units to form either the necked or the fused solid. For both simulations, the temperature resulted to be approximately 510 K and configurations extracted from the initial 3 ps were considered as representative of weakly interacting NPs.

We then continued the simulations of the solids at 510 K (for approximately 80 ps) to investigate whether additional transformations would occur. After the initial, fast formation of the fused solid, we observed major structural changes. In particular, after 30 ps of simulation time, the 2D NP film initially obtained formed a 3D network bridged by ligands between the fused sheets, which then remained intact for the remainder of the simulation. In contrast, after formation of the 2D necked solid, only minor structural reorganization occurred with ligands migrating to and from the "neck" between NPs.

The simulations with a target temperature of 300 K were generated starting from initial configurations from the 600 K simulations. The target temperature was then lowered to 300 K and allowed to equilibrate before calculation of the properties present in the text. Similarly, the radiative lifetimes and band gaps for the solids presented at T=0 were achieved by systematically lowering the target simulation temperature from 600 K to 300 and then 150, 50 and 0 to facilitate a smooth quenching of the structures.

The dipole moments, polarization, and polarizability were obtained by calculating maximally localized Wannier functions (MLWF) [119, 120], as described in detail in Section 3.4.2.

4.3 Electronic Structure of Isolated Nanoparticles

4.3.1 Including Disorder Through Temperature Fluctuations

In experimental NP synthesis, one source of disorder in a NP film is due to the existence of a multitude of possible NP structures, or microstates, that are accessible at a given temperature. Furthermore, with even the most precise temperature control, small fluctuations in temperature will introduce additional disorder. As NP films are neither synthesized nor stored at zero temperature, it is impossible to eliminate this level of disorder and thus it is essential to understand its effect on properties of interest from a computational standpoint.

In order to assess the effect of interaction strength on the electronic and dielectric properties of disordered NPs at finite temperature, we first investigated the electronic structure of the isolated $Pb_{32}S_{28}I_8$ NP at approximately 250 K and 510 K. At both temperatures, simulations started from the 0 K relaxed geometry. To illustrate the effect of temperature on the electronic structure of the isolated NP, the electronic energy levels and wave functions were calculated in Qbox [71] using snapshots of the MD trajectories over 10 ps taken every 0.1 ps, for a total of 100 finite temperature structures per simulation (results obtained with 200 snapshots by decreasing the spacing between snapshots yielded the same average values).

The blue curve in Fig. 4.3a shows the calculated band gap (E_g) for the isolated NP. We found that the band gap decreases linearly as a function of temperature, and we observed a band gap decrease from 1.93 eV at 0 K to 1.75 ± 0.06 eV at 250 K and 1.54 ± 0.11 eV at 510 K. The calculated slope was found to be -0.8 meV/K. We remark that calculations were performed using the PBE exchange correlation functional, which is known to underestimate the magnitude of the fundamental band gap, but it is expected to accurately reproduce
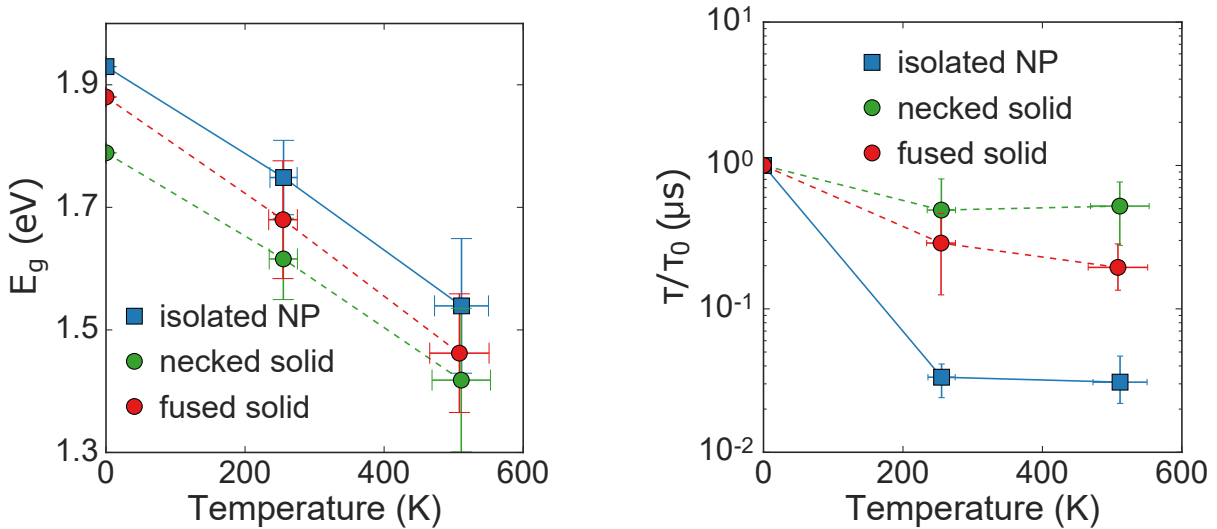
Figure 4.2: Left: Fundamental gaps as a function of temperature, computed as differences between the energies of the lowest unoccupied and highest occupied single particle states using DFT and the PBE functional. Right: Ratio of radiative lifetimes (τ) as a function of temperature, where τ_0 is the value computed at T=0; calculations were carried out at the DFT-PBE level of theory (see text).

qualitative trends [106, 21]; we also note that the gaps of the small NPs considered here correspond to an experimental gap of larger NPs. The decrease in band gap with increasing temperature is in contrast to what is observed in bulk lead chalcogenides [131, 45, 43] and for larger NPs with diameter of approximately 4 nm [165], but it is consistent with some experimental reports [131, 112] of a negative $\frac{dE_g}{dT}$ for PbS NPs below approximately 4 nm in diameter. However, other experimental studies reported a positive $\frac{dE_g}{dT}$ for PbS NPs with diameter larger than 3 nm, with the magnitude of the slope decreasing as a function of diameter [193].

To investigate the effect of NP size, we also calculated the electronic structure of a larger NP ($Pb_{62}S_{55}I_{14}$, which has the same cubic shape as $Pb_{32}S_{28}I_8$ but includes one additional layer of atoms leading to a diameter of 2.1 nm). The band gap of this NP was calculated as an average value of results for 15 configurations taken over 7 ps during a 540 K simulation, as well as at T=0. we found a similar trend in band gap as a function of temperature for this system, with a slope of approximately -0.6 meV/K compared to -0.8 meV/K for the

isolated $Pb_{32}S_{28}I_8$ NP. We calculated the average band gap to be 1.15 ± 0.1 eV compared to 1.48 eV at T=0.
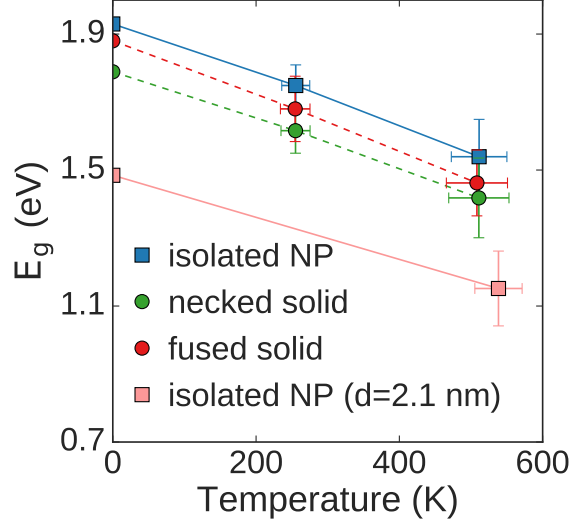
Figure 4.3: Fundamental gaps as a function of temperature, computed as differences between the energies of the lowest unoccupied and highest occupied single particle states using DFT and the PBE functional. The data for $Pb_{62}S_{55}I_{14}$ (d=2.1 nm) are included in addition to the isolated $Pb_{32}S_{28}I_8$ NP (d=1.6 nm) and the two solids formed from $Pb_{32}S_{28}I_8$ units.

4.3.2 Radiative Lifetimes of Isolated Nanoparticles

Due to the interest in PbS NPs for photovoltaic applications, we calculated Boltzmann-averaged radiative lifetimes of the charge carriers, which include the transitions accessible at the simulation temperatures:

$$\langle \tau \rangle = \frac{\sum_{if} \tau_{if} e^{-\omega_{if}/k_B T}}{\sum_{if} e^{-\omega_{if}/k_B T}} \tag{4.1}$$

where τ_{if} was calculated in the dipole approximation [27, 32] with the Quantum Espresso code: [61]

$$\tau_{if} = \left(\frac{4n\alpha_{FS}\omega_{if}^3}{3c^2} \frac{1}{3} \sum_{r \in x,y,z} |\langle\psi_i|r|\psi_f\rangle|^2 \right)^{-1} \tag{4.2}$$

Here, τ_{if} is the radiative lifetime of the transition from the occupied state i to the unoccupied state f with energy $\omega_{if} = \epsilon_f - \epsilon_i$ (ϵ_i is the energy of state i); n is the index of refraction; α_{FS} is the fine-structure constant; the matrix element is the transition dipole moment between states i and f computed using density functional perturbation theory techniques [12]. The ratio of radiative lifetimes τ to the value at T=0 are reported in Fig. 4.3b. For the Boltzmann average, 100 empty states (up to about 3 eV above the LUMO) and 2000 transitions were considered. For the T=0 case, only the HOMO-LUMO transition was used for the calculation of the lifetime.

Calculations for the radiative lifetimes were performed using 50 snapshots over the 10 ps trajectory (results obtained with 100 snapshots by decreasing the spacing between snapshots yielded the same average values). The lifetimes are inversely proportional to the rate of radiative carrier recombination and are an important property to characterize optoelectronic devices built from NP solids. We found that for isolated NPs, the radiative lifetime of the transition between the highest occupied and lowest unoccupied molecular orbitals (HOMO and LUMO, respectively) decreases by about two orders of magnitude from 0 K to 250 K, as can be seen in blue in Fig. 4.3b. This is due to symmetry breaking at finite T: the high symmetry of the optimized structure at T=0 leads to degenerate, nearly forbidden transitions that become allowed when the symmetry is broken due to thermal motion. When analyzing the single particle wave functions we found that at 0 K both the HOMO and LUMO are delocalized over the NP; at finite temperature the LUMO remains delocalized but the HOMO localizes in different regions of the NP over the course of the simulation, leading to an increase of the transition dipole moment and thus to a decrease of the radiative lifetime. The trend in the lifetimes observed here is similar to that reported in the experiments by Maikov *et al.* [112] for PbSe NPs of comparable size, and highlights the importance of including

finite-temperature effects in predictive models of NPs.

4.3.3 Analysis of and Comparison to Nanoparticle Dipole Moments in the Literature

Following our electronic structure calculations, we characterized the dielectric properties of the NPs at different temperatures, which have been widely disputed in the literature and are of great importance to understand assembly of NPs into solids. The magnitude of the dipole for lead (and cadmium) chalcogenide NPs in particular is highly controversial in the literature, i.e. with Klokkenburg *et al.* [91], Sashchiuk *et al.* [146], and Bertolotti *et al.* [20] reporting dipole moments between 300 and 600 D for NPs above 2.5 nm in diameter, and other groups [155, 22, 168] reporting values between 0 - 150 D for the same sized systems using different experimental techniques and analytical expressions.

At T=0, we found a non-zero dipole moment (0.98 D) for the isolated $Pb_{32}S_{28}I_8$ NP, due to the asymmetric ligand arrangement on the surface. As a function of temperature, the dipole moment increased to 4.16 ± 1.9 D at 250 K and 5.68 ± 3.0 D at 510 K. Importantly, we observed that the dipole moment fluctuates on the order of 10 D with a maximum magnitude of 16 D at 510 K, as shown in Fig. 4.4. The increase in magnitude and the fluctuations are due to structural distortions at finite temperature, which increase with increasing temperature, as well as to ligand migration at the NP surface, for example from one facet to another. We also calculated the dipole moment of $Pb_{62}S_{55}I_{14}$. We found that the fluctuations of the dipole moment are similar to those found for the smaller NP. In particular, the dipole moments of $Pb_{62}S_{55}I_{14}$ and $Pb_{32}S_{28}I_8$ averaged over 8 ps are 4.18 ± 1.6 D and 6.06 ± 3.2 D, respectively (without including the corrections for the induced electric field described in Section 4.2); the maximum dipole moment calculated for $Pb_{62}S_{55}I_{14}$ was 9.0 D, with a minimum value of 1.0 D, compared to 17.0 and 1.0 D for the maximum and minimum calculated values for $Pb_{32}S_{28}I_8$.

Fig. 4.5 shows our calculated dipole moment of $Pb_{32}S_{28}I_8$ compared to the values of
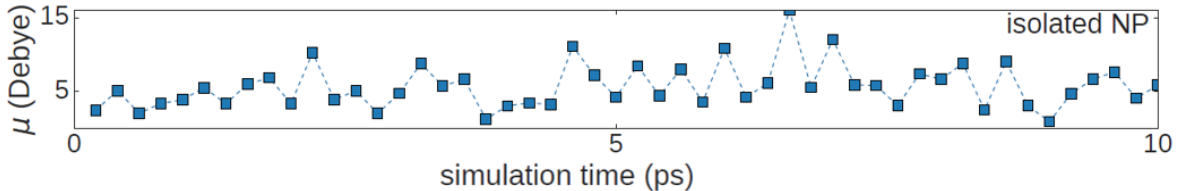
Figure 4.4: Instantaneous dipole moment (μ) as a function of time for an isolated $Pb_{32}S_{28}I_8$ NP over a 10 ps trajectory at T=510 K

dipole moments of lead chalcogenide (squares), cadmium chalcogenide (circles), and zinc chalcogenide (triangles) NPs with radius between 7 and 50 Å, as reported in various papers in the literature. The dipole moment has been measured using a variety of methods, including transient electric birefringence measurements [109], Stark Effect [153, 40, 41, 24], impedance measurements [155, 22], and pair-interaction calculations [91]. Using the birefringence method, a change in index of refraction (used to then calculate a dipole moment) is measured as elongated particles such as nanorods rotate to align in response to an applied pulsed electric field. Alternatively, using the Stark Effect one measures the change in optical density of a sample as an electric field is applied, and the derivative of the optical density is used to extract the dipole moment of the excited state. Impedance measurements on NPs are the most direct method to obtain dipole moments, where the complex impedance of a parallel plate capacitor is measured to obtain the complex dielectric constant of colloidal NPs positioned in between the two parallel plates; the dipole moments are then obtained from the Debye-Onsager equation relating the complex dielectric constant to the dipole moment of a dilute concentration of spherical dipoles [79]. Finally, the so-called pair-interaction method analyzes transmission electron micrographs of dipolar NP chains using a 1D aggregation model in which the concentration of dipolar chains and the chain lengths are used to calculate the potential of mean force between nanoparticles, and from that (assuming a dipolar interaction) the dipole moment. Dipole moments obtained using the Stark Effect method were excluded from Fig. 4.5 as the Stark Effect measures the change in the dipole

moment of excited states as a static electric field is applied, and this quantity is not the same as the ground state dipole we calculated. Furthermore, we limited our study to the dipole moments of spherical or cubical NPs, where it was straightforward to define a "radius," and we do not report birefringence results in Fig. 4.5 as this method requires systems with high aspect ratios such as nanorods.
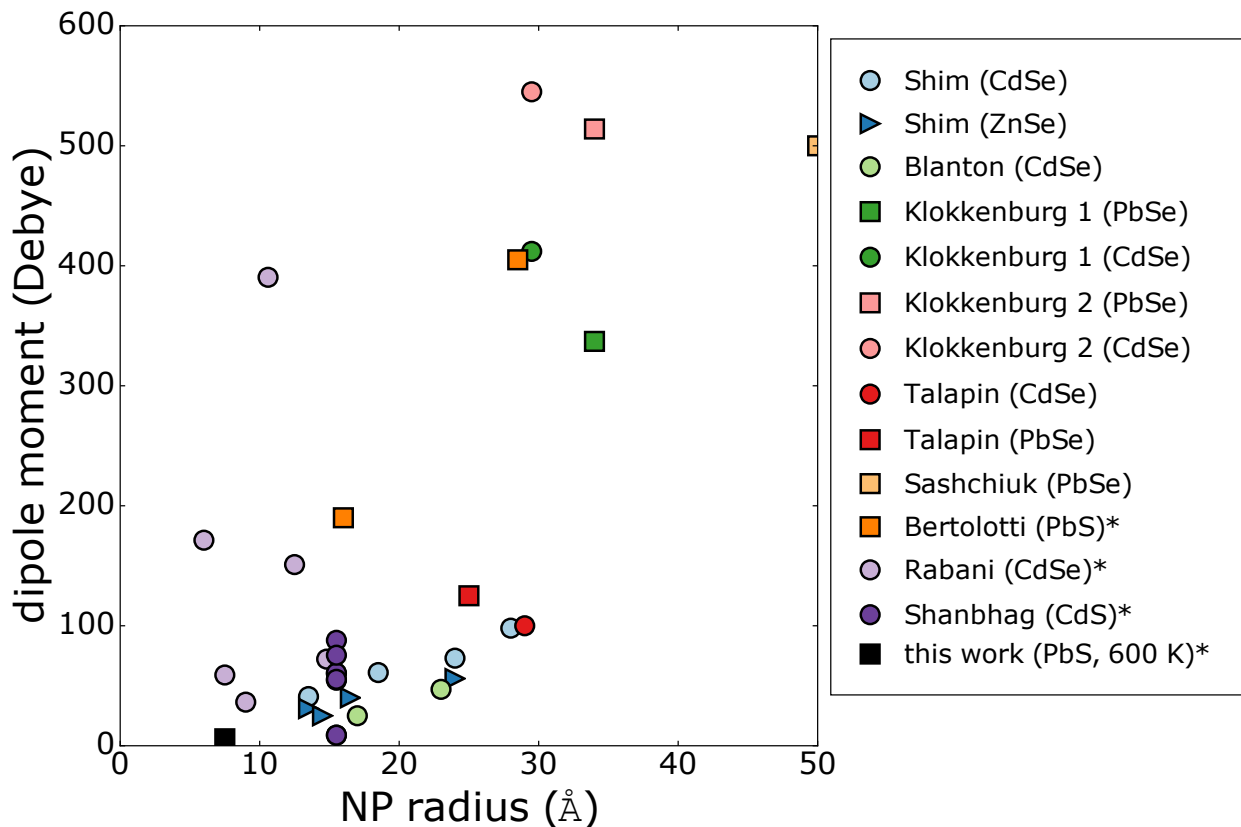
Figure 4.5: Dipole moment data collected from the literature to show the range of values that have been reported. [155, 22, 91, 168, 146, 20, 139, 154] In the legend, an asterisk indicates computational results. "Klokkenburg 1" [91] uses the point-charge assumption, while "Klokkenburg 2" uses the point-dipole assumption for the calculation of the dipole.

Although some [155, 22] reports claim to observe trends in the dipole moment as a function of size, overall we did not observe a clear correlation between the NP radius and the magnitude of the dipole moment from Fig. 4.5. Besides, as our calculations show, any residual interactions that may occur between NPs would affect the value of the dipole moment, making the interpretation of experimental data difficult. We conclude that the

dipole moment of NPs is sensitive to changes in interactions (even non-bonding interactions), ligands, and temperature fluctuations, thus small changes in synthesis conditions or NP concentration could potentially lead to substantial changes in the dipole moment magnitude.
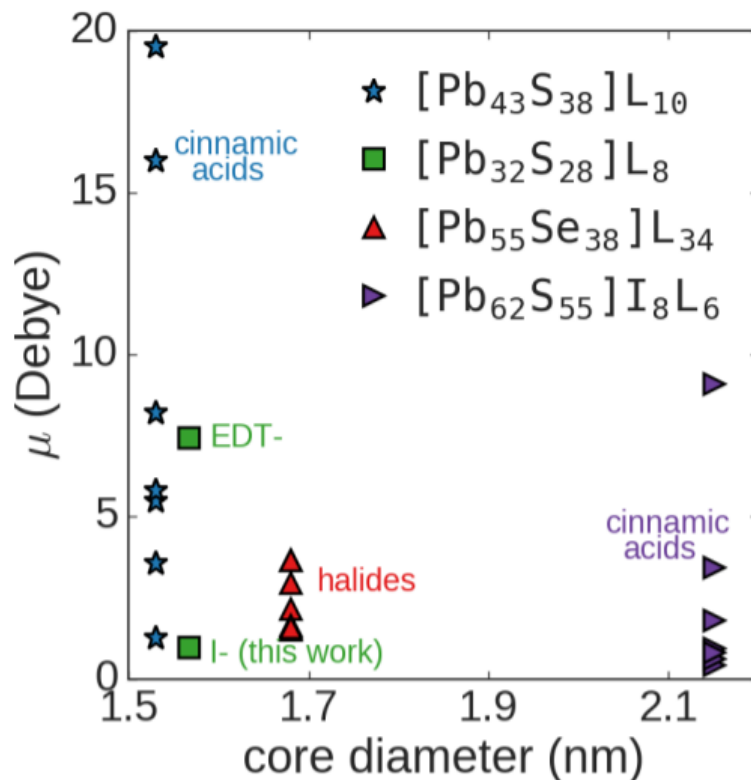
Figure 4.6: Computed dipole moments at T=0 for the lead selenide and lead sulfide NPs with a variety of ligands (L=halides (F,Cl,Br,I), ethane dithiol (EDT), and cinnamic acids)

We further note that the comparison between the different values of dipole moments reported in the literature is not straightforward, as experiments used different ligands as well as NP shape. To shed light on this effect, we calculated the dipole moment for a number of PbS and PbSe NPs at 0 K with different ligands, including replacement of the iodine on $Pb_{32}S_{28}I_8$ with ethane dithiol (EDT), and halide ligands (F, Cl, Br and I) and we considered NP cores ranging from 1.5 - 2.1 nm. We also computed the dipole moments of NPs previously investigated by Kroupa *et al.* [98], capped with cinnamic acid ligands. Our results are reported in Fig. 4.6. We found that the magnitude of the dipole can be tuned by ligand choice for a given NP core, an observation consistent with the claims of Rabani [139]

and Shanbhag [154] that the dipole moment of a NP does not necessarily increase linearly as a function of NP size. In our calculations, we did not observe that the longest ligands (cinnamic acids) always provided the largest dipole. However, we did find that the choice of ligand can have a significant effect on the magnitude of the dipole, despite the ligands being often ignored in the literature. We caution that it may be necessary to revisit some of the approximations made to fit and interpret experimental data, as NP structure, ligand selection, and interactions between tightly packed NPs all contribute to the value of the dipole moment, with even residual interactions between NPs playing an important role in the interpretation of experimental data.

Finally, to relate directly to properties of the nanoparticle solids, we computed the electronic polarizability, α of the isolated NP using finite differences of the polarization under application of an electric field, with the polarizability tensor defined as:

$$\alpha_{ij} = \Omega \frac{P_i(+\Delta E_j) - P_i(-\Delta E_j)}{2\Delta E_j} \tag{4.3}$$

where $P_i(\Delta E_j)$ denotes the polarization in the ith direction in response to an applied field ΔE_j in the jth direction. The ionic coordinates were not allowed to relax upon application of the applied field.

As shown in blue in Fig. 4.7, for the isolated NP we found a surprisingly constant, nearly temperature-independent polarizability of 398 ± 3 Å^3 at 250 K and 401.5 ± 2.5 Å^3 at 510 K, where we defined α to be the trace of the polarizability tensor. In contrast to the dipole moments, the fluctuations in the polarizability were small.

4.4   Nanoparticle Solids

4.4.1   Optoelectronic Properties of Interacting Nanoparticles

Our analysis of the optoelectronic properties of finite temperature isolated NPs was carried out so that the effect of interactions between NPs could be fully understood. Fig.   4.3a
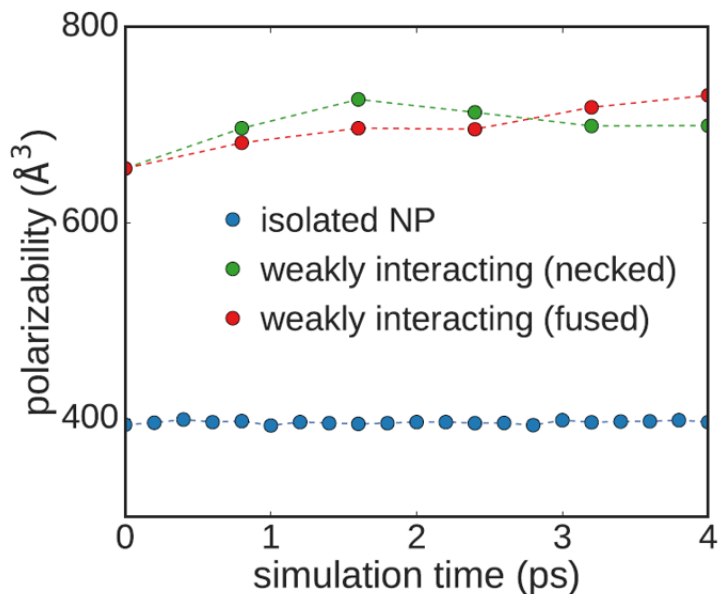
Figure 4.7: Computed polarizabilities as a function of simulation time at T=510 K for the dilute (isolated NP) and weakly interacting solids of $Pb_{32}S_{28}I_8$ NPs (see text)

shows the calculated band gap (E_g) of the two solid structures compared to the isolated NP. We found that the band gap decreases with a similar slope as a function of temperature for all three systems. When the NPs interact to form a solid, the band gap slightly decreases by up to approximately 0.2 eV.

For the isolated NPs, we showed in Section 4.3.2 that the radiative lifetime of the transition between the highest occupied and lowest unoccupied molecular orbitals (HOMO and LUMO, respectively) decreases by about two orders of magnitude from 0 K to 250 K due to the breaking of symmetry at finite T. We observed similar decreases in lifetimes for the NP solids (green and red dotted lines in Fig. 4.3b) at finite T, though to a lesser extent, with the lifetimes about 5 times smaller than at T=0. The calculated radiative lifetimes were $\tau_{510K}/\tau_0 = 0.19$ and $\tau_{510K}/\tau_0 = 0.52$ for the fused and necked solid, respectively. The trend in the lifetimes observed here is similar to that reported in the experiments by Maikov et $al.$ [112] for PbSe NPs of comparable size, and highlights the importance of including finite-temperature effects in predictive models of NPs.

In addition to a decrease of electronic gaps and lifetimes, in the case of the NP solids, we found that instantaneous structural distortions at finite temperature lead to the emergence of localized occupied orbitals within the gap. In Fig. 4.8a we plot the near-gap energy levels as a function of time for a short (0.2 ps) portion of the 510 K simulation for the fused solid, during which one can observe the periodic emergence of an occupied gap state, shown in red in Fig. 4.8a. We found a similar electronic structure for the necked solid at 510 K. At 250 K, such a state was still present, although positioned closer to the valence band maximum (VBM) and it did not occur as frequently throughout the simulations. On average, these dynamic gap states occurred on a timescale of approximately 50 fs during the entire simulation, and they were localized at times on the NP core and at times on the ligands (wave functions are shown in the inset of Fig. 4.8a). This emergent gap state may contribute to the decrease of E_g at finite T, although to a small extent: over a 10 ps portion of the trajectory, we found that the intra-gap state is on average only 0.1 eV above the state immediately lower in energy. It is expected that localized states could give rise to trapping [6, 27], thus we speculate that these emergent localized occupied states may be detrimental to hole transport in NP films. We have not observed any localized unoccupied states, indicating the electron transport may not be affected by trap states.

4.4.2 Emerging Dipole Moments in Nanoparticle Solids

To shed light on the sensitivity of the dipole moment to the interactions between NPs, we compared the dipole moment computed for the isolated $Pb_{32}S_{28}I_8$ NP at 0, 250, and 510 K to those of the weakly interacting solids (See Section 3.4 for details on dipole moment calculations). At T=0, we found a non-zero dipole moment (0.98 D) for the isolated NP, due to the asymmetric ligand arrangement on the surface. As a function of temperature, the dipole moment increased to 4.16 ± 1.9 D at 250 K and 5.68 ± 3.0 D at 510 K. Importantly, we observed that the dipole moment fluctuates on the order of 10 D with a maximum magnitude of 16 D at 510 K, as shown in Fig. 4.9b. The increase in magnitude and

a)

b)
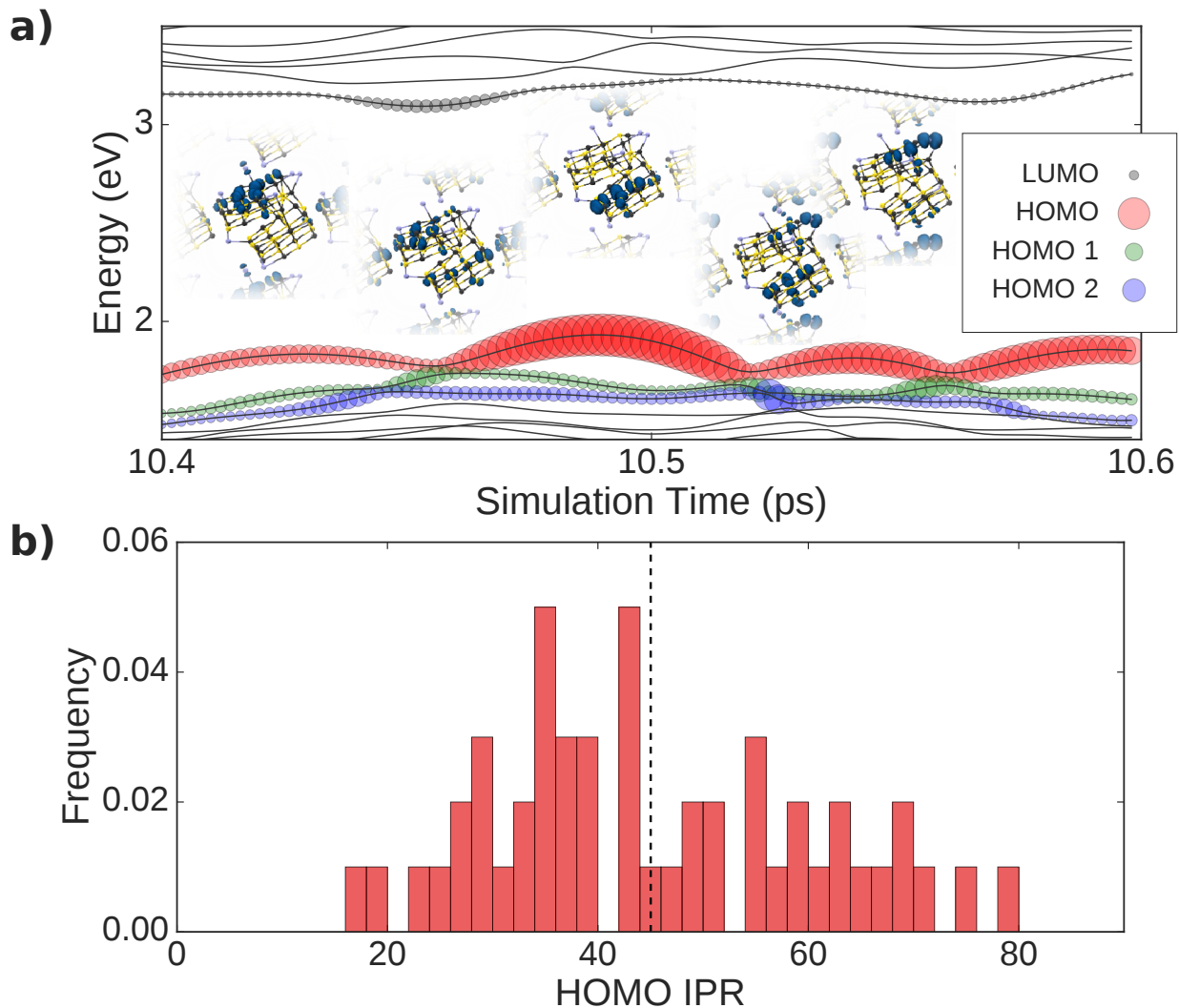
Figure 4.8: a) Emergence of intra-gap states (red dots, corresponding to the highest occupied level (HOMO)) during a small (0.2 ps) portion of the 510 K simulation for the fused solid. The size of dots indicates the value of the inverse participation ratio (IPR, defined as: $\frac{\int |\psi_i|^4 d^3 r}{\left(\int |\psi_i|^2 d^3 r \right)^2}$; larger IPR indicated more localized wave functions). Ball and stick representations of the NP structures show where the HOMO is localized at specific snapshots (from left to right, corresponding to #16, 29, 47, 61, and 72 of the 100 snapshots spaced evenly over the 0.2 ps window). b) Distribution of IPR for the HOMO wave function (intra-gap state) over a 10 ps simulation for the fused solid. Dotted line represents the average value.

the fluctuations are due to structural distortions at finite temperature, which increase with increasing temperature, as well as to ligand migration at the NP surface, for example from one facet to another. We also calculated the dipole moment of $Pb_{62}S_{55}I_{14}$. We found that

50

the fluctuations of the dipole moment are similar to those found for the smaller NP, and that the band gaps and lifetimes follow the same trends. In particular, the dipole moments of $Pb_{62}S_{55}I_{14}$ and $Pb_{32}S_{28}I_8$ averaged over 8 ps are 4.18 ± 1.6 D and 6.06 ± 3.2 D, respectively; the maximum dipole moment calculated for $Pb_{62}S_{55}I_{14}$ was 9.0 D, with a minimum value of 1.0 D, compared to 17.0 and 1.0 D for the maximum and minimum calculated values for $Pb_{32}S_{28}I_8$.

For the necked and fused solids, the absolute dipole moment is ill-defined as these systems are periodic. Hence analysis of the dipole moments was limited to the weakly interacting systems (Fig. 4.9c). We found that weak interactions lead to an increase in the dipole moment even in the absence of bond formation between neighboring NPs. Here, the dipole fluctuations were again significant, with values up to 77.5 D and as low as 5 D at 510 K.
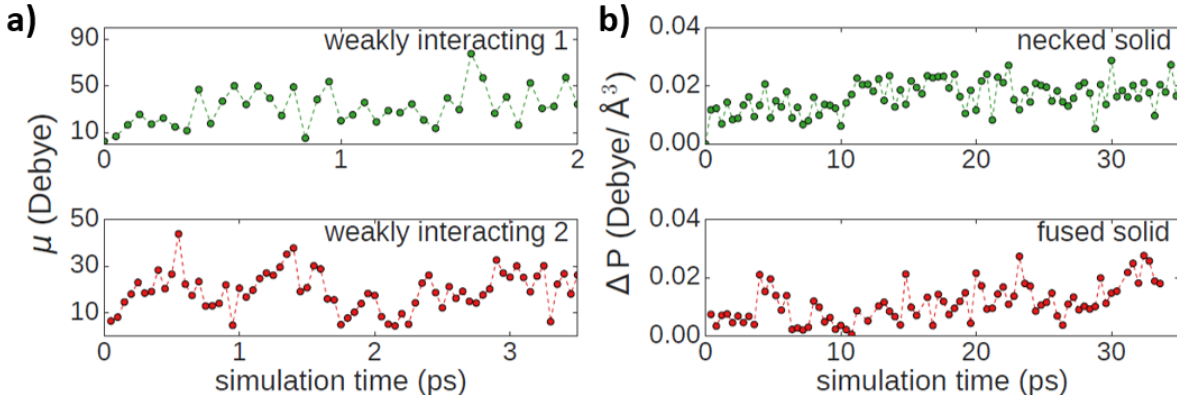
Figure 4.9: a) Instantaneous dipole moment (μ) as a function of time for the weakly interacting NPs over two short trajectories of 2 and 3 ps at T=510 K. b) Difference in polarization with respect to the origin of the trajectories for two interacting NP solids (necked and fused; see text) at T=510 K

For the necked and fused solids, in Fig. 4.9d we plot the difference in polarization, with respect to the initial configurations where bonds were not yet present, as a function of time, showing again a fluctuating behavior. These results indicate that for all solid structures studied here, the NP building blocks acted as dynamic, fluctuating dipolar systems rather than static point-dipoles.

In contrast to the dipole moments, the fluctuations in the polarizability were small,
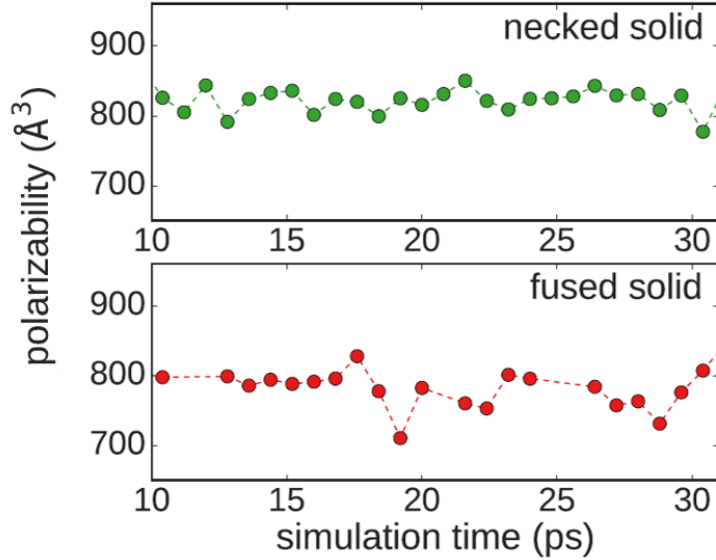
Figure 4.10: Computed polarizabilities as a function of simulation time at T=510 K for the necked and fused solids of $Pb_{32}S_{28}I_8$ NPs (see text)

however increasing in magnitude with the interaction strength. While the increase in α from 700 to 800 Å^3 seem in Fig. 4.9 between the weakly interacting systems and the solids is in part due to the increased number of bonds upon formation of the solid, the increase from 400 to 700 Å^3 from the isolated NP to the weakly interacting solid corresponds solely to non-bonding interactions. These results indicate that it may not be sufficient to use a fixed polarizability value (such as the polarizability of bulk PbS) for models of self-assembly of PbS NP solids, as the electronic part varies substantially. Furthermore, we compared our computed polarizabilities with that calculated from the commonly-used Clausius-Mossotti relation:

$$\alpha_{CM} = \frac{3\Omega}{4\pi} \frac{(\epsilon_\infty - 1)}{(\epsilon_\infty + 2)} \tag{4.4}$$

where the dielectric constant of the solid, ϵ_∞, was obtained by applying a finite electric field to the NP solids and using the Qbox code. We found a value of approximately 3.2 at 0 K for the weakly interacting solid (increasing to 3.6 and 3.7 at 510 K for the fused and necked solids, respectively, which is much smaller than the PbS bulk dielectric constant of

22). We found that the Clausius-Mossotti relation underestimated the polarizability of the interacting solids by 60%, providing values of only 376 Å^3 instead of 700 Å^3, due to inherent approximations of a homogeneous non-dipolar material underlying the derivation of Eq. 4.4.

4.5 Conclusions

In conclusion, we investigated the combined effect of temperature and NP-NP interaction on functionalized PbS nanoparticles, showing the emergence of electronic and dielectric properties different from those of isolated NPs. Using first principles molecular dynamics and electronic structure calculations, we showed that the fundamental gap of the NP slightly decreases with T and as a function of interaction strength, while the radiative lifetimes exhibited a much stronger dependence on interaction, becoming an order of magnitude less sensitive to temperature compared to those of isolated NPs. Our calculations also showed that weakly interacting NPs behave as fluctuating dipoles, with amplitudes on the order of 300% with respect to the average dipole moment, similar to those that we observed for the polarization of strongly interacting NP solids. We found that electronic polarizabilities, similar to dipoles, are affected by the interaction between NPs, increasing by about a factor of 2 in strongly interacting solids; however, their fluctuations at finite T are much smaller than those of the polarization. Hence, at finite T the NP solids behave as dynamical, polarizable dipolar systems, and dispersion interactions, e.g. as Casimir forces, are expected to contribute to their bonding and stability. Finally, in view of our findings, we revisited and discussed several results present in the literature for the dipole moments of lead chalcogenide NPs terminated with various ligands.

CHAPTER 5

ELECTRONIC AND OPTICAL PROPERTIES OF QUASI-2D NANOPLATELETS

5.1   Introduction

In the previous chapter, we discussed the collective properties of lead sulfide nanoparticles as part of a solid composed of these "building blocks", in particular investigating the combined effects of interactions between nanoparticles and the disorder introduced through finite temperature distortions. Here, we transition to studying cadmium selenide nanoplatelets, a class of nanomaterials that is less understood from both an experimental and computational perspective, but has the potential to outperform nanoparticles for photovoltaic applications due to finer tunability. Thus, before understanding the collective behavior of a solid composed of these nano-objects, it is essential to first understand the properties of the isolated nanoplatelets. In this chapter, we describe a computational protocol to accurately calculate the optoelectronic properties of quasi-2D nanoplatelets, in particular focusing on the optical band gap and related quantities for solar cell device performance. We provide state-of-the-art calculations of the optical gap, and interpret our results using a series of simple models that allow us to disentangle the effects of quantum confinement, strain, and dielectric contrast between the material and its environment. In Section 5.2, we begin by laying out our computational strategy, including details of the electronic structure methods and structural models. In Section 5.3, we continue with a deeper discussion of the structural properties of nanoplatelets, particularly in relation to their unique biaxial strain profiles. In Section 5.4, we present and then interpret calculations of the fundamental band gap of these materials obtained using G_0W_0, and suggest a new model that can be used to estimate the fundamental gap of NPLs with reduced computational cost, relative to many body perturbation theory calculations. We end the section with a discussion on the challenges of defining an effective dielectric constant for quasi-2D materials, providing our own definition of a quasi-2D effec-

tive dielectric constant and commenting on the validity of our method through comparing hybrid functional calculations to G_0W_0. Finally, in Section 5.5.1 we use our results for the electronic structure of nanoplatelets to calculate and interpret the optical properties that can be directly related to experiment. We show agreement with experimental optical band gaps and absorption spectra, and provide the first calculations of the exciton binding energy for these materials that do not use excitonic models.

5.1.1 State of the Art of Calculations and Experiments for Semiconducting Nanoplatelets

Quasi-two dimensional CdSe nanoplatelets (NPLs) are a remarkable class of anisotropic materials with strong quantum confinement in only one direction much like epitaxially-grown quantum wells. Similarly to quantum dots (QDs), which have been successfully integrated into certified solar cells, the highly controlled tunability of the optical absorption spectra of NPLs as a function of their thickness promises successful integration of these materials as photoabsorbers in photovoltaic devices. Due to recent synthetic advances, the size and structure of NPLs can be controlled with atomic precision, leading to impressively narrow absorption and emission linewidths of less than 40 meV, nearly half of that typically observed for QDs [34]. This atomically precise synthesis has additionally opened up the possibility to further tune the unique electronic structure of each layer of a complex NPL heterostructure.

Today, CdSe NPLs are routinely synthesized with passivating ligands that have been experimentally shown to affect their photophysical properties [1, 49]. In line with computational reports [176, 195], experiments further suggest [1, 49] that NPLs exhibit ligand-dependent biaxial strain profiles that lead to detailed atomic structures quite different from their bulk counterparts. However, the relationship between ligands, atomic structure, and photophysical properties is not fully understood. This is due, in part, to discrepancies between different computational methods adopted to model the properties of NPLs for example, the optical transition energies.

In general, the optical transition energy is given by the difference between the quasi-particle (QP) and exciton binding (E_b) energies. The former is the difference between the ionization potential and electron affinity. The latter describes the attractive interaction between electron and hole, and it may be modeled knowing the dielectric constant and effective mass of the material. While optical transitions are measured using i.e. UV-vis spectroscopy, separately measuring the quasiparticle and exciton binding energies is more challenging particularly for colloidal solutions where typical photoemission spectroscopy measurements suffer from scattering due to the solvent. For colloidal NPLs, measurements of the QP energies have only recently become accessible [188], through an experimental procedure combining absorption and photoacoustic spectroscopies [188]. Due to the lack of data on QP and exciton binding energies, previous theoretical efforts have used optical transition energies only to validate models of electronic properties. Various theoretical investigations have used different methods to compute E_b and QP energies [37, 17], with reported results that differ significantly, especially for the QP energies.

The common methods for computing quasiparticle energies can be broadly classified in order of increasing computational cost as: effective-mass approximation (EMA), tight-binding (TB), Density Functional Theory (DFT), and the GW approximation. Increased computational cost comes at the benefit of a reduced number of model assumptions. Discrepancies in predicted quasiparticle gaps between different methods can originate from both differences in model assumptions and choice of parameters. Parametric discrepancies between different computational approaches are easier to reconcile. However, identifying differences in model assumptions has more profound implications on our physical understanding of NPLs.

Here, we present a computational protocol for studying quasi-2D NPLs based on first-principles calculations and on the assessment of a number of models that have been proposed in the literature [11, 83, 150, 37, 132] for estimating the quasiparticle gaps and exciton binding energies. In doing so, we rationalize how the photophysical properties of NPLs are affected by ligand-induced biaxial strain and quantum confinement as well as dielectric contrast

between the NPL and its environment. Specifically, we use Density Functional Theory (DFT) calculations to probe the structural properties of a series of CdSe NPLs. Quasiparticle (QP) and exciton binding (E_b) energies are directly computed using Many Body Perturbation Theory at the G_0W_0 level and the Bethe Salpeter equation (BSE), respectively. Our G_0W_0 and BSE results compare favorably with recent experimental reports [188] and are to the best of our knowledge the first calculations at this level of theory for NPLs. We interpret our G_0W_0 results for the QP energy using an EMA model and find agreement between our calculations and the model only when quantum confinement effects are included using a finite, and not infinite, potential barrier in the EMA model—the infinite one being most commonly assumed barrier in literature. We show how the QP energies of NPLs are sensitive to the interplay between dielectric contrast, which has been the focus of previous reports [37, 17], and biaxial strain as well as quantum confinement. Further, we devise a model accounting for strain effects,quantum confinement and dielectric contrast that provides a simple way to estimate the fundamental gap of complex NPLs when the use of first-principles methods is not feasible due to the high computational cost.

To compare our BSE calculations of the exciton binding energies of NPLs with available excitonic models, we calculate the effective masses of each NPL as well as an effective dielectric constant defined using information from the electrostatic potential, illustrating the importance of taking into account the thickness-dependent nature of all quantities entering the excitonic model. The interpretation of our BSE results through exciton models further highlights the necessity to consider the effect of the screened Coulomb interaction due to dielectric contrast between the NPL and its environment, as well as a finite extension of the exciton wavefunction in the direction perpendicular to the NPL.

5.2   Computational Framework

In line with previous experimental and computational reports [83, 36, 17, 164, 195], we focus our study on zinc blende CdSe NPLs ranging from 2-7 monolayers (MLs) in thickness, where

we define the number of monolayers to be equal to the number of layers of Se, adhering to the formula $Cd_{x+1}Se_x$ due to the symmetric Cd termination on both the top and bottom of the NPL. We chose NPLs capped with chlorine ligands to passivate both surfaces, as they have been successfully used in ligand-exchange experiments [36], with ligands initially placed as bridges between Cd atoms prior to structural relaxation [164] to preserve the tetrahedral coordination.

Structures of 2ML, 3ML, 5ML and 7ML NPLs were generated using 2x2x1 supercells (28-68 atoms) and using 3x3x1 k-point meshes, allowing both the in-plane lattice constants and the atom positions to relax until forces were below 10^{-5} a.u. We found that the relaxation of lattice constants in addition to atomic positions was essential in order to recover accurate strain profiles. All structural relaxations were performed using the open source plane-wave code Quantum Espresso [61] with the Perdew-Burke-Ernzerhof (PBE) exchange-correlation functional [134] and using PseudoDojo pseudopotentials [173] to describe the interaction between the core and valence electrons; we found that including the 3d electrons in the valence partition of Se was essential to reproduce a band gap in quantitative agreement with experiment (see further details in Section 3.2.4). A kinetic energy cutoff of 100 Ry was used for all calculations, with a vacuum spacing of at least 17 Angstrom in the out-of-plane direction to separate periodic replicas.

5.2.1   Calculation of Quasiparticle Gaps from G_0W_0

G_0W_0 quasiparticle energies were calculated for the 2ML, 3ML and 5ML NPLs, while BSE calculations were performed on 2ML and 3ML NPLs only. For both G_0W_0 and BSE calculations, a primitive unit cell of 7-15 atoms was used. Each primitive unit cell was symmetrized to remove spurious numerical differences in the lattice constants in x and y and reduce the number of k-points needed to carry out our calculations, with a difference in band gap compared to the non-symmetrized structure of less than 0.1 meV.

G_0W_0 calculations were performed using the West code [66], which does not require
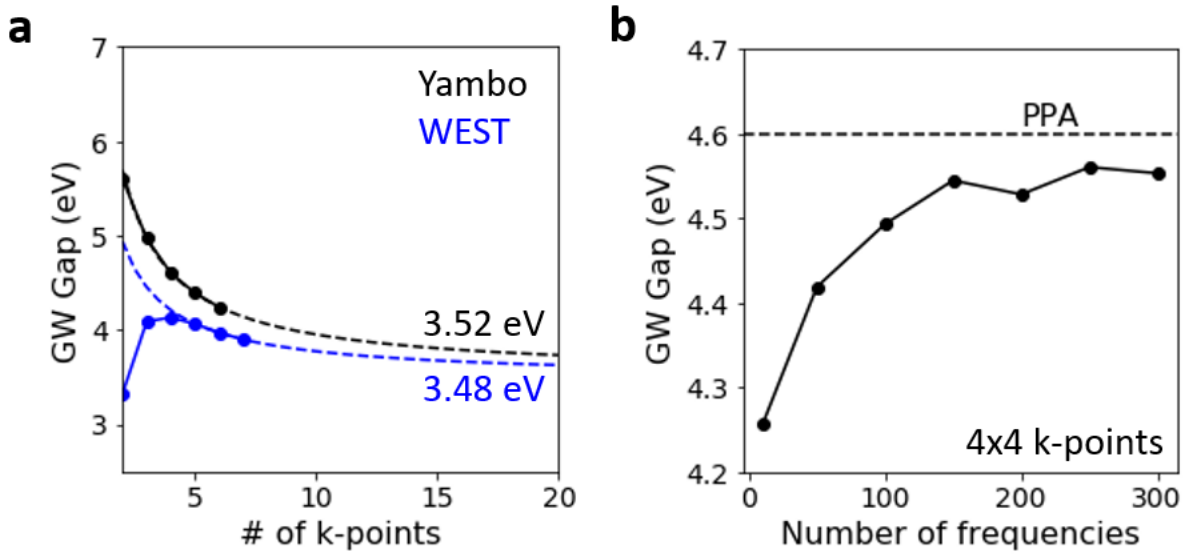
Figure 5.1: a) Comparison of the convergence of the G_0W_0 band gap with respect to k-point mesh for a 2ML CdSe NPL, obtained using Yambo (Plasmon-pole model approximation) and West (Full-frequency integration), demonstrating that the two codes agree after extrapolating to infinite k-points, but not for small k-point meshes, due to different methods adopted for the truncation of the Coulomb potential. The x axis gives number of k-points in the in-plane direction, i.e. 4x4x1, etc. b) Comparison of Plasmon-pole approximation to Full-frequency approaches using Yambo with a 4x4x1 k-point mesh for the 2ML NPL, as a function of increasing number of explicitly calculated frequencies.

explicit calculation of empty states and avoids inversion of dielectric matrices. G_0W_0 quasi-particle gaps were extrapolated to infinite number of k-points in the lateral dimensions and to infinite number of PDEPs (see Section 3.5 for discussion of PDEP convergence). The long-range Coulomb interaction was truncated to properly converge with respect to vacuum size in the axial direction, using the method discussed in Ref. [159]. For G_0W_0 calculations in West, we found that a sufficiently large k-point mesh of at least 5x5x1 was essential prior to extrapolation to infinite k-points due to the method used in the code for the Coulomb truncation.

For the 2ML NPL, in Fig. 5.1a we provide a detailed comparison between G_0W_0 calculations using West and the Yambo code [145, 115], the latter of which uses the Plasmon-Pole Approximation (PPA) of Godby and Needs [63, 53, 161] rather than the full-frequency (FF) approach of West. Yambo calculations of the quasiparticle gap were conducted with 100 empty states, and the Coulomb interaction was truncated using the Random Integration Method (RIM) [123]. We found that, after extrapolating to infinite k-point meshes, quasiparticle gaps calculated with the two codes converge to within 40 meV (Fig 5.1a), with the remaining small discrepancy accounted for by the difference between PPA and FF approaches (Fig 5.1b, where both PPA and FF are calculated with Yambo).

5.2.2 Calculation of Exciton Binding Energy from BSE

The exciton binding energy and absorption spectra of CdSe NPLs were calculated through the Bethe-Salpeter Equation (BSE) using the Yambo code (see Section 3.6 for more details of the method) and using PBE wavefunctions and a scissor correction equal to the difference between the G_0W_0 and PBE gaps at the chosen k-point density for the 2ML and 3ML NPLs. The final spectrum for the 2ML NPL was calculated with a 15x15x1 k-point mesh, while exciton binding energies for the larger NPLs were extrapolated from smaller k-point densities, as shown in Fig. 5.2b and c. We found that convergence with respect to k-point mesh was essential, as the BSE spectra required a much denser mesh than the PBE or
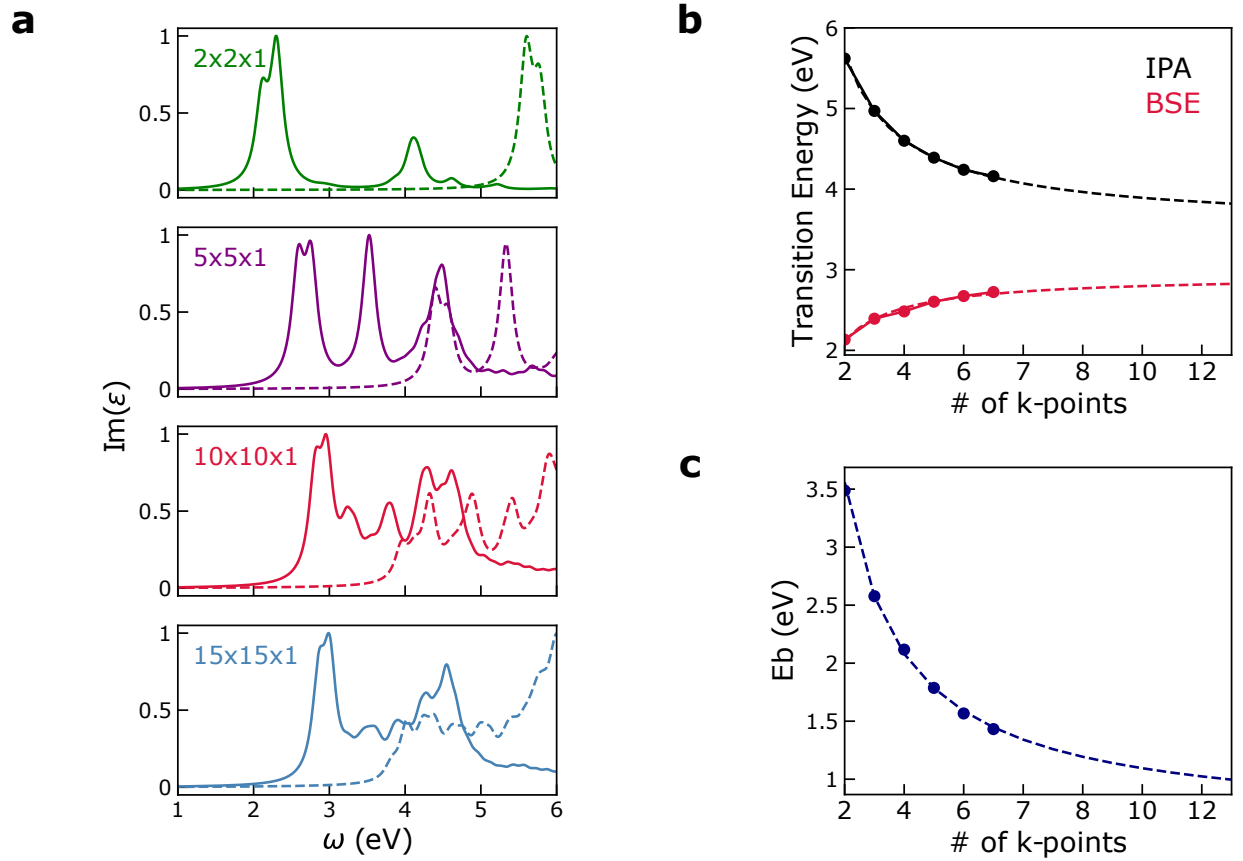
Figure 5.2: a) Examples of BSE spectra obtained at different k-point densities, from 2x2x1 to 15x15x1, for a 2ML CdSe NPL. Solid lines are from BSE, while dashed lines are from the Independent Particle Approximation (IPA). Spectra are plotted with a Lorentzian broadening of 0.1 eV. b) Convergence as a function of k-points of the first transition energy for the IPA spectrum (black, same as HOMO-LUMO G_0W_0 gap) and BSE (red). c) Convergence as a function of k-points of the exciton binding energy of the 2ML NPL, calculated as the difference between the first transition energies of IPA and BSE.
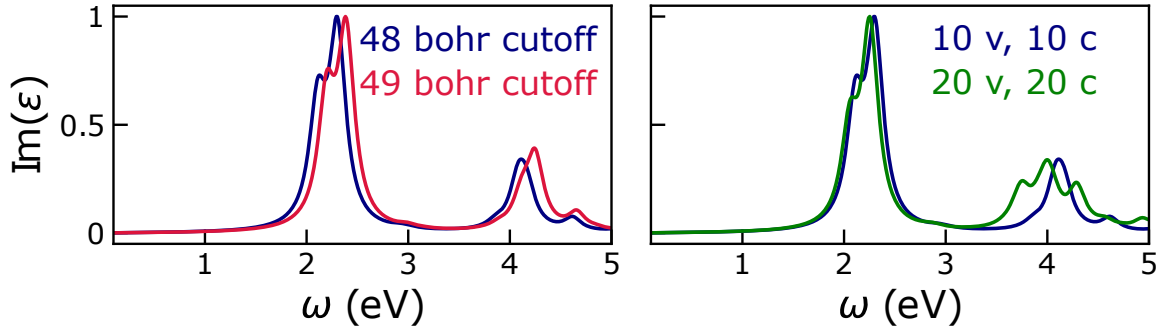
Figure 5.3: (left) 2x2x1 k-point BSE spectrum for 2ML CdSe using a Coulomb cutoff set at 48 (blue) and 49 (red) Bohr. Total axial unit cell size is 49.4 Bohr. (right) 2x2x1 k-point BSE spectrum for 2ML CdSe illustrating the difference between including 10 valence/10 conduction band states (blue) and 20 valence/20 conduction band states (green). v=valence band, c=conduction band.

G_0W_0 band gaps alone. In 5.2a we show the variation of the BSE (solid lines) and IPA (dashed lines) spectra of 2ML NPL with increasing k-point density, noting the qualitatively incorrect shape below a 10x10x1 mesh. We note that a fully converged spectrum would require at least 25x25x1 k-points; however, the exciton binding energy and near-quantitative comparison with experiment are obtained by 15x15x1 k-points.

Similarly to the Yambo G_0W_0 calculations, BSE calculations of 2D NPLs employed a Coulomb cutoff using the Random Integration Method in order to converge with respect to vacuum size in the axial direction. The Yambo documentation recommends the Coulomb cutoff to be set approximately 1 Bohr smaller than the total unit cell size in the relevant direction. All BSE and G_0W_0 calculations adhered to this guideline, for example using a cutoff distance of 48.5 Bohr for the 2ML NPL, where the total axial unit cell size was 49.4 Bohr. Comparison of absorption spectra (using only 2x2x1 k-point sampling) with a cutoff of 48 Bohr and 49 Bohr is shown in Fig. 5.3a in blue and red, respectively. As can be seen, the absorption spectra is quite insensitive to the cutoff value when it is close to the edge of the unit cell; however, we found the spectra onset to vary substantially when the cutoff was reduced to near the center of the unit cell and lead to non-physical results.

Finally, the spectra presented in this work were calculated using transitions between 10 occupied and 10 unoccupied energy levels near the band edges to reduce the size of the matrices involved in the BSE calculation. We found this to be sufficient for the convergence of the first two absorption peaks (attributed to the light-hole and heavy-hole transitions), though more transitions would be required to fully converge the higher-energy regions of the spectra, as shown in Fig. 5.3.

5.3   Structural Properties

5.3.1   Atomic Structure of Nanoplatelets

We begin our study through an analysis of the strain profiles in a series of CdSe NPLs. In Fig 5.4 we plot the in-plane and out-of-plane strain for NPLs passivated with Cl^- and H^- (the latter taken from Ref. [195] using the same level of theory). We define the strain to be relative to the bulk lattice constant computed at the PBE level of theory. In line with previous reports, our results show that NPLs are subject to compressive biaxial strain that sensitively depends on their thickness and passivating ligands. We note that different passivating ligands lead to different in-plane (ε_x) to out-of-plane (ε_z) strain ratios. We explain the biaxial strain in NPLs as observed in our first principles calculations by using a continuum elastic model that includes surface stress (solid lines in Fig. 5.4), originally proposed for thin metallic films [69, 163]. According to the model, the equilibrium structure of NPLs, i.e. in- and out-of-plane strain, arises from the fine interplay between volume deformation-energy of the bulk crystal (ΔU_{vol}), and surface energy due to surface stress (ΔU_{s}):

$$\Delta \tilde{U} = \frac{\Delta U_{\mathrm{vol}} + \Delta U_{\mathrm{s}}}{A_0} = \left[L^0_{\mathrm{NPL}} Y_\infty \varepsilon^2 + \mathcal{O}(\varepsilon^3) \right] + 2 f_0 (1 + \varepsilon)^2, \tag{5.1}$$

where ε_x is the in-plane strain, $\Delta \tilde{U}$ is the total work per unit area (A_0), L^0_{NPL} is the NPL thickness in the absence of strain, and f_0 is the surface stress. The biaxial-modulus (Y_∞) in the 100-direction is defined for cubic crystals as $C_{11} + C_{12} - 2C_{12}^2/C_{11}$, where C_{ij} are
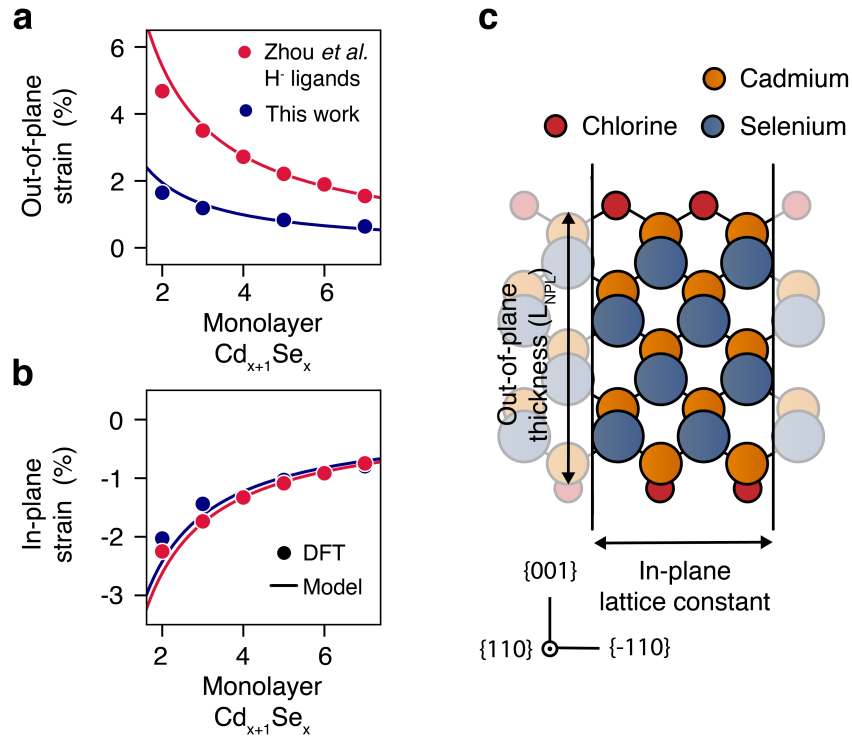
Figure 5.4: a-b) Out-of-plane and in-plane strain as a percentage relative to the bulk lattice constant, for NPLs passivated with Cl^- ligands (blue) and H^- ligands, the latter using PBE data from Zhou, et al [195]. Calculations were carried out at the DFT/PBE level of theory. c) Drawing of a 4ML NPL labelling the in-plane and out-of-plane directions used throughout the text.

the elastic constants of the bulk [92]. The equilibrium in-plane strain that minimizes $\Delta \tilde{U}$ is given as:

$$\varepsilon_x = \frac{-2f_0}{2f_0 + L^0_{\text{NPL}} Y_\infty} + \mathcal{O}(\varepsilon_x). \tag{5.2}$$

Therefore, both in- and out-of-plane strain($\varepsilon_z = -\eta \varepsilon_x$) are inversely proportional to the thickness of the unstrained NPL (L^0_{NPL}). The model also rationalizes the observed overall contraction across all layers of NPL heterostructures grown using c-ALD [77]. Since in biaxially strained materials, a contraction of the in-plane lattice constant leads to an expansion in the axial direction (or vice-versa), changes in the biaxial strain profile of NPLs are coupled with changes in the quantum confinement through changing the NPL thickness. Thus, the electronic properties such as the quasiparticle band gap strongly depend on the amount of strain present in the system.

5.4 Electronic and Dielectric Properties

5.4.1 Fundamental Gaps of Nanoplatelets

To understand the electronic properties of the nanoplatelets, we start by computing the quasiparticle energies of NPLs passivated with Cl$^-$ ligands using G_0W_0 starting from PBE wavefunctions. Results are given in Fig. 5.5 in black. To the best of our knowledge, these are the first calculations of the quasiparticle band gap of CdSe NPLs at the G_0W_0 level of theory, which is widely accepted to give quantitative agreement with experiment.

We find the G_0W_0 quasiparticle gap to be 3.52 eV for the 2ML NPL, decreasing to 3.05 eV for the 3ML NPL and to 2.43 eV for 5ML. We do not include Spin-Orbit Coupling (SOC) for the G_0W_0 calculations, but expect SOC to lower the quasiparticle gaps by approximately 0.1 eV, as was found for bulk CdS GW gaps [148] as well as our own PBE calculations. Our quasiparticle gaps are in good agreement with the only experimental report of fundamental gaps for these materials [188], where they measure the band-to-band transition energy to be approximately 2.9 eV for a 3ML NPL through a combination of photoacoustic and absorption
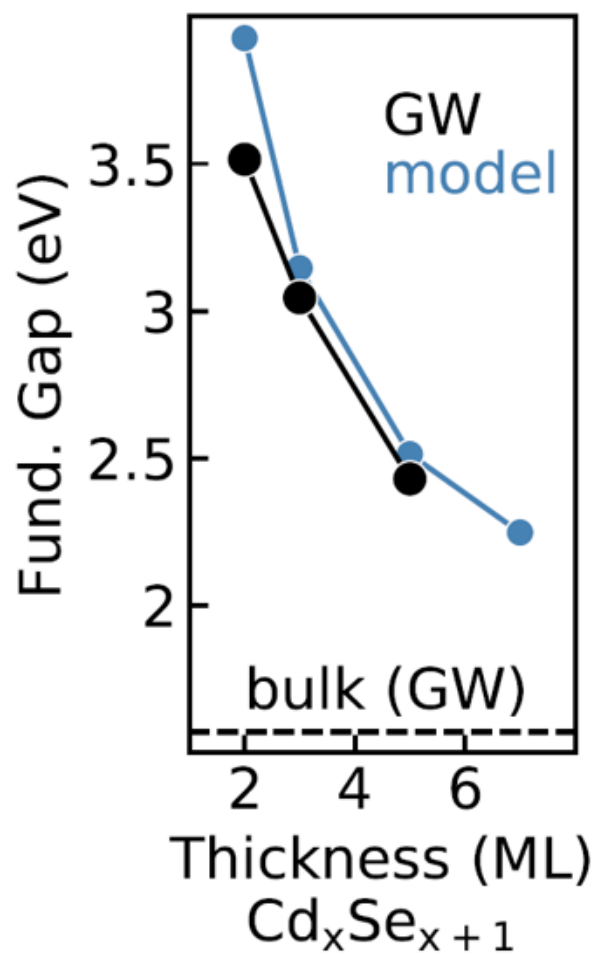
Figure 5.5: Fundamental band gaps of CdSe NPLs calculated using G_0W_0 starting from PBE wavefunctions (black), and estimated using the combined model described in the text (blue).

spectra. However, we note that the experimental samples were capped with organic ligands and were in colloidal solution where the environmental dielectric constant was larger than that of vacuum (approximately 2) which we expect would slightly reduce the measured fundamental gap compared to the one that would be measured in vacuum.

5.4.2   Interpretation of Quasiparticle Gaps Through Simplified Models

While we have presented accurate calculations of quasiparticle gaps, the computational cost of G_0W_0 is prohibitive for thicker NPLs or more complex heterostructures, and thus a model that can estimate the quasiparticle gap with G_0W_0 accuracy, without explicitly performing calculations for each size, is highly desirable. In order to find the best possible model to estimate the quasiparticle band gap of CdSe NPLs, we identified three key descriptors to understand how the properties of NPLs differ from that of bulk CdSe, the latter of which has been extensively studied experimentally, from first principles, and using models. First, as previously mentioned, the strong anisotropy of the NPLs leads to a biaxally strained material whose thickness depends on the exact biaxial strain profile since the in-plane compression directly leads to an axial expansion. Second, similarly to quantum dots or other nanomaterials, quantum confinement, determined by the NPL thickness, leads to an increase of the quasiparticle gap compared to the bulk material. Finally, the quasiparticle gap of a 2D or quasi-2D material has been shown to depend on the dielectric contrast between the material, e.g. the NPL, and its environment [37], and can either increase or decrease depending on whether the external dielectric constant is smaller or larger than the dielectric constant within the material.

We first consider the effect of strain and we begin by discussing an eight-band $\mathbf{k} \cdot \mathbf{p}$-Hamiltonian that accurately describes changes in the band gap of bulk CdSe due to applied biaxial strain; we then compare two separate effective mass models to estimate the change in gap due to quantum confinement. Finally, we will use a model already present in the literature [37] to calculate the change in band gap of the NPL caused by the dielectric

67

contrast due to the surrounding vacuum. Combining the information from the models of the three effects (strain, quantum confinement and dielectric contrast) into a unified model of the QP gap as a function of size, we compare our results with those of G_0W_0 calculations. We obtain an accurate description of the gap as a function of size, comparable to that of G_0W_0 calculations (see Fig. 5.5).

We describe changes in the CdSe bulk band structure, and thus the band gap, as a function of strain using an effective mass $\mathbf{k} \cdot \mathbf{p}$-Hamiltonian [177]. For zinc-blende crystals, such as CdSe, the eight-band $\mathbf{k} \cdot \mathbf{p}$-Hamiltonian describes the energies of the electron, heavy (hh) and light-holes (lh), as well as the spin-orbit (SO) hole bands. At fixed momentum-vector $\mathbf{k}$, the band-energies, and therefore also $E_{\text{QP,bulk}}$, are obtained by diagonalizing the $\mathbf{k} \cdot \mathbf{p}$-Hamiltonian.

The eight-band model can be extended to include effects of strain on the bulk dispersion [11]. To assess changes in band gap as a function of strain, we consider the individual changes in the heavy-hole and electron energies. Changes to the Γ-point energies of the heavy-hole and electron are given by:

$$\Delta E_{\text{e}} = a_p \left(\varepsilon_z - 2\eta \right), \tag{5.3}$$

$$\Delta E_{\text{hh}} = -a \left(\varepsilon_z - 2\eta \right) + b \left(\varepsilon_z + \eta \right), \tag{5.4}$$

where a, b, and a_p are the material-dependent deformation potentials. Out-of-plane (ε_z) and in-plane strain $(\varepsilon_y = \varepsilon_x)$ are connected through $\eta = -\varepsilon_x / \varepsilon_z$. The difference between electron and heavy-hole energy due to strain is then given as:

$$\Delta E_{\text{strain}}^{\text{bulk}} = \Delta E_{\text{e}} - \Delta E_{\text{hh}} \tag{5.5}$$

In Fig. 5.6 we compare the pristine-bulk dispersion obtained from PBE calculations to the results obtained from the eight-band model which has been parametrized using our PBE results. We also plot the bulk Γ-point energies of both heavy-hole and electron, computed for different out-of-plane strains. The deformation potentials $(a, b, \text{ and } a_p)$ were determined
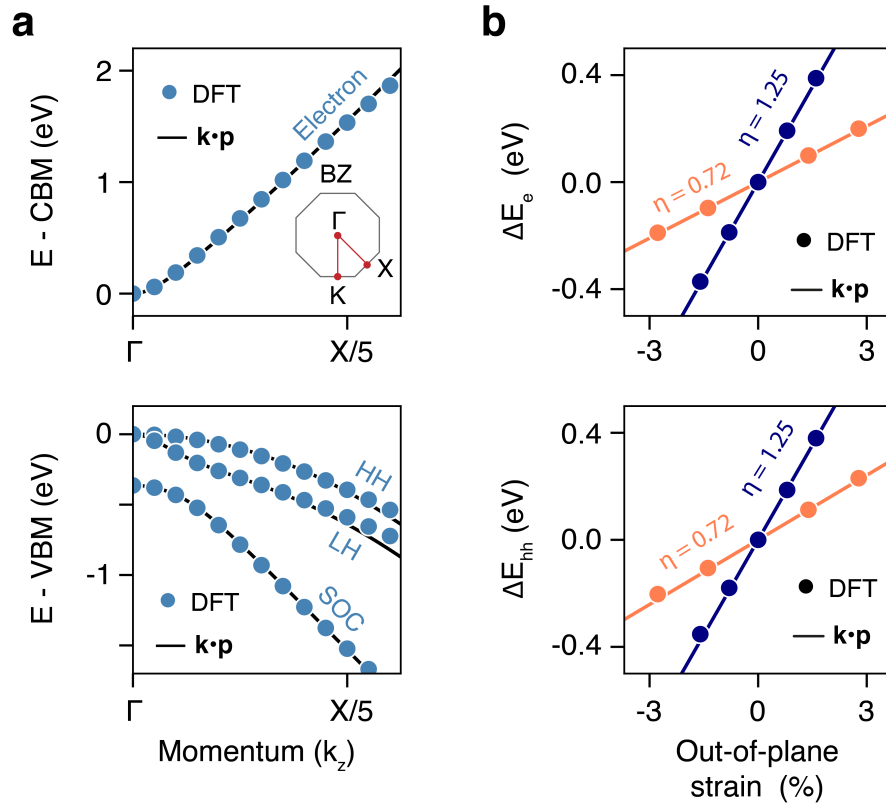
Figure 5.6: a) Band structure of unstrained bulk CdSe, showing agreement between our DFT (PBE) results (blue) and $\mathbf{k} \cdot \mathbf{p}$ model. b) The change in electron (top) and heavy-hole (bottom) energies of the bulk upon applied biaxial strain. The $\mathbf{k} \cdot \mathbf{p}$ model was parametrized using the data in orange, while the blue line is an extrapolation that shows good agreement with DFT.

by using Eqs. 5.3 and 5.4 and by fitting PBE data of the bulk material where the atomic structure had a biaxial strain ratio of η=0.72 (shown in orange), corresponding to the biaxial-strain ratio obtained using bulk elastic properties. The blue lines are an extrapolation of the model corresponding to η=1.25 (the average strain-ratio in our Cl- passivated NPLs) using the same deformation potentials. The close agreement between PBE results and eight-band model indicate that the model can accurately described band-dispersion and strain-induced changes on $E_{QP,bulk}$.

To include the effect of quantum confinement, we consider an infinite potential-well model that is often used in the literature to predict QP energies of NPLs [83]. The presence of infinite barriers forces the wave-function (envelope) to vanish at the top and bottom of the NPL, which leads to a discretization of the out-of-plane momentum ($k_z = n\pi/L_{NPL}$, $n=$ 1,2,...). Most importantly, the smallest k_z is non-zero and increases with decreasing NPL thickness (L_{NPL}). The confinement energy, E_{conf}, is then the difference between band-energy at finite k_z obtained by diagonalizing the eight-band model and the respective Γ-point energies. Our ability to correctly describe confinement therefore strongly depends on how accurately we describe the band-dispersion of the bulk.

In Fig. 5.7a we plot the confinement energy computed at the PBE level of theory for NPLs of different thickness and passivated with chlorine ligands. The confinement energy is obtained as $E_{conf}^{DFT} = E_{NPL}^{DFT} - E_{bulk}^{DFT}$. We compare the PBE confinement energy with that obtained with the infinite potential model. Our results show that the infinite potential model strongly overestimates the PBE results, suggesting that the hypothesis of an infinite barrier needs to be revisited.

The simplest way to go beyond the infinite-barrier assumption and model the effect of a finite-potential (V_0) on the QP gap, is to consider the heavy-hole (hh) and electron (e) separately [150], similar to our approach to describe the effective mass model including biaxial strain. We approximate the heavy-hole dispersion assuming a constant effective mass $[m_{hh} = m_0/(\gamma_1 - 2\gamma_2)]$, where γ_i are the modified Luttinger parameters of the bulk and m_0
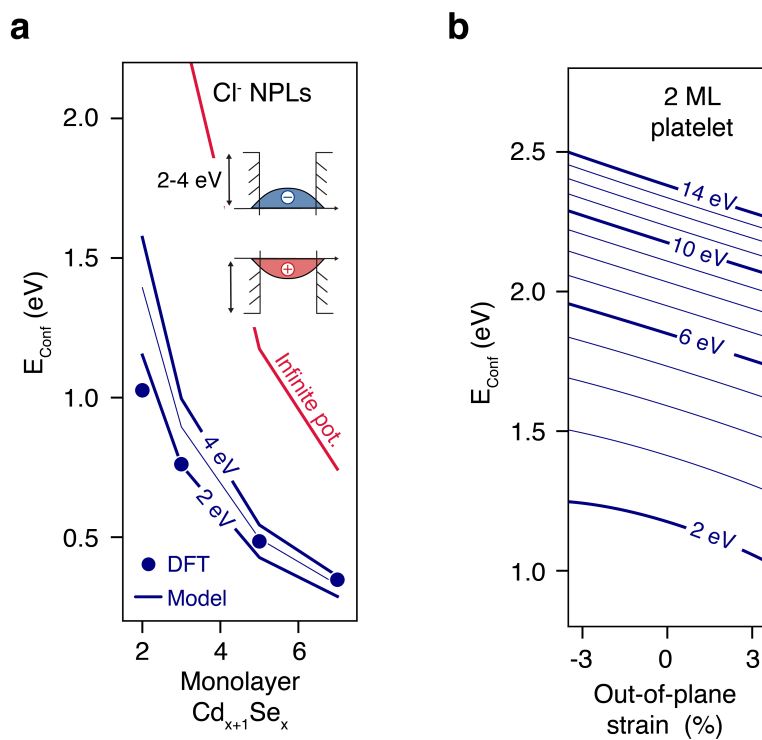
Figure 5.7: a) Charge carrier confinement energy in NPLs, comparing the finite (blue) and infinite (red) potential well models. b) Charge carrier confinement energy as a function of strain for the 2ML NPL using increasing finite potentials between 2 eV and 14 eV.

is the free-electron mass [11]. To account for the non-parabolicity of the electron dispersion, we use an energy dependent electron effective-mass $m_e(E)$ similar to Ref. [52, 129]:

$$m_0/m_e(E) = \alpha + \frac{E_p}{3}\left(\frac{2}{E} + \frac{1}{E + \Delta}\right) \tag{5.6}$$

where E_p is the Kane energy describing conduction and valence band mixing [11], α describes the coupling of the lowest electron-band to higher bands [52, 129, 51], and Δ is the energy-splitting of the valance band due to spin-orbit coupling. The electron effective-mass at the bottom of the band is obtained for $E = E_g$. Neglecting effects of non-parabolicity by assuming a constant m_e can lead to incorrect estimates of the confinement energy, especially for thin NPLs.

The heavy-hole ($E_{\text{hh,conf}}$) and electron ($E_{\text{e,conf}}$) confinement energies for a finite potential well are then obtained by solving an implicit equation for $m_i = m_{\text{hh}}$ and $m_i = m_e(E)$ respectively:

$$\tan\left(\frac{L_{\text{NPL}}}{2}\sqrt{2m_i E_{i,\text{conf}}}\right) = \sqrt{m_i\left(\frac{V_0}{E_{i,\text{conf}}} - 1\right)}. \tag{5.7}$$

Eq. 5.7, here given in atomic units, is obtained by imposing continuity and current-conserving boundary conditions [14] for the wave-function at the top and bottom of the NPL. As in Ref. [129], a free-electron mass is assumed for heavy-hole and electron in the vacuum region surrounding the NPLs. Strain-induced changes in the effective NPL-thickness are accounted for by L_{NPL}. Assuming different confinement potentials (V_0) for heavy-hole and electron is straightforward. The overall confinement energy (E_{conf}) is then given as the sum of $E_{\text{e,conf}}$ and $E_{\text{hh,conf}}$.

In general, the confinement potential (V_0) originates from the covalent interaction be-tween organic ligands and Cd atoms located on the surface. V_0 therefore sensitively depends on the type of ligand passivating the surface. In Fig. 5.7b we plot the confinement energy of a 2ML-thick NPL as a function of out-of-plane strain and for varying confinement potentials (V_0). Note that E_{conf} combines both $E_{\text{e,conf}}$ and $E_{\text{hh,conf}}$. Bulk parameters entering the

model are extracted from DFT calculations of the pristine and strained bulk. However, using experimental parameters [83] yields similar results. Our findings show that both out-of-plane strain and, to an even greater extent, V_0 sensitively affect the confinement energy.

We probe the strength of V_0 and the validity of the finite-potential model using our PBE calculations of NPLs passivated with Cl- ligands. By comparing the finite potential model plotted for different V_0 to PBE calculations, as shown in Fig. 5.7, we show that the two methods are in agreement for V_0 between 2 and 4 eV. Confining potentials of only a few eV stand in stark contrast to most previous reports that assume V_0 to be infinite.

To finally assess the effect of the dielectric environment on the fundamental band gap of our series of NPLs, we use a model proposed by Cho *et al.* [37] which offers a simple correction scheme to accurately estimate QP band gaps. This correction scheme is based upon the method of image charges [99], in which a self-energy, E_{self}, is calculated as the repulsive interaction between a charge inside and an infinite number of imaginary charges outside the NPL:

$$E_{\text{self}} = \frac{1}{\varepsilon_{in}d_{NPL}}\left[2\text{tanh}^{-1}(L_{12}) - \ln(1 - L_{12})\right] \tag{5.8}$$

where d_{NPL} is the NPL thickness and $L_{12} = (\varepsilon_{\text{in}} - \varepsilon_{\text{out}})/(\varepsilon_{\text{in}} + \varepsilon_{\text{out}})$. This scheme was validated for MoS_2 [37] and later used for CdSe NPLs [195] as an additive correction upon PBE calculations of NPLs.

We combine the effective mass model for the change in the band gap of bulk CdSe due to biaxial strain ($\Delta E_{\text{strain}}^{\text{bulk}}$) with the change in fundamental gap due to quantum confinement (E_{conf}) using a finite potential well model, and the self-energy (E_{self}) due to dielectric contrast using the model by Cho *et al.*, to estimate the quasi-particle energy (E_{QP}) of NPLs:

$$E_{\text{NPL}}^{\text{QP}} = E_{\text{QP,bulk}} + \Delta E_{\text{strain}}^{\text{bulk}} + E_{\text{conf}} + E_{\text{self}} \tag{5.9}$$

where $\Delta E_{\text{strain}}^{\text{bulk}}$, E_{conf}, and E_{self} are defined as in Eqs. 3-5. A value of 2.5 eV for V_0 was

assumed for all NPL thicknesses, as this was the average value found to match our PBE data. The effective masses entering the finite potential model (E_{conf}, Eq. 4), are taken from the eight-band $\mathbf{k} \cdot \mathbf{p}$-Hamiltonian of the strained bulk, parametrized using PBE calculations. Similarly, the deformation potentials entering $\Delta E_{\text{strain}}^{\text{bulk}}$ (Eq. 3) are extracted from the same calculations. In-plane and out-of-plane strain values are extracted from the relaxed NPL structures passivated by Cl-ligands. The same calculations are used to determine the NPL thickness (d_{NPL}), entering E_{self} (Eq. 5). Finally, for E_{self}, we take ε_{in} and ε_{out} to be 6.2 and 1, respectively, corresponding to the bulk dielectric constant of CdSe and that of vacuum. We take the experimental value of 1.66 eV for $E_{\text{QP,bulk}}$ [88].

The close agreement between this combined model and G_0W_0 calculations is shown in Fig. 5.5 and suggests that this model accurately describes the interplay between strain, quantum confinement and dielectric screening effects that ultimately determine quasiparticle gaps in NPLs.

5.4.3   Band Structure and Effective Masses of Nanoplatelets

In addition to the fundamental gaps presented in Section 5.4.1 and interpreted through models in 5.4.2, it is also important to understand how the full band structure of NPLs is affected by changes in strain and quantum confinement, particularly as it relates to changes in the effective masses that will be shown to be essential in the estimation of exciton binding energies in Section 5.5.1 using excitonic models.

Going from the 3D crystalline bulk of zinc blende CdSe to a 2D or quasi-2D counterpart requires careful comparison of band structures, as it is not necessarily straightforward to compare the 3D and 2D Brillouin zones. In 2D, the zinc blende Brillouin zone can be visualized as a slice through the 3D Brillouin, as shown in the schematic in Fig. 5.8b. While the full reciprocal space of the 2D NPLs is not directly comparable with that of the bulk, the high symmetry point commonly labeled X (or M) is identical in both dimensionalities. Thus, comparisons in band structure and effective masses between the bulk and NPLs are
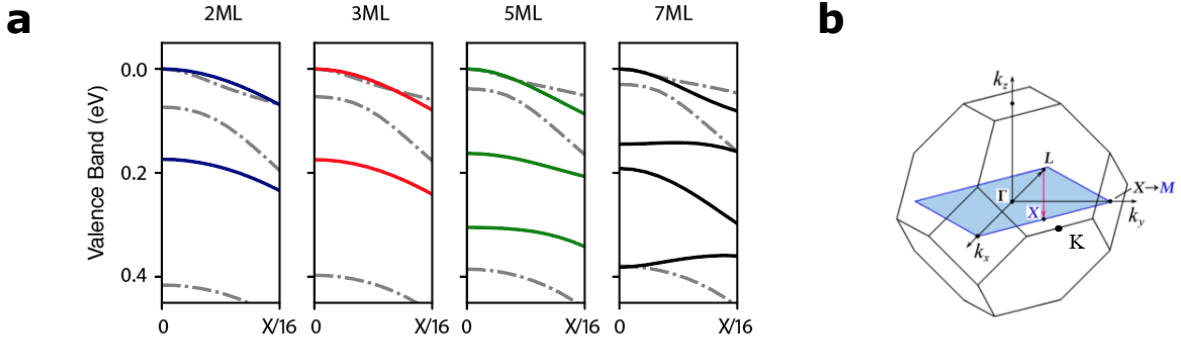
Figure 5.8: a) Valence band states (including SOC) near the band edge for 2ML-7ML NPLs, along the $\Gamma - X$ direction (colored lines) compared to the same states for biaxially strained bulk CdSe (gray dotted lines). b) Schematic of the Brillouin zone for the 3D Bulk and 2D NPLs (blue rectangle) [176]

done along the reciprocal space path between Γ and X.

In Fig. 5.8a we compute the valence band structure including spin-orbit coupling (SOC) for the 2ML, 3ML, 5ML and 7ML NPLs along the $\Gamma - X$ direction. In gray, we compare to the bandstructure of the NPL to the band structure of a biaxially strained bulk, subject to the same strain as the respective NPLs, where SOC has also been included. We find that while the dispersion of the valence band maximum (VBM) is similar to that of the bulk, the lower-lying bands all differ significantly. As the NPL thickness increases, we observe an increase in the number of subbands close to the VBM not present in the bulk dispersion. This is consistent with the results of Vasilev et al. [176]. The presence of energy subbands is typical for quantum-wells, and is best understood through the infinite confinement potential model described previously [186]. Energy subbands correspond either to the light- and spin-orbit-hole, with reduced energy compared to the heavy-hole due to quantum confinement and strain, or they can be assigned to heavy-hole states with finite out-of-plane momentum $k_z = n\pi/L_{\mathrm{NPL}}$, where n is larger than one. We also note the clear non-parabolicities of all bands of the NPLs that originate from both quantum confinement and strain effects.

In Fig. 5.9, we plot the reduced mass, μ, calculated using band structures at the PBE level of theory, where we define the reduced mass to include contributions from only the
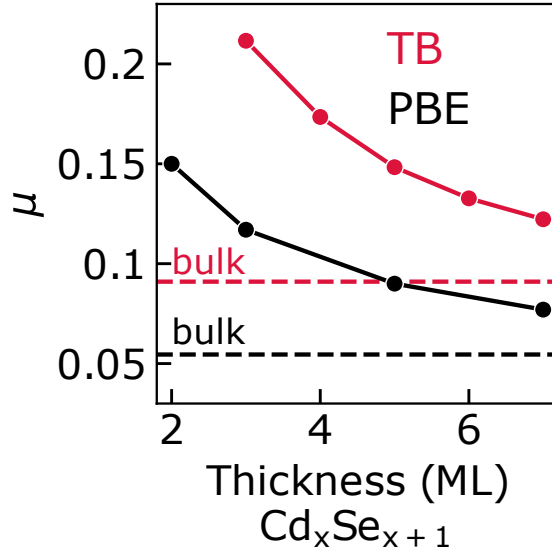
Figure 5.9: Reduced masses of NPLs computed using PBE (this work, black) and compared to Tight Binding calculations from Ref. [17] (red).

effective mass of the heavy hole (hh) and the electron (e):

$$\frac{1}{\mu} = \frac{1}{m_e} + \frac{1}{m_{hh}} \tag{5.10}$$

To the best of our knowledge, there are no direct experimental measurements of effective masses for CdSe NPLs, hence we compare our results with Tight Binding calculations of the reduced masses [17], which yielded results for the reduced mass of bulk CdSe in good agreement with experiment. Our effective masses calculated at the PBE level of theory are lower than literature results, which is unsurprising due to the level of theory, but we find that the trends and ratio of the reduced mass of the NPL to that of the bulk are in good agreement between our PBE results and that of Ref. [17]. Furthermore, in Table 5.1 we summarize all possible methods for calculating the reduced mass of bulk CdSe, and show that calculating the band structures using a hybrid functional such as DDH rather than PBE leads to a reduced mass in much better agreement with experiment. However, such calculations for NPLs are prohibitively costly due to the need for a extremely dense k-point

Table 5.1: Summary of reduced masses of bulk CdSe calculated using different methods and compared to experiment value taken from [83].

f. diff. (PBE)	f. diff. (PBE w/ SOC)	k · p (PBE)	k · p (PBE w/ SOC)	k · p (DDH)	exp. [83]
0.067	0.068	0.055	0.054	0.081	0.11

mesh near the Γ point.

5.4.4   Dielectric Constants of Nanoplatelets

For three dimensional materials such as bulk CdSe, there is a clear relation between the dielectric constant, ε, and refractive index, n: $\varepsilon = n^2$. For 2D-periodic systems such as nanoplatelets, however, there is no consensus in the literature regarding the definition of a dielectric constant particularly due to the necessity of defining a volume, Ω (see Eq. 3.11). For example, previous calculations of a 2D dielectric constant have been performed by using a volume based on the positions of the atoms in a unit cell (either including or excluding ligands), while others have suggested that the atom positions plus the covalent radii of the ligands is a preferred descriptor of the material thickness. Some authors [170, 132] have suggested that the dielectric constant is actually not sufficient for describing dielectric properties of 2D materials, instead pointing towards a 2D polarizability as the fundamental variable of interest. Olsen *et al.* [132] demonstrated that an *effective* dielectric constant could be determined by analytically averaging the screening felt by the exciton in the center of the 2D material using an effective Bohr radius. In this work we sought to define an effective dielectric constant by using a thickness defined by the electrostatic potential, which extends further away from the atoms than the covalent radii of the surface atoms by approximately 1 Å on either side, regardless of the NPL thickness. For example, for the 2ML NPL, we find an atom-to-atom thickness of 17.0933 Bohr, a covalent thickness of 20.9483 Bohr (where the covalent radii of Cl is 1.928 Bohr), and an electrostatic potential thickness of 23.2180 Bohr. In Table 5.2, we show how the value of the thickness defined using the electrostatic potential depends on the threshold chosen for the zero of the potential. We note that, near the edges
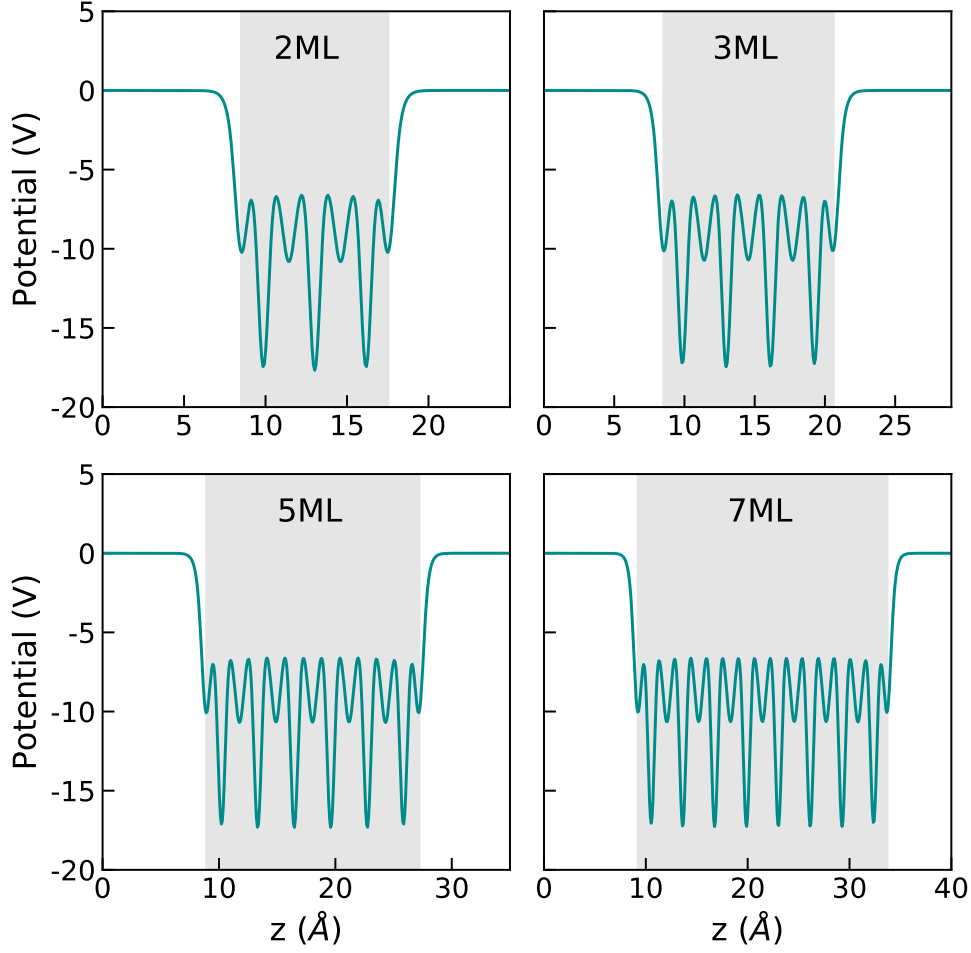
Figure 5.10: Planar-averaged electrostatic potential of the 2ML, 3ML, 5ML and 7ML NPLs. Gray boxes show the atom-to-atom thickness of the NPLs

of the unit cell, fluctuations of the electrostatic potential were on the order of 0.001 V.

We use the Effective Dielectric Model (EDM) from classical mechanics [170], where a 2D material surrounded by an external dielectric medium (in our case, vacuum) can be modelled by two capacitors in parallel (series) to compute the effective in-plane (out-of-plane) dielectric constant of the system:

$$\varepsilon_{eff,\parallel} = \varepsilon_{NPL}\frac{\delta}{L} + \varepsilon_{ext}(1 - \frac{\delta}{L}) \tag{5.11}$$

where δ is the thickness of the NPL and L is the full length of the unit cell including the

Table 5.2: NPL thickness for different definitions of the electrostatic potential threshold.

Threshold	Thickness (Å)
0.175 V (1% of max)	11.879
0.1 V	12.205
0.088 V (0.5% of max)	12.458
0.05 V	12.693
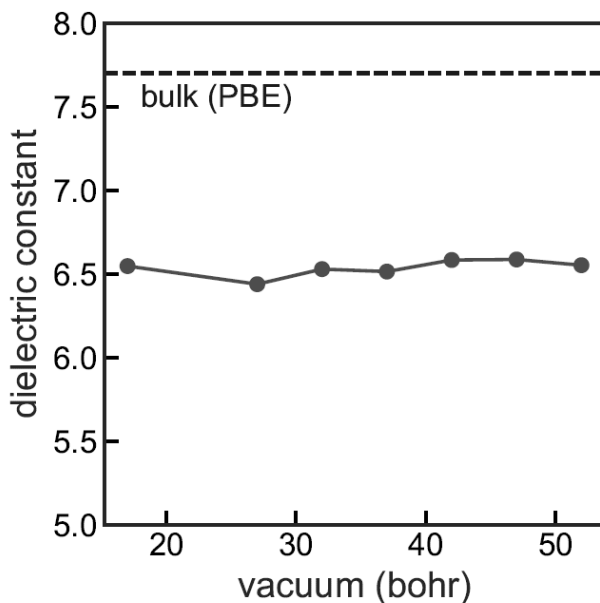
Figure 5.11: Effective dielectric constant calculated at the PBE level of theory with atom-to-atom thickness, as a function of increasing vacuum spacing. Dashed line shows the PBE dielectric constant of the bulk.

surrounding medium (vacuum). $\varepsilon_{eff,\parallel}$ is the total effective dielectric constant of the NPL and the surrounding medium (vacuum), which was calculated using the self-consistent dielectric-dependent hybrid (sc-DDH, see Section 3.2.3) functional and the method of finite fields. As expected, we find that both the in-plane and out-of-plane components of the total dielectric constant converge to 1 as the total unit cell lattice constant and the vacuum between periodic images in increased. On the contrary, by defining instead an effective volume of the NPL, ε_{NPL}, we obtain a value of the dielectric constant that is insensitive to the size of the vacuum layer, as shown in Fig. 5.11.

We additionally found that our sc-DDH effective dielectric constants calculated using finite fields were in good agreement with an estimation of the experimental effective dielectric

Table 5.3: Dielectric constant of bulk CdSe from exp. and calculated using sc-DDH, compared with the effective dielectric constant of the 2ML NPL estimated using Eq. 5.12 and calculated with one and two self-consistent iterations for DDH.

	bulk CdSe, exp.	bulk CdSe, sc-DDH	2ML NPL, exp. approx	2ML NPL, sc-DDH1	2ML NPL, sc-DDH2
ε	6.2	6.0	3.82	4.02	4.05

constant of the NPL calculated using a ratio of experimental and PBE values:

$$\varepsilon_{NPL,exp} \approx \frac{\varepsilon_{bulk,exp}}{\varepsilon_{bulk,PBE}} \varepsilon_{NPL,PBE} \tag{5.12}$$

We note that this expression is also used to estimate an initial input value for the fraction of exact exchange in sc-DDH calculations, which speeds up convergence of sc-DDH by requiring only two self-consistent iterations, for example as shown in Table 5.3 for the 2ML NPL, labeled "sc-DDH1" and "sc-DDH2". Comparison with the estimated value from Eq. 5.12 is provided as well.

In Fig. 5.12a, we present the dielectric constants calculated at sc-DDH using NPL thicknesses defined by the atom-to-atom distances, the covalent radii and the electrostatic potential. The total dielectric constant of the system, $\varepsilon_{eff,\parallel}$, was calculated using the finite field method (see Section 3.4.2) with a self-consistent dielectric-dependent hybrid (sc-DDH) functional, in which the inverse of the effective dielectric constant of the NPL, ε_{NPL}, was used in each case as the fraction of exact exchange and solved self-consistently until convergence (see Section 3.2.3) [158].

To validate our method of defining this 2D effective dielectric constant, we calculated the fundamental band gaps using the sc-DDH functional, where the fraction of exact exchange is again the inverse of the dielectric constant defined through the electrostatic potential. In Fig. 5.12b, we compare the sc-DDH fundamental band gaps to that of G_0W_0, presented and validated above in Section 5.4.1, and find that the fundamental gap calculated with sc-DDH underestimates the G_0W_0 by approximately 0.3-0.4 eV. Since the sc-DDH fundamental gap of bulk CdSe is slightly higher than the G_0W_0 gap (1.66 eV and 1.57 eV, respectively),
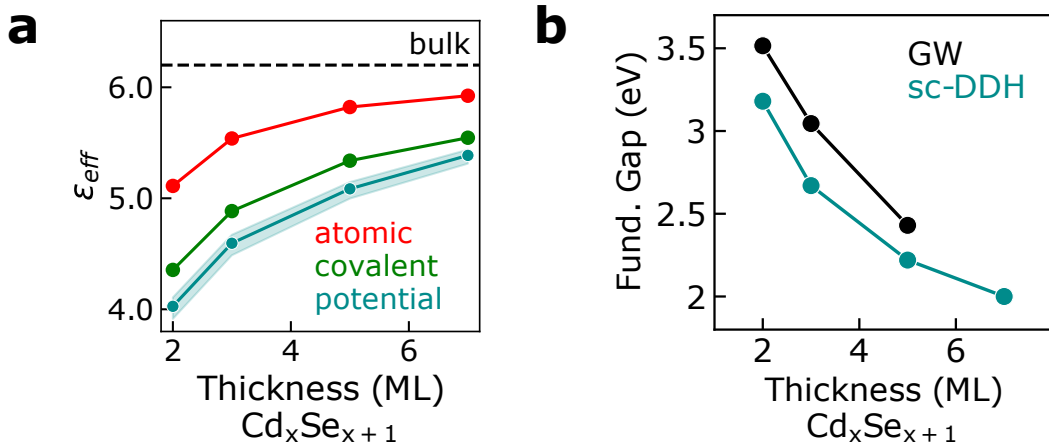
Figure 5.12: a) Effective dielectric constants of the NPLs calculated using three definitions of the NPL thickness: the atom-to-atom distance (red), the covalent radii (green) and the electrostatic potential (teal). Error bars on the teal curve represent the maximum and minimum thicknesses defined in Table 5.4.4. b) Fundamental band gaps calculated using sc-DDH compared to G_0W_0.

we attribute the underestimation of sc-DDH for the NPLs to a dielectric constant that is slightly too large. This corresponds to a thickness that is slightly too small, thus indicating that a more accurate screening length would actually be *larger* than that defined by the electrostatic potential, which is significant due to the fact that all previous attempts to define an effective 2D dielectric constant have used thicknesses smaller than the ones in the present study.

5.5   Optical Properties

5.5.1   Absorption Spectra and Exciton Binding Energies

Comparison with absorption experiments is critical for validating both calculations and models, as these experiments are essential for determining the photophysical properties of newly synthesized materials that may be applicable for photovoltaic devices. As such, while we calculated the fundamental band gap in Section 5.4.1, an understanding of the fundamental

gap alone is not sufficient without combining it with an investigation of the exciton binding energy, E_b, and finally the optical band gap, $E_{g,opt}$. Therefore, having computed the fundamental band gap of NPLs using G_0W_0 and having rationalized our results using a series of simple models, we now turn our focus to the exciton binding energy, E_b. We compute the optical absorption spectra and exciton binding energy using the Bethe-Salpeter equation, thus obtaining a direct calculation of E_b from first principles. We find the exciton binding energy of the 2ML NPL to be approximately 600 meV, reducing to 500 eV for 3ML. In Fig. 5.13a we show the absorption spectrum of 2ML CdSe calculated with BSE starting from PBE wavefunctions and a constant scissor correction equal to the difference between the fundamental band gaps at PBE and G_0W_0. The spectrum was calculated with a 15x15x1 k-point mesh, and includes transitions between 10 occupied and 10 unoccupied energy levels near the band edges. We stress the importance of convergence with respect to k-point mesh, as the BSE spectra were found to require a much denser mesh than the PBE or G_0W_0 band gaps alone. Our BSE calculations explicitly included spin-orbit coupling, as we found that qualitative agreement with experimental absorption spectra, as shown in Fig. 5.13a, could not otherwise be obtained because the first two peaks are widely attributed to the heavy hole and light hole first transitions [83].

Besides providing a value for the exciton binding energy for Cl- passivated NPLs, BSE calculations can help address discrepancies in assumptions used in models present in literature. Current exciton models either neglect (purely 2D models) or consider ("hybrid" models) the finite extension of the exciton wavefunction in the out-of-plane direction. Screened Coulomb interactions due to dielectric contrast are included in most, but not all, models, typically by using the image-charge method [195, 138]. Although in principle more accurate, including the finite extension of the wave-function significantly increases the computational complexity. Additional discrepancies arise in the choice of the reduced mass and dielectric constant entering the exciton models. While most calculations assume the bulk reduced mass (μ), our DFT calculations of NPLs, in line with previous reports [17], suggest that μ differs sub-
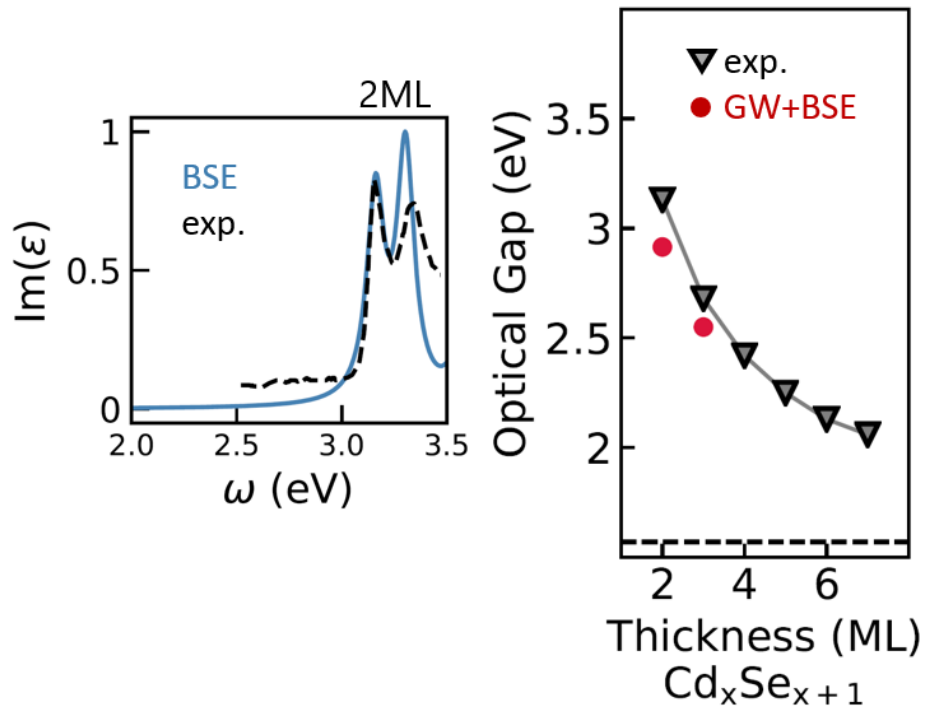
Figure 5.13: a) BSE spectrum of 2ML CdSe calculated using 15x15x1 k-point sampling compared to experimental data from [83]. BSE spectrum is plotted with a Lorentzian broadening of 0.05 eV. b) Optical band gaps using G_0W_0 fundamental gaps and E_b calculated from BSE
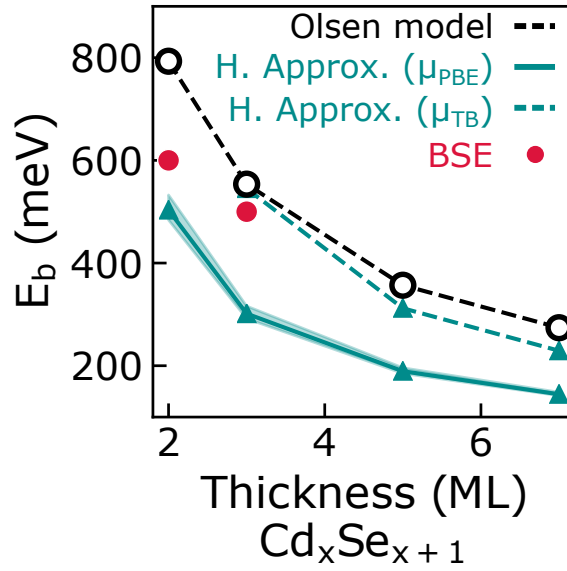
Figure 5.14: Exciton binding energies estimated using the Olsen model (black) and 2D Hydrogen Approximation (teal). Sensitivity to the effective mass is shown by comparison of values obtained using our PBE effective masses (solid teal line) to that with TB effective masses taken from the literature (dashed teal line) [17]

stantially from the bulk value as shown in Section 5.4.4. This effect originates both from confinement [186] and strain [11] and cannot be neglected. Furthermore, in most cases it is necessary to assume a dielectric constant for the semiconductor material, and usually the bulk value is used.

Using our BSE calculations, we probe the validity of the 2D Screened Hydrogen model proposed by Olsen et $al.$ [132], which uses a 2D polarizability rather than a dielectric constant as the fundamental variable to calculate the exciton binding energy. Comparison between Olsen's 2D Screened Hydrogen model and BSE (Fig 5.14, black and red, respectively) shows that the Olsen's model overestimates our BSE results for the 2ML and 3ML NPLs, with better agreement for the thicker 3ML NPL. This is consistent with observations by Olsen et $al.$, as they show that their model performs best for exciton binding energies below approximately 500 meV.

While Olsen et $al.$ presented an analytical expression for purely 2D materials that in-

corporates screening into the 2D Hydrogen Approximation, we propose that such screening may be inherently included by instead using effective dielectric constants for the NPLs such as those presented in Fig. 5.12a. We use the basic 2D Hydrogen Approximation:

$$E_{b,2D} = 4E_{b,3D} = \frac{2\mu}{\varepsilon^2} \tag{5.13}$$

where μ is the effective mass, ε is the dielectric constant, and the factor of 4 comes from dimensionality. The exciton binding energies calculated using the Hydrogen Approximation with the NPL effective dielectric constants (defined using the electrostatic potential) are shown in Fig. 5.14 as solid teal lines, and are found to be approximately 300-400 meV lower than those calculated by the Olsen model (black lines). However, we note the sensitivity of the Hydrogen Approximation to the effective masses, which is not the case for the Olsen model. Similar to the underestimation of effective masses using PBE (Section 5.4.3), the underestimation of the exciton binding energy is unsurprising. For a more direct comparison between the Olsen model and the Hydrogen Approximation using our effective dielectric constants, we thus used effective masses taken from the literature [17]. The results are shown as dashed teal line in Fig. 5.14, where we highlight the remarkable agreement with the Olsen model. This agreement between the Olsen model and Hydrogen Approximation implies that using effective dielectric constants of the NPLs defined using the electrostatic potential may inherently lead to the inclusion of screened Coulomb interactions, which are instead neglected when only the bulk dielectric constant is used in the Hydrogen Approximation. However, we note that models still overestimate our BSE calculations, particularly for the smallest NPL (Fig. 5.13).

A direct comparison between our BSE calculations and other exciton models present in the literature, including both purely 2D [195] and hybrid [17], is not possible due to the fact that they assume an external dielectric constant, $\varepsilon_{r,out}$, of 2 (organic ligands) while our BSE calculations intrinsically assume $\varepsilon_{r,out}$ to be 1 (vacuum). However, exciton binding energies calculated assuming $\varepsilon_{r,out}$ to be 2 instead of 1 are expected to be smaller [7, 37], which is

consistent with our observations. Comparison between BSE and other models that assume $\varepsilon_{r,out}$ to be 1 and use the same values for μ would provide additional physical insights on exact exciton character in NPLs and will be the focus of further studies.

5.5.2   Comparison of Optical Band Gaps to Experiment

By considering both the G_0W_0 fundamental gap and exciton binding energy, we compare our calculated optical gaps with experiment, as shown in Fig. 5.13b. We find good agreement using BSE as well as using the Olsen model and the Hydrogen Approximation with effective NPL dielectric constants defined using the electrostatic potential. Our optical gaps are additionally in decent agreement with Zhou *et al.* [195], where the fundamental gap is calculated with the model of Cho *et al.* based on PBE calculations and E_b is calculated using an effective mass model. We note that, while the E_b and fundamental band gap are both expected to be affected by changes in dielectric constant between the material and its environment, the optical band gap may be less sensitive to these changes, as suggested by Cho *et al.* for MoS_2 [37] due to cancellation of errors; indeed the E_b and fundamental gap are affected by dielectric contrast in opposite ways but by similar amounts.

5.6   Conclusions

In conclusion, we have presented calculations of the fundamental band gap and exciton binding energy of a series of CdSe NPLs calculated from G_0W_0 and BSE, respectively, which lead to optical gaps in good agreement with experimental absorption measurements [83, 36]. We rationalized our calculations of the fundamental gap using a model based on the effective mass approximation for the biaxially strained bulk material that further accounts for quantum confinement and dielectric contrast. Our BSE calculations provide the first calculations of the exciton binding energy for these materials without the need to employ an exciton model that makes assumptions regarding the strength of dielectric screening, extent

of the exciton in the material, and sensitivity of the effective masses to changes in NPL thickness through the number of layers or inherent strain.

We have shown that our model of the fundamental band gap predicts the quasiparticle energies of quasi-2D NPLs with nearly "GW" accuracy. The close agreement between our model and G_0W_0 calculations suggests that the model accurately describes the interplay between strain, quantum confinement and dielectric contrast effects that ultimately determine quasiparticle gaps in NPLs. However, we stress that our model points to a confining potential from the NPL surface of only a few eV, which is in stark contrast to most previous reports that assume infinite potential barriers.

Due to the reduced computational cost of our model compared to G_0W_0 calculations, this model could be used to predict the fundamental gaps of systems that are computationally challenging to calculate with G_0W_0, such as thick NPLs, NPLs with long organic ligands, or core/shell NPLs, and could be used for high-throughput screening of nanomaterials with optimal band gaps for photovoltaic devices, since only calculations of the strained bulk materials are required and the potential barrier, posed by the ligands or NPL shell, can be tuned systematically.

Finally, by combining our model of the fundamental gap with an accurate model for the exciton binding energy (either the model proposed by Olsen *et al.* [132] or the 2D Hydrogen Approximation using effective dielectric constants of the NPLs), we have presented a scalable framework for the calculation of the optical gap of NPLs that could be used for large NPLs without the need for computationally demanding G_0W_0 and BSE calculations. With such a scalable model, one could additionally investigate the more complex relationship between structure and optical properties of core/shell NPL heterostructures, where the interfaces between the core and shell introduce additional complexities in the biaxial strain profile. For example, in the experimental study of Hazarika, *et al.* [77], an unexplained decrease in optical gap was found for CdS/CdSe core/shell NPLs compared to pure CdSe NPLs. This previously surprising result can be rationalized through appreciation of the unique

interplay between biaxial strain, quantum confinement and dielectric contrast presented in this chapter, and further work could include using the models presented here to estimate the optical gaps of a series of core/shell NPLs, including the development of design rules for core/shell NPLs with engineered optoelectronic properties based on the protocol we have established for these calculations.

CHAPTER 6

ELECTRONIC PROPERTIES OF METAL-ORGANIC FRAMEWORKS

6.1   Introduction

As a final application of our electronic structure methods to the field of renewable energy, we show how spin-polarized Density Functional Theory calculations can be used to predict the stability of different spin states for a series of Metal Organic Frameworks (MOFs) of the formula M(BDC)(L) (M = Fe(II) or Co(II), BDC = 1,4-benzenedicarboxylate, L = pyrazine (pyz) or 4,4'-bipyridine (bipy)), in particular focusing in this study on Fe(BDC)(pyz). In conjunction with experiments, we show that these MOFs exist in a energetically favorable antiferromagnetic state at low temperature, with the ferromagnetic spin configurations higher in energy by approximately 30 meV. Although this barrier to switching between spin states is low, we attribute the stability of the anti-ferromagnetic state to the different preferred geometries for the three spin states.

6.2   Computational Framework

DFT calculations were performed using the Quantum Espresso [61] code under the Generalized Gradient Approximation (GGA) with Perdew-Burke-Ernzerhof (PBE) [134] parametrization and a plane-wave basis. Optimized Norm-Conserving Vanderbilt (ONCV) pseudopotentials [74] were chosen to approximate the potential of the core electrons, using a kinetic energy cutoff of 75 Ry. To account for the electronic interaction between partially filled Fe d

states and open up a gap between the valence and conduction bands, the DFT+U method was employed using a correlation energy (U) of 5 eV [48]. The value of U was chosen by scanning over a range of 2-5 eV, as shown in Fig. 6.1, and choosing the smallest value for which the pseudo-octahedral field Fe d electrons and the insulating band structure were accurately represented. This value of U is close to what has been used for DFT+U calculations in literature for other MOF and similar systems [192, 194].
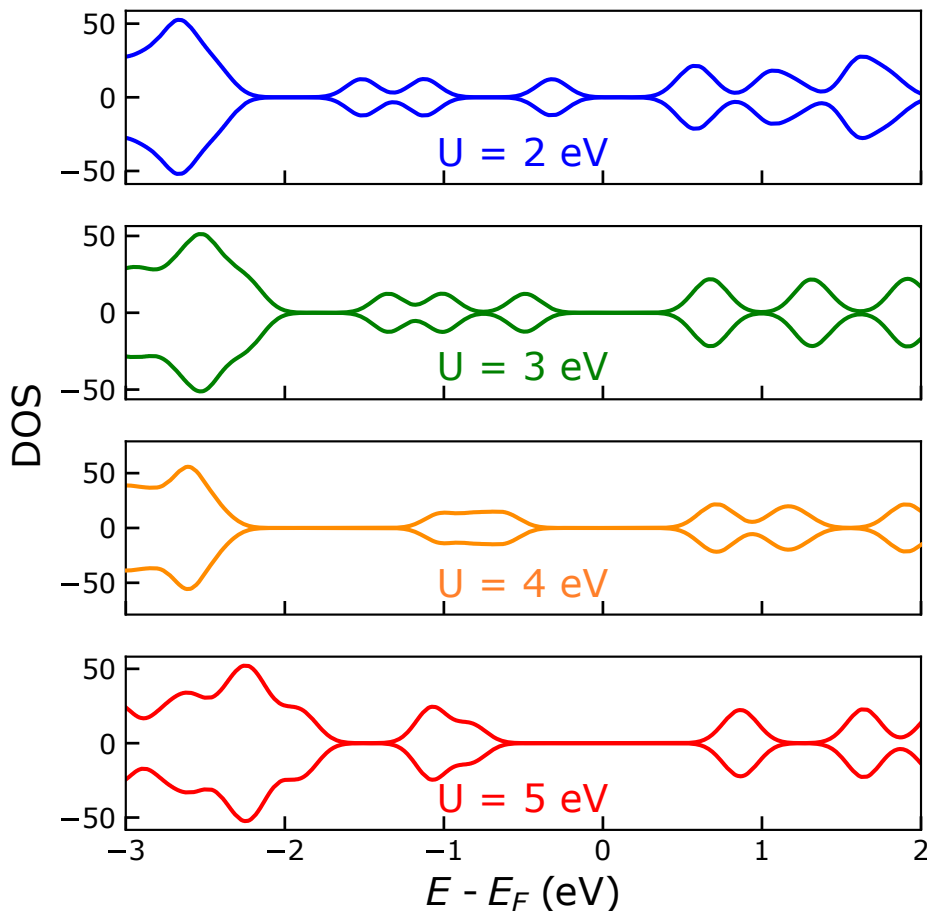
Figure 6.1: Total DOS as a function of increasing U parameter for antiferromagnetic Fe(BDC)(pyz). Positive and negative values correspond to spin-up and spin-down DOS, respectively.

All calculations were performed at the Gamma point and at the experimental lattice constant with a trigonal unit cell (space group P-3) containing 162 atoms and including 6 Fe

centers and two triangular pores (for a total of 636 valence electrons). Spin-Polarized Density Functional Theory was used to account for the different possible spin configurations of the Fe centers. Both antiferromagnetic (AFM) and ferromagnetic (FM) high-spin Fe systems were considered, as well as a non-magnetic (NM) low-spin Fe case. Stable spin states were found by varying the initial local magnetic moments of the Fe, O and N atoms, and enforcing a total magnetization of zero for AFM coupling. The geometry for each of these three systems was optimized at the PBE level of theory until forces on all atoms were less than 10^{-5} Ry Bohr^{-1}. Relaxed geometries were found to vary for the three spin configurations, with the most notable difference coming from the non-magnetic low-spin system which is the most strained at the fixed lattice constant.

6.3   Electronic Structure of Fe(II) MOFs

Metal-organic frameworks (MOFs) are characterized by high surface area and porosity that make them a natural choice for applications such as gas storage [126, 121, 54], separation [29, 23], and heterogeneous catalysis [113, 187]. In addition to studies utilizing MOFs for these applications, the electronic and magnetic properties of these porous systems have recently attracted increasing interest. Typically, MOFs include diamagnetic metal centers (e.g. Zn(II), Al(III), Zr(IV), etc.) or clusters combined with diamagnetic, insulating linkers which have no charge or spin carriers accessible for magnetic and electronic phenomena. Systems that do feature suitable paramagnetic ions frequently feature linkers that mediate weak electronic and magnetic coupling. Nevertheless, there has been substantial effort in developing porous materials that display antiferromagnetic or ferromagnetic coupling, spin canting, or conductivity.

In the context of expanding this class of materials, we have investigated metal centers with high S values, in conjunction with linkers that may support strong electronic or magnetic coupling. One such bidentate linker is pyrazine (pyz) which, along with its expanded analogue 4,4-bipyridine (bipy), has been shown to engender strong electronic coupling. De-
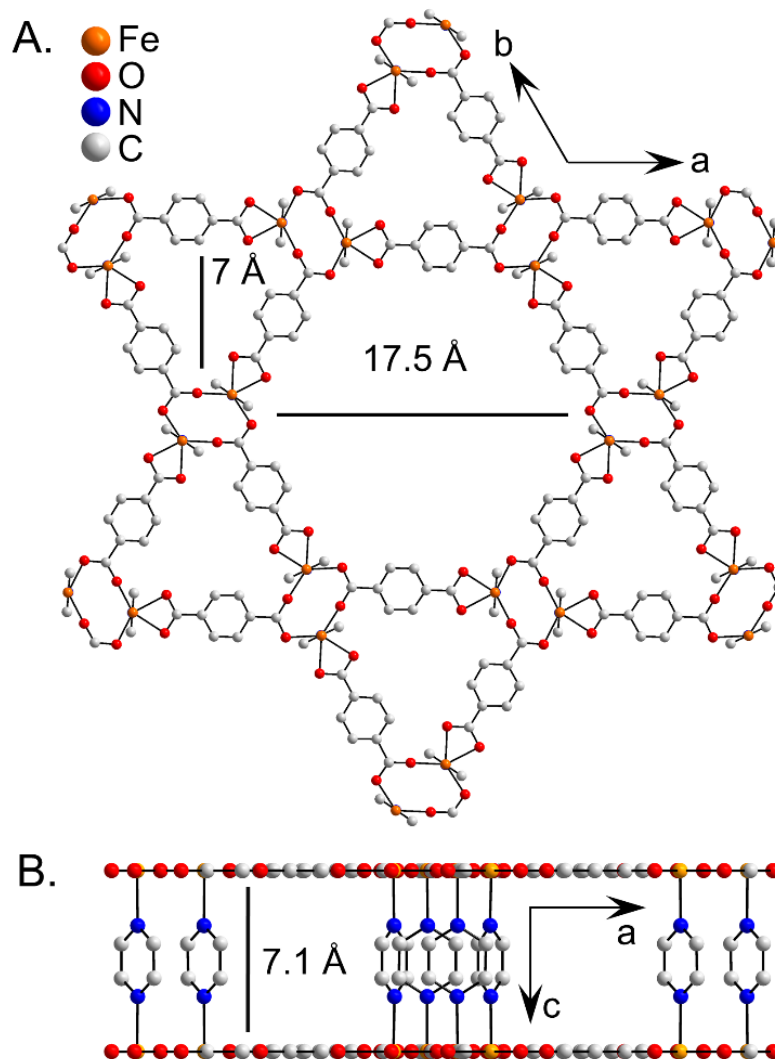
Figure 6.2: Structure of solvated Fe(BDC)(pyz) as determined by single crystal x-ray diffraction showing (A) the hexagonal and triangular pores and (B) the pyrazine axial ligands. H-atoms and disordered solvent have been omitted for clarity.

spite the ubiquity of these linkers in both discrete complexes and 1-D coordination polymers, the properties of 3D materials that incorporate these linkers and paramagnetic metal centers have not been thoroughly investigated. This limited depth of study has prompted us to investigate the ability of these linkers to mediate magnetic and electronic coupling between paramagnetic centers in a structurally confined 3D MOF scaffold. The combination of pyz or bipy with Fe(II) and Co(II) salts and 1,4-benzenedicarboxylate (BDC) provides a new family

92

of MOFs that feature high spin metal centers forming infinite chains with these linkers.

In this study, we used first principles calculations to probe the electronic properties of Fe(BDC)(pyz), one member of this family MOFs, whose experimentally determined 3D structure is shown in Fig. 6.2. Single crystal X-ray diffraction (SXRD) of solvated Fe(BDC)(pyz) revealed a structure consisting of Fe(BDC) sheets with 7 triangular pores and 17.5 hexagonal pores (Fig. 6.2A) pillared through each Fe(II) atom by pyz (Fig. 6.2B). Within the FeBDC sheet, Fe(II) is coordinated to two O atoms from one chelated BDC and two O atoms from two separate BDC μ-OCO bridges to an adjacent Fe(II). The SXRD crystal structure was used to generate initial atomic positions for our DFT calculations, which were then allowed to relax in three separate spin configurations to assess the relative stability of the antiferromagnetic (AFM), ferromagnetic (FM) and non-magnetic (NM) configurations of Fe(BDC)(pyz).

Our DFT+U calculations revealed an insulating band structure for all three spin configurations of Fe(BDC)(pyz), as can be seen in the Projected Density of States (PDOS) in Fig. 6.3A-C, with a filled valence band of primarily Fe d and O p character and an unpopulated N-based conduction band. The insulating band structure was consistent with room temperature, isotropic pressed pellet conductivity measurements, where the conductivity was too low to yield a linear potential vs. current relationship. The electronic structure and magnetic properties of Fe(BDC)(pyz) were also probed by temperature dependent magnetometry. In this experiment, a χT value can be obtained as a function of temperature, which can be compared to known values that relate to specific spin states. In particular, the χT_{300K} of Fe(BDC)(pyz) was found to be 2.74 cm^{-3} K/mol, which is comparable with the spin-only χT of 3 cm^{-3} K/mol expected for an S = 2 center consistent with high-spin Fe(II). The magnetometry experiments were coupled with Mössbauer data, which excluded the possibility of low-spin impurities. Fits to Mössbauer data yielded an isomer shift of 1.171(1) mm/s and quadrupole splitting of 3.198(2) mm/s, both of which are consistent with highspin Fe(II) [160, 116]. Thus, the magnetic and Mössbauer data strongly support a high-spin Fe(II)
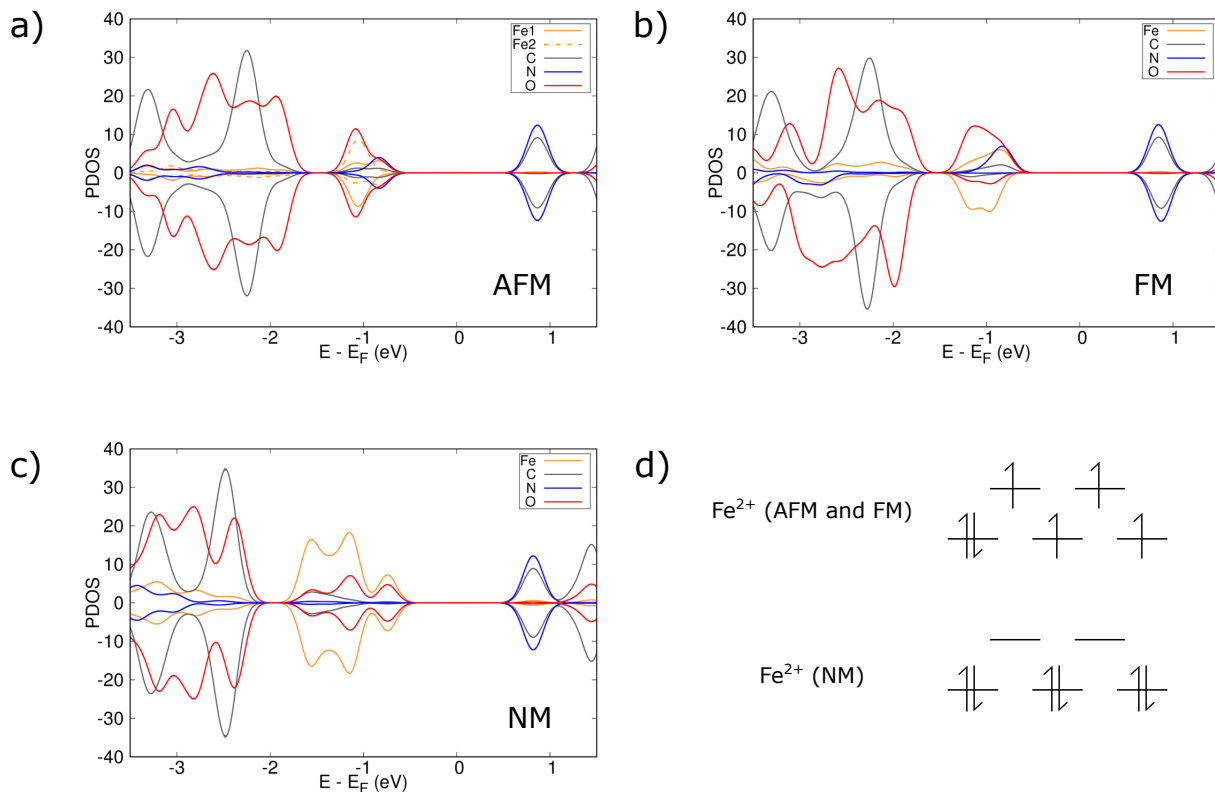
Figure 6.3: Projected Density of States for a) anti-ferromagnetic b) ferromagnetic and c) non-magnetic ordering. d) Diagram showing the high-spin electron configuration for AFM and FM and the low-spin configuration for NM ordering.

center, although the origin of the χT values, lower than expected, is not entirely clear.

We confirmed the experimentally predicted high-spin occupation with DFT for both the AFM and FM ordered systems, while the non-magnetic system exhibited low-spin occupation of the Fe centers (see Fig. 6.3D for a diagram of both possible spin states). A visualization of the electron density of the three systems can be seen in Fig. 6.4. In particular, the juxtaposition of spin-up (green) and spin-down (blue) Fe(II) centers can be seen for the AFM ordering, while for FM ordering each Fe(II) center is identical.

6.3.1   Stability of Fe(II) Spin States in Fe(BDC)(pyz) MOF

Experimentally, as temperature decreased, the χT value of Fe(BDC)(pyz) also decreased, which suggested some combination of antiferromagnetic coupling (rather than ferromag-
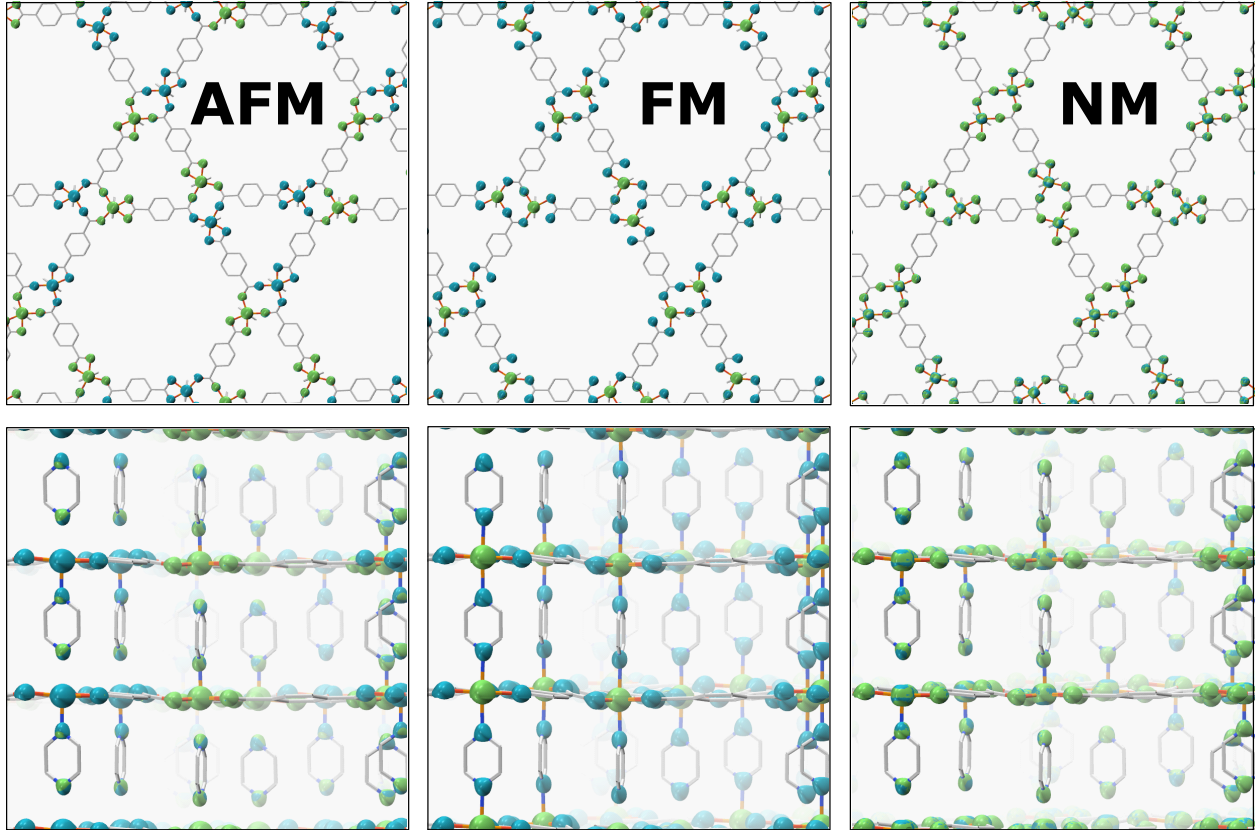
Figure 6.4: Spin-up (green) and spin-down (blue) electron density showing AFM (left), FM (center) and NM (right) ordering. Top panels show the in-plane structure; bottom panels show the axial ligands connecting the layers. Isosurfaces are shown at 15% of maximum value.

netic, which shares the high-spin occupation) and zerofield splitting effects. Our DFT+U calculations indicated that antiferromagnetic coupling is energetically favorable over the ferromagnetic system by 30 meV, with the energy differences between the three relaxed structures presented in Table 6.1.

Table 6.1: DFT+U calculated energy differences between antiferromagnetically (AFM), ferromagnetically (FM) and non-magnetically (NM, i.e. low-spin) coupled systems of Fe(BDC)(pyz).

	Energy Difference (eV)
AFM - FM	-0.0323 eV
AFM - NM	-14.1178 eV
FM - NM	-14.0855 eV

While this energy difference is somewhat small, we found that different relaxed geometries

for the three spin states suggest unfavorable switching and high energy barriers between states. In particular, the stress on the unit cell (Table 6.2) together with differences in bond angles (Table 6.3) points toward AFM ordering being preferred. By comparing the calculated bond angles of the AFM, FM and NM ordered systems to the angles measured with SXRD, we find the calculated AFM bond angles to be in good agreement with experiment.

Finally, we remark that spin crossover has been observed in the structurally similar $[\text{Fe}_2(\mu-\text{Bz})_2(\mu-\text{pyz})_2(\text{Bz})_2] \cdot (\text{HBz})$ system which is a 1-D chain with benzoate ligands [10]. Because spin crossover is accompanied by a change in bond length, as seen in $[\text{Fe}_2(\mu-\text{Bz})_2$-$(\mu-\text{pyz})_2(\text{Bz})_2] \cdot (\text{HBz})$, the lack of such behavior in Fe(BDC)(pyz) may be attributed to the structural restriction of the lattice [10, 70]. Indeed, it has previously been shown that Fe(II) spin crossover in MOFs is dependent on structural flexibility [73, 130]. Our DFT+U calculations predict that the lattice strain of d^6 Fe in a low-spin state would be energetically unfavorable by more than 5 eV, supporting that the rigid framework prevents spin crossover (Table 6.2).

Table 6.2: Stress on the unit cell for the three spin states at the experimental lattice constant and PBE relaxed geometry, and for the same geometry with the additional U parameter.

System	Stress at PBE (kbar)	Stress at PBE + U (kbar)
AFM	3.25	7.41
FM	-0.65	7.57
NM	-13.34	-8.09

Table 6.3: Comparison of bond angles for the three DFT systems and experimental AFM system. AFM 1 and AFM 2 indicate Fe(II) centers in the spin-up and spin-down configurations, respectively.

	Exp. (AFM)	AFM 1 (avg)	% diff.	AFM 2 (avg)	% diff.	FM (avg)	% diff.	NM (avg)	% diff.
Chelated O-Fe-O	60.24	61.71	2.44%	61.68	2.39%	61.76	2.52%	65.76	9.17%
Bridging O-Fe-O	125.35	112.06	-10.6%	112.80	-10.0%	113.52	-9.44%	104.67	-16.5%
N-Fe-N	178.23	176.99	-0.69%	177.06	-0.66%	177.37	-0.48%	179.59	0.76%

6.4   Conclusions

In summary, we used Spin-Polarized DFT+U calculations to characterize the metal-organic framework Fe(BDC)(pyz), a member of a new isoreticular series of MOFs that has been synthesized. Our DFT calculations, along with magnetometry measurements and Mössbauer spectroscopy, confirmed that the Fe metal centers are high-spin and in a 2+ oxidation state. Fe(BDC)(pyz) exhibits antiferromagnetic coupling, likely mediated by a combined effect from both the BDC and L ligands. The effect of structural confinement in these systems appears to quench possible spin canting or spin crossover phenomena, and illustrates the effect of the rigid 3D MOF structure. The materials in this series, including Fe(BDC)(pyz), represent rare examples where high-spin metal centers have been combined with pyrazine and bipyridine linkers in a highly porous extended solid.

CHAPTER 7

CONCLUSIONS

In this dissertation, we have investigated the collective and individual optoelectronic properties of nanomaterials that are used as thin films in photovoltaic devices. After establishing as a baseline the electronic structure of isolated lead sulfide nanoparticles and how they may be affected by temperature, we showed how the properties of these "building blocks" can change remarkably when one considers also the interactions between neighboring units and thus the *collective* properties of a solid made up of nanoparticles. In particular, we showed that while the fundamental band gaps of NPs only change slightly as a function of both temperature and interaction strength, the radiative lifetimes exhibit a much stronger dependence on interaction, becoming an order of magnitude less sensitive to temperature compared to those of isolated NPs. We found that weakly interacting NPs behave as fluctuating dipoles, with amplitudes on the order of 300% with respect to the average dipole moment, similar to those that we observed for the polarization of strongly interacting NP solids. We concluded that, at finite T the NP solids behave as dynamical, polarizable dipolar systems, which allowed us to provide a potential explanation for diverging results present in the literature for the dipole moments of lead chalcogenide NPs terminated with various ligands.

Having demonstrated the unique collective properties of NPs that can play a part in controlling the efficiencies of NP solar cell devices, we turned to a newer class of nanomaterials, namely quasi-two dimensional CdSe nanoplatelets, where the optoelectronic properties of the isolated building blocks had not yet been fully understood but which have the potential to out-perform NPs due to finer tunability of their optoelectronic properties. In collaboration with Sergio Mazzotti at ETH Zürich, we presented a computational protocol for studying these quasi-2D systems through combining first principles calculations with simple models. We offered the first calculations of the fundamental band gap of a series of CdSe NPLs from the accurate first-principles G_0W_0 method, as well as the first calculations of the absorption spectra and exciton binding energies of these materials using the Bethe-Salpeter Equation.

98

We rationalized our results using a series of simple models, probing the effects of strain, quantum confinement and dielectric contrast in isolated NPLs. By evaluating the changes in fundamental band gaps estimated through three simple models, we demonstrated that a combined model could be used to predict the quasiparticle energies of NPLs with nearly "GW" accuracy but greatly reduced computational cost. We thus offered a method that can be used to predict the fundamental gaps of complex systems such as thick NPLs, NPLs with long organic ligands, or core-shell NPLs, where the only calculations needed are that of the strained bulk materials and an estimate of the potential barrier, posed by the ligands or NPL shell, that can be tuned systematically or obtained through experiments. Overall, through comparing first principles calculations to models of fundamental gaps and exciton binding energies, as well as discussing the implications of dielectric properties of 2D materials, we offered insight into a framework that can be used to obtain the optoelectric properties of quasi-2D materials with reduced computational cost compared to state-of-the-art methods such as GW and BSE.

Finally, in collaboration with experimentalists in the Department of Chemistry at the University of Chicago, we demonstrated that a new class of porous, 3D Metal Organic Frameworks displays antiferromagnetic coupling between ion centers, which is a widely sought after attribute due to having spin carriers that are accessible for magnetic and electronic phenomena. We found that the effect of structural confinement in these systems reduced the possibility for spin canting or spin crossover phenomena, illustrating the effect of the rigid 3D structure.

From predicting specific optical properties of nanomaterials using some of the most accurate computational methods available, to interpreting the physical meaning behind their electronic structure, to understanding not just the properties of the individual nanomaterial but their collective behavior as they interact with one another, the work in this dissertation has advanced the field of renewable energy and paved the way for future work in finding optimal combinations of complex nanostructures that can push solar cell efficiencies beyond

current limitations.

REFERENCES

[1] a strain-induced exciton transition energy shift in cdse nanoplatelets: the impact of an organic ligand shell.

[2] National renewable energy laboratory best research-cell efficiencies. https://www.nrel.gov/pv/assets/pdfs/best-research-cell-efficiencies.20200406.pdf. Accessed: 2020-05-12.

[3] Qbox code: www.qboxcode.org.

[4] QD Solar: Our Technology. https://qdsolarinc.com/technology/. Accessed: 2020-06-24.

[5] Renewable Energy Explained. http://californiasolarcenter.org/history-pv/. Accessed: 2020-06-24.

[6] V.N. Abakumov, V.I. Perel, and I.N. Yassievich. *Nonradiative Recombination in Semiconductors*. Elsevier, Amsterdam, 1992.

[7] Alexander W. Achtstein, Andrei Schliwa, Anatol Prudnikau, Marya Hardzei, Mikhail V. Artemyev, Christian Thomsen, and Ulrike Woggon. Electronic structure and exciton-phonon interaction in two-dimensional colloidal cdse nanosheets. *Nano Letters*, 12(6):3151–3157, 2012.

[8] Carlo Adamo and Vincenzo Barone. Toward reliable density functional methods without adjustable parameters: the PBE0 model. *Journal of Chemical Physics*, 110(13):6158–6170, 1999.

[9] David M Adams, Louis Brus, Christopher E D Chidsey, Stephen Creager, Carol Creutz, Cherie R Kagan, Prashant V Kamat, Marya Lieberman, Stuart Lindsay, Rudolph A Marcus, Robert M Metzger, M E Michel-Beyerle, John R Miller, Marshall D Newton, Debra R Rolison, Otto Sankey, Kirk S Schanze, James Yardley, and Xiaoyang Zhu. Charge Transfer on the Nanoscale: Current Status. *Journal of Physical Chemistry B*, 107(28):6668–6697, 2003.

[10] Pilar Amo-Ochoa, Oscar Castillo, and Félix Zamora. Cu(I), Co(II) and Fe(II) coordination polymers with pyrazine and benzoate as ligands. Spin crossover, spin canting and metamagnetism phenomena. *Dalton Trans.*, 42:13453–13460, 2013.

[11] Thomas B Bahder. Eight-band k p model of strained zinc-blende crystals. *Physical Review B*, 41(17):11992, 1990.

[12] Stefano Baroni, Stefano de Gironcoli, Andrea Dal Corso, and Paolo Giannozzi. Phonons and related crystal properties from density-functional perturbation theory. *Rev. Mod. Phys.*, 73:515–562, 2001.

[13] Stefano Baroni, Paolo Giannozzi, and Andrea Testa. Green's-function approach to linear response in solids. *Phys. Rev. Lett.*, 58:1861, 1987.

[14] Gerald Bastard et al. Wave mechanics applied to semiconductor heterostructures. 1988.

[15] William J. Baumgardner, Kevin Whitham, and Tobias Hanrath. Confined-but-Connected Quantum Solids via Controlled Ligand Displacement. *Nano Letters*, 13(7):3225–3231, 2013.

[16] Axel D. Becke. Density-functional exchange-energy approximation with correct asymptotic behavior. *Physical Review A*, 38(6):3098–3100, 1988.

[17] Ramzi Benchamekh, Nikolay A Gippius, Jacky Even, MO Nestoklon, J-M Jancu, S Ithurria, Benoît Dubertret, Al L Efros, and Paul Voisin. Tight-binding calculations of image-charge effects in colloidal nanoscale platelets of cdse. *Physical Review B*, 89(3):035307, 2014.

[18] Lorin X. Benedict, Aaron Puzder, Andrew J. Williamson, Jeffrey C. Grossman, Giulia Galli, John E. Klepeis, Jean-Yves Raty, and O. Pankratov. Calculation of optical absorption spectra of hydrogenated Si clusters: Bethe-Salpeter equation versus time-dependent local-density approximation. *Phys. Rev. B.*, 68:085310, 2003.

[19] Lorin X. Benedict and E. L. Shirley. Ab initio calculation of $\varepsilon_2(\omega)$ including the electron-hole interaction: Application to GaN and CaF$_2$. *Phys. Rev. B.*, 59:5441, 1999.

[20] Federica Bertolotti, Dmitry N. Dirin, Maria Ibáñez, Frank Krumeich, Antonio Cervellino, Ruggero Frison, Oleksandr Voznyy, Edward H. Sargent, Maksym V. Kovalenko, Antonietta Guagliardi, and Norberto Masciocchi. Crystal symmetry breaking and vacancies in colloidal lead chalcogenide quantum dots. *Nature Materials*, 15(9):987–994, 2016.

[21] Satria Zulkarnaen Bisri, Elena Degoli, Nicola Spallanzani, Gopi Krishnan, Bart Jan Kooi, Corneliu Ghica, Maksym Yarema, Wolfgang Heiss, Olivia Pulci, Stefano Ossicini, and Maria Antonietta Loi. Determination of the Electronic Energy Levels of Colloidal Nanocrystals using Field-Effect Transistors and Ab-Initio Calculations. *Advanced Materials*, 26(32):5639–5645, 2014.

[22] Sean A. Blanton, Robert L. Leheny, Margaret A. Hines, and Philippe Guyot-Sionnest. Dielectric Dispersion Measurements of CdSe Nanocrystal Colloids: Observation of a Permanent Dipole Moment. *Physical Review Letters*, 79(5):865–868, 1997.

[23] Witold M. Bloch, Ravichandar Babarao, Matthew R. Hill, Christian J. Doonan, and Christopher J. Sumby. Post-synthetic Structural Processing in a Metal-Organic Framework Material as a Mechanism for Exceptional CO$_2$/N$_2$ Selectivity. *Journal of the American Chemical Society*, 135(28):10441–10448, 2013.

[24] Steven G. Boxer. Stark Realities. *The Journal of Physical Chemistry B*, 113(10):2972–2983, 2009.

[25] Paul V. Braun, Paul Osenar, and Samuel I. Stupp. Semiconductibandlng superlattices templated by molecular assemblies. *Nature*, 380(6572):325–328, 1996.

[26] Nicholas P. Brawand, Marco Govoni, Márton Vörös, and Giulia Galli. Performance and self-consistency of the generalized dielectric dependent hybrid functional. *J. Chem. Theory Comput.*, 13:3318, 2017.

[27] Nicholas P. Brawand, Márton Vörös, and Giulia Galli. Surface dangling bonds are a cause of B-type blinking in Si nanoparticles. *Nanoscale*, 7(8):3737–3744, 2015.

[28] Nicholas P. Brawand, Márton Vörös, Marco Govoni, and Giulia Galli. Generalization of dielectric dependent hybrid functionals to finite systems. *Phys. Rev. X*, 6:041002, 2016.

[29] David Britt, Hiroyasu Furukawa, Bo Wang, T. Grant Glover, and Omar M. Yaghi. Highly efficient separation of carbon dioxide by a metal-organic framework replete with open metal sites. *PNAS*, 106(49):20637–20640, 2009.

[30] Patrick R. Brown, Donghun Kim, Richard R. Lunt, Ni Zhao, Moungi G. Bawendi, Jeffrey C. Grossman, and Vladimir Bulovi. Energy level modification in lead sulfide quantum dot thin films through ligand exchange. *ACS Nano*, 8(6):5863–5872, 2014.

[31] Giovanni Bussi, Davide Donadio, and Michele Parrinello. Canonical sampling through velocity rescaling. *The Journal of Chemical Physics*, 126(1):014101, 2007.

[32] Marco Califano, Alberto Franceschetti, and Alex Zunger. Lifetime and polarization of the radiative decay of excitons, biexcitons, and trions in CdSe nanocrystal quantum dots. *Physical Review B*, 75(11):115401, 2007.

[33] R. Car and M. Parrinello. Unified approach for molecular dynamics and density-functional theory. *Physical review letters*, 55(22):2471, 1985.

[34] Ou Chen, Jing Zhao, Vikash P Chauhan, Jian Cui, Cliff Wong, Daniel K Harris, He Wei, Hee-Sun Han, Dai Fukumura, Rakesh K Jain, et al. Compact high-quality CdSe-CdS core-shell nanocrystals with narrow emission linewidths and suppressed blinking. *Nature materials*, 12(5):445–451, 2013.

[35] A. A. Chistyakov, M. A. Zvaigzne, V. R. Nikitenko, A. R. Tameev, I. L. Martynov, and O. V. Prezhdo. Optoelectronic Properties of Semiconductor Quantum Dot Solids for Photovoltaic Applications. *The Journal of Physical Chemistry Letters*, 8:4129–4139, 2017.

[36] Wooje Cho, Siyoung Kim, Igor Coropceanu, Vishwas Srivastava, Benjamin T. Diroll, Abhijit Hazarika, Igor Fedin, Giulia Galli, Richard D. Schaller, and Dmitri V. Talapin. Direct synthesis of six-monolayer (1.9 nm) thick zinc-blende cdse nanoplatelets emitting at 585 nm. *Chemistry of Materials*, 30(20):6957–6960, 2018.

[37] Yeongsu Cho and Timothy C Berkelbach. Environmentally sensitive theory of electronic and optical transitions in atomically thin semiconductors. *Physical Review B*, 97(4):041409, 2018.

[38] Ji-Hyuk Choi, Aaron T. Fafarman, Soong Ju Oh, Dong-Kyun Ko, David K. Kim, Benjamin T. Diroll, Shin Muramoto, J Greg Gillen, Christopher B. Murray, and Cherie R. Kagan. Bandlike Transport in Strongly Coupled and Doped Quantum Dot Solids: A Route to High-Performance Thin-Film Electronics. *Nano Letters*, 12(5):2631–2638, 2012.

[39] C. P. Collier, T. Vossmeyer, and J. R. Heath. NANOCRYSTAL SUPERLATTICES. *Annual Review of Physical Chemistry*, 49(1):371–404, 1998.

[40] V. L. Colvin and A. P. Alivisatos. CdSe nanocrystals with a dipole moment in the first excited state. *The Journal of Chemical Physics*, 97(1):730–733, 1992.

[41] V. L. Colvin, K. L. Cunningham, and A. P. Alivisatos. Electric field modulation studies of optical absorption in CdSe nanocrystals: Dipolar character of the excited state. *The Journal of Chemical Physics*, 101(8):7122–7138, 1994.

[42] Ryan W Crisp, Daniel M Kroupa, Ashley R Marshall, Elisa M Miller, Jianbing Zhang, Matthew C Beard, and Joseph M Luther. Metal halide solid-state surface treatment for high efficiency PbS and PbSe QD solar cells. *Scientific Reports*, 5:9945, 2015.

[43] Quanqin Dai, Yu Zhang, Yingnan Wang, Michael Z. Hu, Bo Zou, Yiding Wang, and William W. Yu. Size-Dependent Temperature Effects on PbSe Nanocrystals. *Langmuir*, 26(13):11435–11440, 2010.

[44] Stefano de Gironcoli. Lattice dynamics of metals from density-functional perturbation theory. *Physical Review B*, 51(10):6773, 1995.

[45] P. Dey, J. Paul, J. Bylsma, D. Karaiskaj, J.M. Luther, M.C. Beard, and A.H. Romero. Origin of the temperature dependence of the band gap of PbS and PbSe quantum dots. *Solid State Communications*, 165:49–54, 2013.

[46] Dmitriy S. Dolzhnikov, Hao Zhang, Jaeyoung Jang, Jae Sung Son, Matthew G. Panthani, Tomohiro Shibata, Soma Chattopadhyay, and Dmitri V. Talapin. Composition-matched molecular solders for semiconductors. *Science*, 347(6220):425–428, 2015.

[47] Walter S. Drisdell, Roberta Poloni, Thomas M. McDonald, Jeffrey R. Long, Berend Smit, Jeffrey B. Neaton, David Prendergast, and Jeffrey B. Kortright. Probing adsorption interactions in metalorganic frameworks using x-ray spectroscopy. *Journal of the American Chemical Society*, 135(48):18183–18190, 2013.

[48] S. L. Dudarev, G. A. Botton, S. Y. Savrasov, C. J. Humphreys, and A. P. Sutton. Electron-energy-loss spectra and the structural stability of nickel oxide: An LSDA+U study. *Phys. Rev. B.*, 57:1505, 1998.

[49] Marion Dufour, Junling Qu, Charlie Gréboval, Christophe Méthivier, Emmanuel Lhuillier, and Sandrine Ithurria. Halide ligands to release strain in cadmium chalcogenide nanoplatelets and achieve high brightness. *ACS nano*, 13(5):5326–5334, 2019.

[50] Emmanuel A. Echiegu. Nanotechnology as a Tool for Enhanced Renewable Energy Application in Developing Countries. *J. Fundam. Renewable Energy Appl.*, 6(6), 2016.

[51] Al L Efros and M Rosen. Quantum size level structure of narrow-gap semiconductor nanocrystals: Effect of band coupling. *Physical Review B*, 58(11):7120, 1998.

[52] Alexey I Ekimov, F Hache, MC& al Schanne-Klein, D Ricard, Chr Flytzanis, IA Kudryavtsev, TV Yazeva, AV Rodina, and Al L Efros. Absorption and intensity-dependent photoluminescence measurements on cdse quantum dots: assignment of the first electronic transitions. *JOSA B*, 10(1):100–107, 1993.

[53] G. E. Engel and B. Farid. Generalized plasmon-pole model and plasmon band structures of crystals. *Phys. Rev. B.: Condens. Matter Mater. Phys.*, 47:15931–15934, 1993.

[54] Omar K. Farha, A. Özgür Yazaydn, Ibrahim Eryazici, Christos D. Malliakas, Brad G. Hauser, Mercouri G. Kanatzidis, SonBinh T. Nguyen, Randall Q. Snurr, and Joseph T. Hupp. De novo synthesis of a metal-organic framework material featuring ultrahigh surface area and gas storage capacities. *Nature Chemistry*, 2:944–948, 2010.

[55] B Farid, R Daling, D Lenstra, and W van Haeringen. GW approach to the calculation of electron self-energies in semiconductors. *Physical Review B*, 38(11):7530, 1988.

[56] Nancy C. Forero-Martinez, Ha-Linh Thi Le, Ning Ning, Holger Vach, and Hans-Christian Weissker. Temperature dependence of the radiative lifetimes in Ge and Si nanocrystals. *Nanoscale*, 7(11):4942–4948, 2015.

[57] A. Franceschetti. First-principles calculations of the temperature dependence of the band gap of Si nanocrystals. *Physical Review B*, 76(16):161301, 2007.

[58] Adam Gali, Márton Vörös, Dario Rocca, Gergely T. Zimanyi, and Giulia Galli. High-Energy Excitations in Silicon Nanoparticles. *Nano Letters*, 9(11):3780–3785, 2009.

[59] Yunan Gao, Mark C. Weidman, and William A. Tisdale. CdSe Nanoplatelet Films with Controlled Orientation of their Transition Dipole Moment. *Nano Letters*, 17(6):3837–3843, 2017.

[60] Jaco J. Geuchies, Carlo van Overbeek, Wiel H. Evers, Bart Goris, Annick de Backer, Anjan P. Gantapara, Freddy T. Rabouw, Jan Hilhorst, Joep L. Peters, Oleg Konovalov, Andrei V. Petukhov, Marjolein Dijkstra, Laurens D. A. Siebbeles, Sandra van Aert, Sara Bals, and Daniel Vanmaekelbergh. In situ study of the formation mechanism of two-dimensional superlattices from PbSe nanocrystals. *Nature Materials*, 15(12):1248–1254, 2016.

[61] Paolo Giannozzi, Stefano Baroni, Nicola Bonini, Matteo Calandra, Roberto Car, Carlo Cavazzoni, Davide Ceresoli, Guido L Chiarotti, Matteo Cococcioni, Ismaila Dabo, Andrea Dal Corso, Stefano de Gironcoli, Stefano Fabris, Guido Fratesi, Ralph Gebauer, Uwe Gerstmann, Christos Gougoussis, Anton Kokalj, Michele Lazzeri, Layla Martin-Samos, Nicola Marzari, Francesco Mauri, Riccardo Mazzarello, Stefano Paolini, Alfredo Pasquarello, Lorenzo Paulatto, Carlo Sbraccia, Sandro Scandolo, Gabriele Sclauzero, Ari P Seitsonen, Alexander Smogunov, Paolo Umari, and Renata M Wentzcovitch. QUANTUM ESPRESSO: a modular and open-source software project for quantum simulations of materials. *Journal of Physics: Condensed Matter*, 21(39):395502, 2009.

[62] Federico Giberti, Márton Vörös, and Giulia Galli. Design of Heterogeneous Chalcogenide Nanostructures with Pressure-Tunable Gaps and without Electronic Trap States. *Nano Letters*, 17(4):2547–2553, 2017.

[63] R. W. Godby and R. J Needs. Metal-insulator transition in Kohn-Sham theory and quasiparticle theory. *Phys. Rev. Lett.*, 62:1169–1172, 1989.

[64] Dorothea Golze, Marc Dvorak, and Patrick Rinke. The GW Compendium: A Practical Guide to Theoretical Photoemission Spectroscopy. *Frontiers in Chemistry*, 7(377):1–66, 2019.

[65] Xavier Gonze and J-P Vigneron. Density-functional approach to nonlinear-response coefficients of solids. *Physical Review B*, 39(18):13120, 1989.

[66] Marco Govoni and Giulia Galli. Large Scale GW Calculations. *J. Chem. Theory. Comput.*, 11(6):2680–2696, 2015.

[67] Marco Govoni, Ivan Marri, and Stefano Ossicini. Carrier multiplication between interacting nanocrystals for fostering silicon-based photovoltaics. *Nature Photonics*, 6(10):672–679, 2012.

[68] M. Green. *Third Generation Photovoltaics: Advanced Solar Energy Conversion.* Springer, Berlin, 2006.

[69] Morton E Gurtin, GURTIN ME, and MURDOCH AI. Surface stress in solids. 1978.

[70] Philipp Gütlich, Yann Garcia, and Harold A. Goodwin. Spin crossover phenomena in Fe(II) complexes. *Chem. Soc. Rev.*, 29:419–427, 2000.

[71] F. Gygi. Architecture of Qbox: A scalable first-principles molecular dynamics code. *IBM Journal of Research and Development*, 52(1.2):137–144, 2008.

[72] F. Gygi, Jean-Luc Fattebert, and Eric Schwegler. Computation of Maximally Localized Wannier Functions using a simultaneous diagonalization algorithm. *Computer Physics Communications*, 155(1):1–6, 2003.

[73] Gregory J. Halder, Cameron J. Kepert, Boujemaa Moubaraki, Keith S. Murray, and John D. Cashion. Guest-Dependent Spin Crossover in a Nanoporous Molecular Framework Material. *Science*, 298(5599):1762–1765, 2002.

[74] D. R. Hamann. Optimized Norm-Conserving Vanderbilt Pseudopotentials. *Physical Review B*, 88(8):085117, 2013.

[75] D. R. Hamann, M. Schluter, and C. Chiang. Norm-Conserving Pseudopotentials. *Physical Review Letters*, 43:1494–1497, 1979.

[76] M. C. Hanna and A. J. Nozik. Solar conversion efficiency of photovoltaic and photoelectrolysis cells with carrier multiplication absorbers. *Journal of Applied Physics*, 100(7):074510, 2006.

[77] Abhijit Hazarika, Igor Fedin, Liang Hong, Jinglong Guo, Vishwas Srivastava, Wooje Cho, Igor Coropceanu, Joshua Portner, Benjamin T. Diroll, John P. Philbin, Eran Rabani, Robert Klie, and Dmitri V. Talapin. Colloidal Atomic Layer Deposition with Stationary Reactant Phases Enables Precise Synthesis of "Digital" IIVI Nanoheterostructures with Exquisite Control of Confinement and Strain. *J. Am. Chem. Soc.*, 141(34):13487–13496, 2019.

[78] Lars Hedin. New method for calculating the one-particle Green's function with application to the electron-gas problem. *Physical Review*, 139:A796, 1965.

[79] N.E. Hill, W.E. Vaughn, A.H. Price, and M. Davies. *Dielectric Properties and Molecular Behavior*. Von Nostrand Reinhold, London, 1969.

[80] Pierre Hohenberg and Walter Kohn. Inhomogeneous electron gas. *Physical Review*, 136:B864–B871, 1964.

[81] Mark S Hybertsen and Steven G Louie. First-principles theory of quasiparticles: calculation of band gaps in semiconductors and insulators. *Physical review letters*, 55(13):1418, 1985.

[82] Mark S Hybertsen and Steven G Louie. Electron correlation in semiconductors and insulators: Band gaps and quasiparticle energies. *Physical Review B*, 34(8):5390, 1986.

[83] S Ithurria, MD Tessier, B Mahler, RPSM Lobo, B Dubertret, and Al L Efros. Colloidal nanoplatelets with two-dimensional electronic structure. *Nature Materials*, 10(12):936, 2011.

[84] Sandrine Ithurria and Dmitri V. Talapin. Colloidal Atomic Layer Deposition (c-ALD) using Self-Limiting Reactions at Nanocrystal Surface Coupled to Phase Transfer between Polar and Nonpolar Media. *J. Am. Chem. Soc.*, 134(45):18585–18590, 2012.

[85] Jaeyoung Jang, Dmitriy S. Dolzhnikov, Wenyong Liu, Sooji Nam, Moonsub Shim, and Dmitri V. Talapin. Solution-Processed Transistors Using Colloidal Nanocrystals with Composition-Matched Molecular Solders: Approaching Single Crystal Mobility. *Nano Letters*, 15(10):6309–6317, 2015.

[86] Cherie R. Kagan and Christopher B. Murray. Charge transport in strongly coupled quantum dot solids. *Nature Nanotechnology*, 10:1013–1026, 2015.

[87] Hideyuki Kamisaka, Svetlana V. Kilina, Koichi Yamashita, and Oleg V. Prezhdo. Ab Initio Study of Temperature and Pressure Dependence of Energy and Phonon-Induced Dephasing of Electronic Excitations in CdSe and PbSe Quantum Dots. *The Journal of Physical Chemistry C*, 112(21):7800–7808, 2008.

[88] Y. D. Kim, M. V. Klein, S. F. Ren, Y.C. Chang, H. Luo, N. Samarth, and J. K. Furdyna. Optical properties of zinc-blende CdSe and $Zn_xCd_{1-x}Se$ films grown on gaas. *Phys. Rev. B.*, 49(11):7262–7270, 1994.

[89] R.D. King-Smith and David Vanderbilt. Theory of polarization of crystalline solids. *Physical Review B*, 47:1651(R), 1993.

[90] Victor I. Klimov. Multicarrier Interactions in Semiconductor Nanocrystals in Relation to the Phenomena of Auger Recombination and Carrier Multiplication. *Annual Review of Condensed Matter Physics*, 5(1):285–316, 2014.

[91] Mark Klokkenburg, Arjan J Houtepen, Rolf Koole, Julius W J De Folter, Ben H Erné, Ernst Van Faassen, and Daniel Vanmaekelbergh. Dipolar Structures in Colloidal Dispersions of PbSe and CdSe Quantum Dots. *Nano Letters*, 7(9):2931–2936, 2007.

[92] Kevin M Knowles. The biaxial moduli of cubic materials subjected to an equi-biaxial elastic strain. *Journal of Elasticity*, 124(1):1–25, 2016.

[93] Weon-kyu Koh, Naveen K. Dandu, Andrew F. Fidler, Victor I. Klimov, Jeffrey M. Pietryga, and Svetlana V. Kilina. Thickness-Controlled Quasi-Two-Dimensional Colloidal PbSe Nanoplatelets. *Journal of the American Chemical Society*, 139(6):2152–2155, 2017.

[94] Walter Kohn and Lu Jeu Sham. Self-consistent equations including exchange and correlation effects. *Physical Review*, 140:A1133–A1138, 1965.

[95] Maksym V. Kovalenko, Liberato Manna, Andreu Cabot, Zeger Hens, Dmitri V. Talapin, Cherie R. Kagan, Victor I. Klimov, Andrey L. Rogach, Peter Reiss, Delia J. Milliron, Philippe Guyot-Sionnnest, Gerasimos Konstantatos, Wolfgang J. Parak, Taeghwan Hyeon, Brian A. Korgel, Christopher B. Murray, and Wolfgang Heiss. Prospects of Nanoscience with Nanocrystals. *ACS Nano*, 9(2):1012–1057, 2015.

[96] Maksym V. Kovalenko, Marcus Scheele, and Dmitri V. Talapin. Colloidal Nanocrystals with Molecular Metal Chalcogenide Surface Ligands. *Science*, 324(5933):1417–1420, 2009.

[97] Boris Kozinsky and Nicola Marzari. Static Dielectric Properties of Carbon Nanotubes from First Principles. *Physical Review Letters*, 96(16):166801, 2006.

[98] Daniel M. Kroupa, Márton Vörös, Nicholas P. Brawand, Brett W. McNichols, Elisa M. Miller, Jing Gu, Arthur J. Nozik, Alan Sellinger, Giulia Galli, and Matthew C. Beard. Tuning colloidal quantum dot band edge positions through solution-phase surface chemistry modification. *Nature Communications*, 8:15257, 2017.

[99] Masami Kumagai and Toshihide Takagahara. Excitonic and nonlinear-optical properties of dielectric quantum-well structures. *Physical Review B*, 40(18):12359, 1989.

[100] Xinzheng Lan, Menglu Chen, Margaret H. Hudson, Vladislav Kamysbayev, Yuanyuan Wang, Philippe Guyot-Sionnest, and Dmitri V. Talapin. Quantum dot solids showing state-resolved band-like transport. *Nature Materials*, 19:323–329, 2020.

[101] Xinzheng Lan, Oleksandr Voznyy, F. Pelayo García de Arquer, Mengxia Liu, Jixian Xu, Andrew H. Proppe, Grant Walters, Fengjia Fan, Hairen Tan, Min Liu, Zhenyu Yang, Sjoerd Hoogland, and Edward H. Sargent. 10.6% Certified Colloidal Quantum Dot Solar Cells via Solvent-Polarity-Engineered Halide Passivation. *Nano Letters*, 16(7):4630–4634, 2016.

[102] David C. Langreth and M. J. Mehl. Beyond the local-density approximation in calculations of ground-state electronic properties. *Physical Review B*, 28(4):1809, 1983.

[103] Adèle D. Laurent and Denis Jacquemin. TD-DFT benchmarks: A review. *International Journal of Quantum Chemistry*, 113(17):2019–2039, 2013.

[104] C.T. Lee, W.T. Yang, and R.G. Parr. Development of the Colle-Salvetti Correlation-Energy Formula into a Fuctional of the Electron-Density. *Physical Review B.*, 37:785, 1988.

[105] J.-S. Lee, M. V. Kovalenko, J. Huang, D. S. Chung, and D. V. Talapin. Band-like transport, high electron mobility and high photoconductivity in all-inorganic nanocrystal arrays. *Nature Nanotechnology*, 6:348–352, 2011.

[106] R. Leitsmann and F. Bechstedt. Characteristic Energies and Shifts in Optical Spectra of Colloidal IVVI Semiconductor Nanocrystals. *ACS Nano*, 3(11):3505–3512, 2009.

[107] Xia Leng, Fan Jin, Min Wei, and Yuchen Ma. GW method and Bethe-Salpeter equation for calculating electronic excitations. *Advanced Review*, 6(5):532–550, 2016.

[108] Huashan Li, David Zhitomirsky, Shreya Dave, and Jeffrey C. Grossman. Toward the Ultimate Limit of Connectivity in Quantum Dots with High Mobility and Clean Gaps. *ACS Nano*, 10(1):606–614, 2016.

[109] Liang-shi Li and A. Paul Alivisatos. Origin and Scaling of the Permanent Dipole Moment in CdSe Nanorods. *Physical Review Letters*, 90(9):097402, 2003.

[110] Songping Luo, Miri Kazes, Hong Lin, and Dan Oron. Strain-Induced Type II Band Alignment Control in CdSe Nanoplatelet/ZnS-Sensitized Solar Cells. *The Journal of Physical Chemistry C*, 121(21):11136–11143, 2017.

[111] Joseph M. Luther, Matt Law, Matthew C. Beard, Qing Song, Matthew O. Reese, Randy J. Ellingson, and Arthur J. Nozik. Schottky Solar Cells Based on Colloidal Nanocrystal Films. *Nano Letters*, 8(10):3488–3492, 2008.

[112] Georgy I. Maikov, Roman Vaxenburg, Aldona Sashchiuk, and Efrat Lifshitz. Composition-Tunable Optical Properties of Colloidal IVVI Quantum Dots, Composed of Core/Shell Heterostructures with Alloy Components. *ACS Nano*, 4(11):6547–6556, 2010.

[113] Kuntal Manna, Pengfei Ji, Zekai Lin, Francis X. Greene, Ania Urban, Nathan C. Thacker, and Wenbin Lin. Chemoselective single-site Earth-abundant metal catalysts at metalorganic framework nodes. *Nature Communications*, 7:12610, 2016.

[114] Narbe Mardirossian and Martin Head-Gordon. Thirty years of density functional theory in computational chemistry: an overview and extensive assessment of 200 density functionals. *Molecular Physics*, 115(19):2315–2372, 2017.

[115] Andrea Marini, Conor Hogan, Myrta Grüning, and Daniele Varsano. Yambo: An ab initio tool for excited state calculations. *Computer Physics Communications*, 180:1392–1403, 2009.

[116] Maria Angeles. Martinez-Lorente, Vasili. Petrouleas, Jean Michel. Savariault, Richard. Poinsot, Marc. Drillon, and Jean Pierre. Tuchagues. Bis(4-imidazoleacetato)iron.bis(methanol): a 2d antiferromagnetic iron(ii) system exhibiting 3d long-range ordering with a net magnetic moment at 15 k. *Inorganic Chemistry*, 30(19):3587–3589, 1991.

[117] D. Marx and J. Hutter. *Ab Initio Molecular Dynamics: Basic Theory and Advanced Methods*. Cambridge University Press, 2009.

[118] Dominik Marx and Jürg Hutter. *Ab initio molecular dynamics: basic theory and advanced methods*. Cambridge University Press, 2009.

[119] Nicola Marzari, Arash A. Mostofi, Jonathan R. Yates, Ivo Souza, and David Vanderbilt. Maximally localized Wannier functions: Theory and applications. *Reviews of Modern Physics*, 84(4):1419–1475, 2012.

[120] Nicola Marzari, Ivo Souza, and David Vanderbilt. An Introduction to Maximally Localized Wannier Functions. *Scientific Highlight of the Month*, 57:129–168, 2003.

[121] Jarad A. Mason, Julia Oktawiec, Mercedes K. Taylor, Matthew R. Hudson, Julien Rodriguez, Jonathan E. Bachman, Miguel I. Gonzalez, Antonio Cervellino, Antonietta Guagliardi, Craig M. Brown, Philip L. Llewellyn, Norberto Masciocchi, and Jeffrey R. Long. Methane storage in flexible metalorganic frameworks with intrinsic thermal management. *Nature*, 527:357–361, 2015.

[122] Thomas M. McDonald, Jarad A. Mason, Xueqian Kong, Gygi David Bloch, Eric D., Alessandro Dani, Valentina Crocellà, Filippo Giordanino, Samuel O. Odoh, Walter S. Drisdell, Bess Vlaisavljevich, Allison L. Dzubak, Roberta Poloni, Sondre K. Schnell, Nora Planas, Kyuho Lee, Tod Pascal, Liwen F. Wan, David Prendergast, Jeffrey B. Neaton, Berend Smit, Jeffrey B. Kortright, Laura Gagliardi, Silvia Bordiga, Jeffrey A. Reimer, and Jeffrey R. Long. Cooperative insertion of CO_2 in diamine-appended metal-organic frameworks. *Nature*, 519:303–308, 2015.

[123] William J Morokoff and Russel E Caflisch. Quasi-monte carlo integration. *Journal of computational physics*, 122(2):218–230, 1995.

[124] C. B. Murray, C. R. Kagan, and M. G. Bawendi. Synthesis and Characterization of Monodisperse Nanocrystals and Close-Packed Nanocrystal Assemblies. *Annual Review of Materials Science*, 30(1):545–610, 2000.

[125] C B Murray, D J Noms, and M G Bawendi. Synthesis and Characterization of Nearly Monodisperse CdE (E = S, Se, Te) Semiconductor Nanocrystallites. *J. Am. Chem. Soc*, 115:8706–8715, 1993.

[126] Leslie J. Murray, Mircea Dinca, and Jeffrey R. Long. Hydrogen storage in metalorganic frameworks. *Chem. Soc. Rev.*, 38:1294–1314, 2009.

[127] Gautham Nair, Liang-Yi Chang, Scott M Geyer, and Moungi G Bawendi. Perspective on the Prospects of a Carrier Multiplication Nanocrystal Solar Cell. *Nano Letters*, 11(5):2145–2151, 2011.

[128] Zhijun Ning, Oleksandr Voznyy, Jun Pan, Sjoerd Hoogland, Valerio Adinolfi, Jixian Xu, Min Li, Ahmad R. Kirmani, Jon-Paul Sun, James Minor, Kyle W. Kemp, Haopeng Dong, Lisa Rollny, André Labelle, Graham Carey, Brandon Sutherland, Ian Hill, Aram Amassian, Huan Liu, Jiang Tang, Osman M. Bakr, and Edward H. Sargent. Air-stable n-type colloidal quantum dot solids. *Nature Materials*, 13(8):822–828, 2014.

[129] David J Norris and MG Bawendi. Measurement and assignment of the size-dependent optical spectrum in cdse quantum dots. *Physical Review B*, 53(24):16338, 1996.

[130] Masaaki Ohba, Ko Yoneda, Gloria Agustí, M. Carmen Muñoz, Ana B. Gaspar, José A. Real, Mikio Yamasaki, Hideo Ando, Yoshihide Nakao, Shigeyoshi Sakaki, and Susumu Kitagawa. Bidirectional Chemo-Switching of Spin State in a Microporous Framework. *Angewandte Chemie International Edition*, 48(26):4767–4771, 2009.

[131] A. Olkhovets, R.-C. Hsu, A. Lipovskii, and F. W. Wise. Size-Dependent Temperature Variation of the Energy Gap in Lead-Salt Quantum Dots. *Physical Review Letters*, 81(16):3539–3542, 1998.

[132] Thomas Olsen, Simone Latini, Filip Rasmussen, and Kristian S. Thygesen. Simple screened hydrogen model of excitons in two-dimensional materials. *Phys. Rev. Lett.*, 116:056401, 2016.

[133] Lazaro A. Padilha, John T. Stewart, Richard L. Sandberg, Wan Ki Bae, Weon-Kyu Koh, Jeffrey M. Pietryga, and Victor I. Klimov. Carrier Multiplication in Semiconductor Nanocrystals: Influence of Size, Shape, and Composition. *Accounts of Chemical Research*, 46(6):1261–1269, 2013.

[134] John P. Perdew, Kieron Burke, and Matthias Ernzerhof. Generalized Gradient Approximation Made Simple. *Physical Review Letters*, 77(18):3865–3868, 1996.

111

[135] J.P. Perdew and A. Zunger. Self-interaction correction to density-functional approximations for many-electron systems. *Physical Review B.*, 23:5048, 1981.

[136] John Perlin. Passive Solar History. https://www.eia.gov/energyexplained/renewablesources/. Accessed: 2020-06-24.

[137] Yuan Ping, Dario Rocca, and Giulia Galli. Electronic excitations in light absorbers for photoelectrochemical energy conversion: first principles calculations based on many body perturbation theory. *Chemical Society Reviews*, 42(6):2437–2469, 2013.

[138] Josep Planelles, Alexander W Achtstein, Riccardo Scott, Nina Owschimikow, Ulrike Woggon, and Juan I Climente. Tuning intraband and interband transition rates via excitonic correlation in low-dimensional semiconductors. *ACS Photonics*, 5(9):3680–3688, 2018.

[139] Eran Rabani, Balázs Hetényi, B. J. Berne, and L. E. Brus. Electronic properties of CdSe nanocrystals in the absence and presence of a dielectric medium. *The Journal of Chemical Physics The Journal of Chemical Physics*, 110(115):5355, 1999.

[140] Raffaele Resta. Macroscopic polarization in crystalline dielectrics: the geometric phase approach. *Reviews of Modern Physics*, 66:899, 1994.

[141] Dario Rocca, Deyu Lu, and Giulia Galli. Ab initio calculations of optical absorption spectra: Solution of the Bethe-Salpeter equation within density matrix perturbation theory. *J. Chem. Phys.*, 133:164109, 2010.

[142] Dario Rocca, Yuan Ping, Ralph Gebauer, and Giulia Galli. Solution of the Bethe-Salpeter equation without empty electronic states: Application to the absorption spectra of bulk systems. *Phys. Rev. B.*, 85:045116, 2012.

[143] R. Rossetti, S. Nakahara, and L. E. Brus. Quantum size effects in the redox potentials, resonance Raman spectra, and electronic spectra of CdS crystallites in aqueous solution. *The Journal of Chemical Physics*, 79(2):1086–1088, 1983.

[144] Clare E. Rowland, Igor Fedin, Hui Zhang, Stephen K. Gray, Alexander O. Govorov, Dmitri V. Talapin, and Richard D. Schaller. Picosecond energy transfer and multiexciton transfer outpaces Auger recombination in binary CdSe nanoplatelet solids. *Nature Materials*, 14:484–489, 2015.

[145] Davide Sangalli, Andrea Ferretti, Henrique Miranda, Claudio Attaccalite, Ivan Marri, Elena Cannuccia, Pedro Miguel Melo, Margherita Marsili, Fulvio Paleari, Antimo Marrazzo, Gianluca Prandini, Pietro Bonfà, Michael O. Atambo, Fabio Affinito, Maurizia Palummo, Alejandro Molina Sanchez, Conor Hogan, Myrta Grüning, Daniele Varsano, and Andrea Marini. Many-body perturbation theory calculations using the yambo code. *Journal of Physics: Condensed Matter*, 31:325902, 2019.

[146] A Sashchiuk, L Amirav, M Bashouti, M Krueger, U Sivan, and E Lifshitz. PbSe Nanocrystal Assemblies: Synthesis and Structural, Optical, and Electrical Characterization. *Nano Letters*, 4(1):159–165, 2003.

[147] Benjamin H. Savitzky, Robert Hovden, Kevin Whitham, Jun Yang, Frank Wise, Tobias Hanrath, and Lena F. Kourkoutis. Propagation of Structural Disorder in Epitaxially Connected Quantum Dot Solids from Atomic to Micron Scale. *Nano Letters*, 16(9):5714–5718, 2016.

[148] Peter Scherpelz, Marco Govoni, Ikutaro Hamada, and Giulia Galli. Implementation and Validation of Fully Relativistic GW Calculations: Spin-Orbit Coupling in Molecules, Nanocrystals, and Solids. *J. Chem. Theory Comput.*, 12(8):3523–3544, 2016.

[149] Constanze Schliehe, Beatriz H. Juarez, Marie Pelletier, Sebastian Jander, Denis Greshnykh, Mona Nagel, Andreas Meyer, Stephan Foerster, Andreas Kornowski, Christian Klinke, and Horst Weller. Ultrathin PbS Sheets by Two-Dimensional Oriented Attachment. *Science*, 329(5991):550–553, 2010.

[150] MFH Schuurmans et al. Simple calculations of confinement states in a quantum well. *Physical Review B*, 31(12):8041, 1985.

[151] Octavi E. Semonin, Joseph M. Luther, and Matthew C. Beard. Quantum dots for next-generation photovoltaics. *Materials Today*, 15(11):508–515, 2012.

[152] Octavi E. Semonin, Joseph M. Luther, Sukgeun Choi, Hsiang-Yu Chen, Jianbo Gao, Arthur J. Nozik, and Matthew C. Beard. Peak External Photocurrent Quantum Efficiency Exceeding 100% via MEG in a Quantum Dot Solar Cell. *Science*, 334(6062):1530–1533, 2011.

[153] J. Seufert, M. Obert, M. Scheibner, N. A. Gippius, G. Bacher, A. Forchel, T. Passow, K. Leonardi, and D. Hommel. Stark effect and polarizability in a single CdSe/ZnSe quantum dot. *Applied Physics Letters*, 79(7):1033–1035, 2001.

[154] Sachin Shanbhag and Nicholas A Kotov. On the Origin of a Permanent Dipole Moment in Nanocrystals with a Cubic Crystal Lattice: Effects of Truncation, Stabilizers, and Medium for CdS Tetrahedral Homologues. *Journal of Physical Chemistry B Letters*, 110:12211–12217, 2006.

[155] Moonsub Shim and Philippe Guyot-Sionnest. Permanent dipole moment and charges in colloidal semiconductor quantum dots. *The Journal of Chemical Physics*, 111(15):6955–6964, 1999.

[156] Yasuhiro Shirasaki, Geoffrey J. Supran, Moungi G. Bawendi, and Vladimir Bulović. Emergence of colloidal quantum-dot light-emitting technologies. *Nature Photonics*, 7(1):13–23, 2012.

[157] William Shockley and Hans J. Queisser. Detailed Balance Limit of Efficiency of p–n Junction Solar Cells. *Journal of Applied Physics*, 32(3):510–519, 1961.

[158] Jonathan H. Skone, Marco Govoni, and Giulia Galli. Self-consistent hybrid functional for condensed systems. *Phys. Rev. B.*, 89:195112, 2014.

[159] Tyler J Smart, Feng Wu, Marco Govoni, and Yuan Ping. Fundamental principles for calculating charged defect ionization energies in ultrathin two-dimensional materials. *Physical Review Materials*, 2(12):124002, 2018.

[160] Edward I. Solomon, Thomas C. Brunold, Mindy I. Davis, Jyllian N. Kemsley, Sang-Kyu Lee, Nicolai Lehnert, Frank Neese, Andrew J. Skulan, Yi-Shan Yang, and Jing Zhou. Geometric and electronic structure/function correlations in non-heme iron enzymes. *Chemical Reviews*, 100(1):235–350, 2000.

[161] M. Stankovski, G. Antonius, D. Waroquiers, A. Miglio, H. Dixit, K. Sankaran, M. Giantomassi, X. Gonze, M. Côte, and G.-M. Rignanese. G^0W^0 band gap of ZnO: Effects of plasmon-pole models. *Phys. Rev. B.: Condens. Matter Mater. Phys.*, 84:241201, 2011.

[162] Massimiliano Stengel and Nicola A. Spaldin. Accurate polarization within a unified Wannier function formalism. *Physical Review B*, 73(7):075121, 2006.

[163] FH Streitz, RC Cammarata, and Karl Sieradzki. Surface-stress effects on elastic properties. I. Thin metal films. *Physical Review B*, 49(15):10699, 1994.

[164] A. Szemjonov, T. Pauporté, S. Ithurria, N. Lequeux, B. Dubertret, I. Ciofini, and F. Labat. Ligand-stabilized cdse nanoplatelet hybrid structures with tailored geometric and electronic properties. new insights from theory. *RSC Adv.*, 4(99):55980–55989, 2014.

[165] Krisztina Szendrei, Mark Speirs, Widianta Gomulya, Dorota Jarzab, Marianna Manca, Oleksandr V. Mikhnenko, Maksym Yarema, Bart J. Kooi, Wolfgang Heiss, and Maria A. Loi. Exploring the Origin of the Temperature-Dependent Behavior of PbS Nanocrystal Thin Films and Solar Cells. *Advanced Functional Materials*, 22(8):1598–1605, 2012.

[166] Razika Zair Tala-Ighil. Nanomaterials in Solar Cells. In Mahmood Aliofkhazraei and Abdel Salam Hamdy Makhlouf, editors, *Handbook of Nanoelectrochemistry*. Springer International Publishing, Switzerland, 2015.

[167] Dmitri V. Talapin and Christopher B. Murray. PbSe Nanocrystal Solids for n- and p-Channel Thin Film Field-Effect Transistors. *Science*, 310(5745):86–89, 2005.

[168] Dmitri V Talapin, Elena V Shevchenko, Christopher B Murray, Alexey V Titov, and Petr Král. DipoleDipole Interactions in Nanoparticle Superlattices. *Nano Letters*, 7(5):1213–1219, 2007.

[169] Jiang Tang, Kyle W. Kemp, Sjoerd Hoogland, Kwang S. Jeong, Huan Liu, Larissa Levina, Melissa Furukawa, Xihua Wang, Ratan Debnath, Dongkyu Cha, Kang Wei Chou, Armin Fischer, Aram Amassian, John B. Asbury, and Edward H. Sargent. Colloidal-quantum-dot photovoltaics using atomic-ligand passivation. *Nature Materials*, 10(10):765–771, 2011.

[170] Tian Tian, Declan Scullion, Dale Hughes, Lu Hua Li, Chih-Jen Shih, Jonathan Coleman, Manish Chhowalla, and Elton J. G. Santos. Electronic polarizability as the fundamental variable in the dielectric properties of two-dimensional materials. *Nano Letters*, 20(2):841–851, 2020.

[171] Benjamin E. Treml, Benjamin H. Savitzky, Ali M. Tirmzi, Jessica Cimada DaSilva, Lena F. Kourkoutis, and Tobias Hanrath. Successive Ionic Layer Absorption and Reaction for Postassembly Control over Inorganic Interdot Bonds in Long-Range Ordered Nanocrystal Films. *ACS Applied Materials & Interfaces*, 9(15):13500–13507, 2017.

[172] J. J. Urban, D. V. Talapin, E. V. Shevchenko, and C. B. Murray. Self-assembly of PbTe quantum dots into nanocrystal superlattices and glassy films. *J. Am. Chem. Soc.*, 128:3248–3255, 2006.

[173] M. J. van Setten, M. Giantomassi, E. Bousquet, M. J. Verstraete, D. R. Hamann, X. Gonze, and G.-M. Rignanese. The PseudoDojo: Training and grading a 85 element optimized norm-conserving pseudopotential table. *Computer Physics Communications*, 226:39–54, 2018.

[174] David Vanderbilt. Soft self-consistent pseudopotentials in a generalized eigenvalue formalism. *Physical Review B.*, 41:7892–7895, 1990.

[175] David Vanderbilt and R.D. King-Smith. Electric polarization as a bulk quantity and its relation to surface charge. *Physical Review B*, 48:4442, 1993.

[176] Roman B. Vasiliev, Alexander I. Lebedev, Elizabeth P. Lazareva, Natalia N. Shlenskaya, Vladimir B. Zaytsev, Alexei G. Vitukhnovsky, Yuanzhao Yao, and Kazuaki Sakoda. High-energy exciton transitions in quasi-two-dimensional cadmium chalcogenide nanoplatelets. *Phys. Rev. B.*, 95:165414, 2017.

[177] Lok C Lew Yan Voon and Morten Willatzen. *The kp method: electronic properties of semiconductors*. Springer Science & Business Media, 2009.

[178] Márton Vörös, Giulia Galli, and Gergely T. Zimanyi. Colloidal Nanoparticles for Intermediate Band Solar Cells. *ACS Nano*, 9(7):6882–6890, 2015.

[179] Quan Wan. *First principles simulations of vibrational spectra of aqueous systems*. PhD thesis, Ann Arbor, 2015.

[180] M. C. Weidman, M. E. Beck, R. S. Hoffman, F. Prins, and W. A. Tisdale. Monodisperse, air-stable PbS nanocrystals via precursor stoichiometry control. *ACS Nano*, 8:6363–6371, 2014.

[181] Kevin Whitham and Tobias Hanrath. Formation of Epitaxially Connected Quantum Dot Solids: Nucleation and Coherent Phase Transition. *The Journal of Physical Chemistry Letters*, 8(12):2623–2628, 2017.

[182] Kevin Whitham, Jun Yang, Benjamin H. Savitzky, Lena F. Kourkoutis, Frank Wise, and Tobias Hanrath. Charge transport and localization in atomically coherent quantum dot solids. *Nature Materials*, 15(5):557–563, 2016.

[183] Feng Wu, Andrew Galatas, Ravishankar Sundararaman, Dario Rocca, and Yuan Ping. First-principles engineering of charged defects for two-dimensional quantum technologies. *Physical Review Materials*, 1:071001(R), 2017.

[184] Yong Yan, Ryan W Crisp, Jing Gu, Boris D Chernomordik, Gregory F Pach, Ashley R Marshall, John A Turner, and Matthew C Beard. Multiple exciton generation for photoelectrochemical hydrogen evolution reactions with quantum yields exceeding 100%. *Nature Energy*, 2(NREL/JA-5900-66234), 2017.

[185] Jun Yang and Frank W. Wise. Effects of Disorder on Electronic Properties of Nanocrystal Assemblies. *The Journal of Physical Chemistry C*, 119(6):3338–3347, 2015.

[186] Peter Y. Yu and Manuel Cardona. *Fundamentals of Semiconductors.* Springer, 4 edition, 1996.

[187] Xiao Yu and Seth M. Cohen. Photocatalytic Metal-Organic Frameworks for Selective 2,2,2-Trifluoroethylation of Styrenes. *Journal of the American Chemical Society*, 138(38):12320–12323, 2016.

[188] Szymon J. Zelewski, Katarzyna C. Nawrot, Andrzej Zak, Marta Gladysiewicz, Marcin Nyk, and Robert Kudrawiec. Exciton binding energy of two-dimensional highly luminescent colloidal nanostructures determined from combined optical and photoacoustic spectroscopies. *The Journal of Physical Chemistry Letters*, 10(12):3459–3464, 2019.

[189] Haitao Zhang, Bo Hu, Liangfeng Sun, Robert Hovden, Frank W. Wise, David A. Muller, and Richard D. Robinson. Surfactant Ligand Removal and Rational Fabrication of Inorganically Connected Quantum Dots. *Nano Letters*, 11(12):5356–5361, 2011.

[190] Jianbing Zhang, Jianbo Gao, Elisa M. Miller, Joseph M. Luther, and Matthew C. Beard. Diffusion-Controlled Synthesis of PbS and PbSe Quantum Dots with *in Situ* Halide Passivation for Quantum Dot Solar Cells. *ACS Nano*, 8(1):614–622, 2014.

[191] Jing Zhang, Jason Tolentino, E. Ryan Smith, Jianbing Zhang, Matthew C. Beard, Arthur J. Nozik, Matt Law, and Justin C. Johnson. Carrier Transport in PbS and PbSe QD Films Measured by Photoluminescence Quenching. *The Journal of Physical Chemistry C*, 118(29):16228–16235, 2014.

[192] Qiuju Zhang, Baihai Li, and Liang Chen. First-Principles Study of Microporous Magnets M-MOF-74 (M = Ni, Co, Fe, Mn): the Role of Metal Centers. *Inorganic Chemistry*, 52(16):9356–9362, Aug 2013.

[193] Haiguang Zhao, Hongyan Liang, François Vidal, Federico Rosei, Alberto Vomiero, Dongling Ma, Franc Ois Vidal, Federico Rosei, Alberto Vomiero, and Dongling Ma.

Size Dependence of Temperature-Related Optical Properties of PbS and PbS/CdS Core/Shell Quantum Dots. *The Journal of Physical Chemistry C*, 118(35):20585–20593, 2014.

[194] Jian Zhou and Qiang Sun. Magnetism of Phthalocyanine-Based Organometallic Single Porous Sheet. *J. Am. Chem. Soc.*, 133(38):15113–15119, Aug 2011.

[195] Qunfei Zhou, Yeongsu Cho, Shenyuan Yang, Emily A. Weiss, Timothy C. Berkelbach, and Pierre Darancet. Large band edge tunability in colloidal nanoplatelets. *Nano Letters*, 19(10):7124–7129, 2019.